

**Thermodynamic Modelling and Experimental
Investigation of 3D Printed Inconel 718 Superalloy**

Xinzhao Mu

A Thesis in

The Department

of

Mechanical, Industrial & Aerospace Engineering (MIAE)

Presented in Partial Fulfillment of the

Requirements for the Degree of Master of Applied Science

(Mechanical Engineering) at Concordia University

Montreal, Quebec, Canada

August, 2022

© Xinzhao Mu, 2022

CONCORDIA UNIVERSITY

School of Graduate Studies

This is to certify that the thesis prepared

By: Xinzhao Mu

Entitled: Thermodynamic Modelling and Experimental Investigation of 3D Printed Inconel
718 Superalloy

and submitted in partial fulfillment of the requirements for the degree of

Master of Applied Science (Mechanical Engineering)

Complies with the regulations of the University and meets the accepted standards with respect to originality and quality.

Signed by the final examining committee:

_____	Chair
Dr.	
_____	Examiner
Dr.	
_____	Examiner
Dr.	
_____	Supervisor
Dr. Mamoun Medraj	
_____	Co-Supervisor
Dr. Mezbahul Islam	

Approved by: _____
Dr. Martin Pugh Chair of Department or Graduate Program Director

Mourad Debbabi Dean of Faculty

Date:

Abstract

Thermodynamic Modelling and Experimental Investigation of 3D Printed Inconel 718

Superalloy

Xinzhao Mu

In recent years, with the constant maturity of metal 3D printing technology, the additive manufacturing of IN718, nickel-base superalloy, has attracted very strong attention in the aerospace field. Additive manufacturing, especially the laser powder bed fusion (LPBF) of IN718, has several advantages over the conventionally manufactured IN718 (cast and wrought) because additive manufacturing is more time-saving with lower cost and a lower buy-to-fly ratio. However, 3D printed IN718 components still exhibit defects due to thermal gradient during printing. This thermal gradient affects the mechanical properties of printed parts to a large extent. Performing some special post-processing heat treatment could minimize this problem. However, only heat treatments designed for conventionally manufactured IN718 are currently applied to the printed material. Therefore, establishing and optimizing a thermodynamic database representing the 3D printed IN718 alloy is essential to effectively guide the heat treatment and obtain information on phase formation and transformation.

In this work, firstly, a customized database was constructed by optimizing the phases presented in IN718, starting with the lower-order binary systems, followed by extrapolation to higher-order systems. The customized database is used to calculate the thermodynamic properties and predict phase formation in the IN718 alloy. Furthermore, to validate this database, experimental investigations, including differential scanning calorimetry (DSC) and scanning electron microscopy (SEM), are done to determine the temperature of different phase transitions and the microstructure of the printed IN718 alloy. The modelling results obtained in the current work are more consistent with the current experimental results and the experimental results from the literature than the results obtained using two commercial databases

Acknowledgments

The accomplishment of this dissertation would not be possible without the help of many people at Concordia University.

First of all, I would like to express my sincere gratitude and appreciation to my thesis supervisor Dr. Mamoun Medraj for his time, suggestions, support, and encouragement. Dr. Mamoun Medraj has inspired me a lot, especially with his discerning and innovative idea on research.

Then, I would like to thank my parents for giving me life, bringing me up, educating me, and encouraging me in my study all the time. Especially during the completion of my dissertation, the Covid-19 pandemic was raging, and I felt homesick and hard at times. My parents gave me a lot of encouragement and support. I really appreciate their endless and unconditional love.

My sincere thanks go to all the TMG group members, especially Dr. Mezbahul, who inspired and helped me a lot with thermodynamic modelling. Also, thanks to J.C. Franco-Correa for helping me with Thermo-Calc calculation and some experiments. And thanks to J.C. Franco-Correa for his help and useful suggestions during my thesis writing. I would also like to give many thanks to Mazen Samara and Dmytro Kevekov for their help and support throughout my experimental work. I cannot imagine how I would have done this amount of work without all this help.

Thanks to all my friends for their support and encouragement during my MAsC project.

Lastly, I would thank the almighty God for giving me a lot of courage and strength to overcome the difficulties and complete this dissertation.

Table of Contents

LIST OF FIGURES.....	vii
LIST OF TABLES.....	xi
CHAPTER 1 INTRODUCTION.....	1
1.1 INCONEL 718 (IN718) SUPERALLOY.....	1
1.2 MANUFACTURING METHOD OF IN718	2
1.3 LASER-BASED POWDER BED FUSION (LPBF) PRINTED IN718	4
1.4 THERMODYNAMIC MODELLING	5
1.5 AIM OF THIS WORK.....	6
CHAPTER 2 LITERATURE REVIEW.....	8
2.1 PHASES IN IN718	8
2.2 GAMMA PHASE	9
2.3 GAMMA PRIME PHASE.....	9
2.3 GAMMA DOUBLE PRIME PHASE	15
2.4 DELTA PHASE	17
2.5 LAVES PHASE.....	19
2.6 CARBIDES	25
CHAPTER 3 THERMODYNAMIC MODELLING.....	26
3.1 BASIC THERMODYNAMIC PRINCIPLE.....	27
3.2 GENERAL THERMODYNAMIC MODEL.....	28
3.3 SOLUTION MODEL	29
3.3.1 Regular Solution Model	29
3.3.2 Associated Solution Model.....	30
3.3.3 Sublattice Model.....	30
3.3.4 Interaction Parameters	32

3.4 EXTRAPOLATION AND ASSESSMENT OF HIGHER-ORDER SYSTEMS.....	33
CHAPTER 4 CALCULATION RESULTS OF THE BINARY SYSTEMS IN THE IN718 ALLOY	35
4.1 Γ' PHASE.....	35
4.2 Γ'' PHASE	41
4.3 LAVES PHASE	48
4.4 DELTA PHASE.....	61
CHAPTER 5 THERMODYNAMIC CALCULATION RESULTS OF THE IN718 ALLOY	65
5.1 EQUILIBRIUM CALCULATION.....	65
5.2 NON-EQUILIBRIUM CALCULATION	69
5.3 EXPERIMENTAL VERIFICATION	72
5.3.1 Sample Preparation.....	72
5.3.2 Phase Transformation Analysis	76
5.3.3 Microstructural and Phase Analysis	82
CHAPTER 6 CONCLUSIONS, CONTRIBUTIONS AND RECOMMENDATIONS FOR FUTURE WORK.....	90
6.1 CONCLUSION	90
6.2 CONTRIBUTIONS	91
6.3 RECOMMENDATIONS FOR FUTURE WORK.....	92

List of Figures

Figure 1-1 Number of publications per year on AM of Inconel 718	4
Figure 1-2. Schematic drawing of the laser powder bed fusion process [14].....	5
Figure 2-1 Crystal structure of γ' phase [20]	10
Figure 2-2 The Al-Ni phase diagram calculated from the Huang and Chang [24].....	11
Figure 2-3 The Al-Ti phase diagram calculated from Kattner <i>et al.</i> [28].....	12
Figure 2-4 The Ni-Ti phase diagram calculated from Bellen <i>et al.</i> [33]	13
Figure 2-5 Crystal structure of γ'' phase [7].....	14
Figure 2-6 The Al-Nb phase diagram calculated from Witusiewicz [38]	15
Figure 2-7 Unit cell of the Delta phase [42]	17
Figure 2-8 The Ni-Nb phase diagram calculated from Chen and Du [43]	18
Figure 2-9 high-magnification SEM picture of the as-deposited IN718 sample [51]	19
Figure 2-10 The calculated Cr-Ti phase diagram [56].....	20
Figure 2-11 The calculated Cr-Nb phase diagram with superimposed experimental result points [62]	21
Figure 2-12 The calculated Fe-Ti phase diagram [67].....	23
Figure 2-13 The calculated Fe-Nb phase diagram with an overlay of the previous thermodynamic assessment [73]	23
Figure 3-1. Flow chart of the thermodynamic optimization using the CALPHAD method [77]	26

Figure 3-2 Graphical explanation about four different ternary extrapolation methods [84] .. 34

Figure 4-1 The calculated Al-Ni phase diagram using the optimized parameter of γ' combined with the FTlite database. Phase boundaries of γ' are compared with the relevant data from the literature. 40

Figure 4-2 The calculated Al-Nb phase diagram using the optimized parameter of γ' combined with the FTlite database. Phase boundaries of γ'' are compared with the relevant data from the literature. 46

Figure 4-3 Enlarged area in the vicinity of γ'' shown in Figure 4-2..... 46

Figure 4-4 The calculated Al-Ti phase diagram using the optimized parameter of γ'' combined with the FTlite database. Phase boundaries of γ'' are compared with the relevant data from the literature. 47

Figure 4-5 Enlarged area in the vicinity of γ'' shown in Figure 4-4..... 47

Figure 4-6 The calculated Cr-Ti phase diagram using the optimized parameter of C14 Laves combined with the FTlite database. Phase boundaries of C14 Laves are compared with the relevant data from the literature. 55

Figure 4-7 The calculated Cr-Nb phase diagram using the optimized parameter of C14 Laves combined with the FTlite database. Phase boundaries of C14 Laves are compared with the relevant data from the literature. 57

Figure 4-8 The calculated Fe-Nb phase diagram using the optimized parameter of C14 Laves combined with the FTlite database. Phase boundaries of C14 Laves are compared with the relevant data from the literature. 58

Figure 4-9 The calculated Fe-Ti phase diagram using the optimized parameter of C14 Laves combined with the FTlite database. Phase boundaries of C14 Laves are compared with the relevant data from the literature.	63
Figure 4-10 The calculated Ni-Nb phase diagram using the optimized parameter of δ phase combined with the FTlite database. Phase boundaries of δ are compared with the relevant data from the literature.	64
Figure 5-1 Equilibrium calculation of the mass percentage of phases as a function of temperature for the IN718 alloy using the FactSage database [76]	66
Figure 5-2 Equilibrium calculation of the mass fraction of phases as a function of temperature for the IN718 alloy using Thermo-Calc database [104]	67
Figure 5-3 Equilibrium calculation of the mass percentage of phases as a function of temperature for the IN718 alloy using the current customized database combined with the FTlite database	68
Figure 5-4 Enlarged area of Figure 5-3	68
Figure 5-5 Non-equilibrium calculation of the mass percentage as a function of temperature for IN718 by FTlite database [76] without the current database	70
Figure 5-6 Non-equilibrium calculation of the mass fraction of phases as a function of temperature for IN718 alloy using Thermo-Calc database [104]	70
Figure 5-7 Non-equilibrium calculation of the mass percentage of phases as a function of temperature for IN718 alloy using the current customized database combined with FTlite ..	71
Figure 5-8 partially enlarged area of Figure 5-7	72

Figure 5-9 (a) Scanning electron microscopy (SEM) micrograph of original Inconel 718 powder (b) single particle of original Inconel 718 powder.....	73
Figure 5-10 (a) Dimensions of the printed IN718 sample (b) appearance of the printed IN718 sample	75
Figure 5-11 DSC spectra and reaction temperatures of the IN718 powder	76
Figure 5-11 DSC cooling curve and phase transformation temperatures of IN718	77
Figure 5-12 DSC cooling curve and phase transformation temperatures of IN718	80
Figure 5-13 DSC heating curve and reaction temperatures of IN718	81
Figure 5-14 High magnification SEM images showing the γ , γ' , γ'' and δ phases.....	83
Figure 5-15 (a) Original high magnification SEM image; (b) image after the filter process; (c) image after setting the contrast thresholds; (d) final image for filtering out the phases.....	84
Figure 5-17 (a-d) Original high magnification SEM micrographs; (b-h) images after setting the contrast thresholds; (i-l) final image after filtering out the phases.	85

List of Tables

Table 1-1 The alloying elements, mass fraction, and their effect in IN718 [5,6,7]	2
Table 2-1 Crystal structure and chemical formula of phases in the IN718 superalloy [19]	9
Table 4-1. Crystallographic information of gamma prime phase	36
Table 4-2 Comparison of this work and different experimental results of invariant equilibria in the Al-Ni system	37
Table 4-3 Optimized Thermodynamic parameters for gamma prime phase in the IN718 alloy	39
Table 4-4 Crystallographic information of γ'' phase	42
Table 4-5 Comparison of this work and different experimental results of invariant equilibria in the Al-Nb system	43
Table 4-6 Comparison of this work and different experimental results of invariant equilibria in the Al-Ti system	44
Table 4-7 Optimized Thermodynamic parameters for γ'' in IN718 alloy	45
Table 4-8 Crystallographic information of the Laves phase	49
Table 4-9 Optimized Thermodynamic parameters for the Laves phase in IN718 alloy	50
Table 4-10 Comparison between this work and different experimental results from the literature of the C14-Laves invariant equilibria in the Cr-Ti system	53
Table 4-11 Comparison between this work and different experimental results from the literature of the C14-Laves invariant equilibria in the Cr-Nb system	55

Table 4-12 Comparison between this work and different experimental results from the literature of the C14-Laves invariant equilibria in the Fe-Nb system.....	57
Table 4-13 Comparison between this work and different experimental results from the literature of the C14-Laves invariant equilibria in the Fe-Ti system	59
Table 4-14 Crystallographic information of Delta phase.	62
Table 4-15 Optimized thermodynamic parameters for the δ phase in the IN718 alloy.....	62
Table 4-16 Comparison between this work and different experimental results from the literature of the δ phase invariant equilibria in the Ni-Nb system	63
Table 5-1 EDS chemical composition of the IN718 powder.....	72
Table 5-2 Precipitation temperature for main phases in the 3D printed IN718 alloy under equilibrium condition	78
Table 5-3 Precipitation temperature for main phases in the 3D printed IN718 alloy under non-equilibrium condition	82
Table 5-4 EDS spot analysis results (The spectrum number correspond to the spot number in Figure 5-16)	85
Table 5-5 Phase content in the 3D-printed IN718 alloy....	87

Chapter 1 Introduction

This chapter briefly introduces some details of the Inconel 718 superalloy. Different manufacturing methods of the Inconel 718 alloy are discussed briefly. Especially the improvement of additive manufacturing technology in recent years makes it possible to further improve the properties of this alloy. The thermodynamic modelling of IN718 is also introduced. Finally, the objectives of this research work are presented.

1.1 Inconel 718 (IN718) Superalloy

Inconel 718 (IN718) is one of the most widely used nickel-based high-temperature alloys. In the year 1959, Inconel 718 (IN718) was developed by the International Nickel Company [1]. In the following years, IN718 was massively used in commercial engines, especially gas turbines. Nickel-based superalloys generally contain six main phases (gamma, gamma prime, gamma double prime, delta, Laves and carbides) [2]. It is worth noting that the primary strengthening mechanism of IN718 is precipitation strengthening. The main strengthening phase is γ' complemented by metastable γ'' phase) with body-centered tetragonal (BCT) D0₂₂ structure [3]. The metastable γ'' transfers to the equilibrium δ phase (Ni₃Nb) with an orthorhombic structure under certain conditions [4]. Compared to other types of precipitation hardening alloys, the precipitation of the γ'' phase in the γ matrix makes the IN718 alloy more stable [5] in the temperature range within which the alloy is normally used. Hence, IN718 is widely used in the fabrication of high-temperature resistant parts and engines for aero and space rockets because of its high strength and resistance to oxidation, corrosion, and fatigue even at elevated temperatures. The main elements and their weight percentages are listed in Table 1-1, and the different effects are also included.

Table 1-1 The alloying elements, mass fraction, and their effect in IN718 [5,6,7]

Element	Weight %	Effect
Ni	50-55	Solid solution base
Cr	17-21	Solid solution strengthener, improve hot corrosion and oxidation resistance, $M_{23}C_6$ carbides former
Nb	4.75-5.5	Strengthening phase former γ'' (Ni_3Nb), M_6C and MC carbides former
Ti	0.65-1.15	Strengthening phase former γ' ($Ni_3(Al,Ti)$), MC carbides former
Al	0.2-0.8	Strengthening phase former γ' ($Ni_3(Al,Ti)$), improves hot corrosion and oxidation resistance
Mo	2.8-3.3	Solid solution strengthener, $M_{23}C_6$ and MC carbides former, improves the tribological properties and wet corrosion resistance
Co	< 1.0	Solid solution strengthener, increases the solvus temperature of γ' phase
C	< 0.08	Grain boundary strengthener
Fe	Balance	Solid solution strengthener

1.2 Manufacturing Method of IN718

In general, conventional manufacturing methods of IN718 include casting and bulk deformation such as forging. In particular, following the emergence and development of vacuum melting, the processing and composition control of superalloys became relatively easier. Most of the IN718 parts used in high-temperature applications are in the form of cast or forged products [7]. However, IN718 casting can produce defects in microstructure, such as coarse grains, and is prone to macro-segregation, which is harmful to mechanical properties. On the other hand, wrought IN718 parts tend to be more homogenous because cast structure is dissolved and dispersed, as the parts undergo repeated heating and deformation during processing [6]. However, when complex structural parts (such as turbine blades) need to be

machined, it is difficult to complete the process only by traditional casting and forging methods. Therefore, this wastes a lot of high-value forged raw materials due to machining. This has led to an interest in additive manufacturing of IN718.

Additive manufacturing (AM) is a group of manufacturing processes that use the layer-by-layer concept to fabricate near-net-shape 3D components from a digital 3D model [7]. Additive manufacturing has many advantages, such as reduced manufacturing time, low production cost, and a low buy-to-flight ratio [8,9]. Therefore, AM has gained a lot of attention in various industries such as aerospace, automotive, and medical. According to the ASTM F42 standard, additive manufacturing is roughly divided into seven categories [10]. Each category is different because of the material used, the heating source, the deposition technique, or the way the material melts or solidifies. Among them, powder bed fusion (PBF), Direct energy deposition (DED), binder jetting (BJ), and sheet lamination (SL) are the manufacturing processes used for metals. In the PBF process, the metallic powder is selectively melted and fused using either a high-intensity laser beam or electron beam to form three-dimensional (3D) objects. The laser-based powder bed fusion (LPBF) process generally includes selective laser melting (SLM) and selective laser sintering (SLS) techniques [11,12]. Compared with other processes, LPBF has a higher cooling rate ($105^{\circ}\text{C}/\text{s}$) and better surface finishing [13]. Therefore, finer structure and higher mechanical properties can be obtained. Figure 1-1 shows the increasing research interest in recent years in additive manufacturing of IN718 (The statistics are extracted from Scopus and Google Scholar).

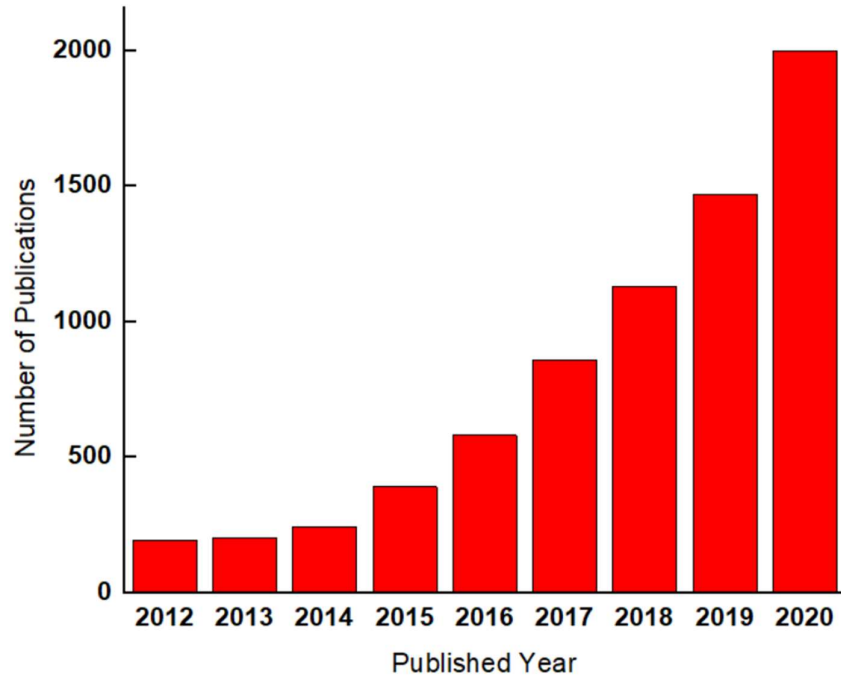


Figure 1-1. Number of publications per year on AM of Inconel 718

1.3 Laser-based Powder Bed Fusion (LPBF) Printed IN718

A schematic of the LPBF operation is shown in Figure 1-2 [14]. Before the printing process, the CAD modelling of the part is required. The CAD model is sliced into uniform cross-sections which will be set equal to the layer thickness used in the LPBF process. During the printing process, the powder on the building platform is preheated to mitigate thermal gradients and minimize thermal stress. In addition, the building chamber is evacuated and filled with argon gas during the printing process to reduce oxidation. Meanwhile, rotating powder levelling rollers on both sides control the required metal powder for each layer of the printing process. After a single layer is printed, the building platform is moved down one layer in thickness. Then, one of the side rollers will rotate to provide the required powder for a new layer. This process is repeated until the final 3D part is built [14].

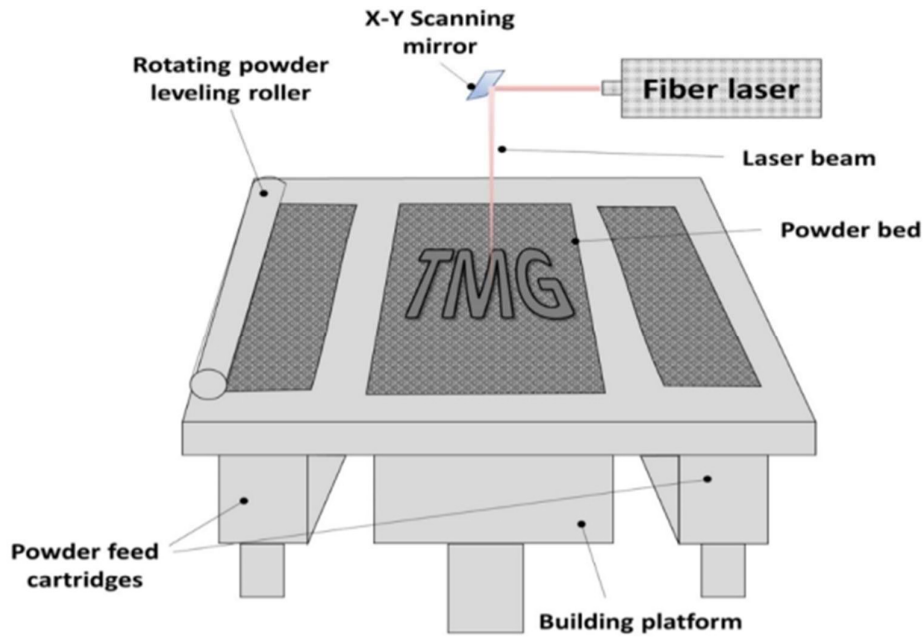


Figure 1-2. Schematic drawing of the laser powder bed fusion process [14]

1.4 Thermodynamic Modelling

When referring to thermodynamic description, the CALPHAD (CALculation of PHase Diagrams) technique [15] has to be mentioned. CALPHAD combines data from thermodynamics, phase diagrams, and physical properties such as magnetism into a unified and consistent model, represented as Gibbs energy which could be further used to calculate the thermodynamic properties and phase transformation of multi-component materials. For example, the solidification process of the entire system can be simulated computationally to obtain thermodynamic information such as phase fractions, elemental segregation, and even information about metastable phases [16].

The most commonly used thermodynamics software are FactSage, Thermo-Calc, and Pandat. Each one has its advantages and disadvantages in terms of thermodynamic calculation and modelling, but they all contain an embedded calculation module for calculating different types of phase diagrams and thermodynamic properties of different phases. Although different

software packages use different thermodynamic databases, there is little influence on the calculation results of binary and, to a lesser extent, on the ternary phase diagrams. But when it comes to higher-order systems, such as quaternary or higher-order alloy systems with more elements (such as nickel-based alloys), existing databases are generally unverified due to a lack of experimental data. This means that the simulation results are not as accurate. It is also possible to have some missing phases. Fortunately, thermodynamic software allows users to build a user database. Most software packages also include an assessment module to optimize the thermodynamic functions of phases based on experimental data. This capability provides support for developing more accurate models for high-order systems that help understand complex alloys. In the present work, the customization of the database has been done using all the available resources from the literature along with the experimental finding from our research group. This will be explained elaborately in chapters 3 and 4.

1.5 Aim of this Work

With the development of additive manufacturing for metals, significant interest has been directed to printed nickel-based superalloys. Therefore, it becomes essential to establish accurate thermodynamic models for these superalloys. The current work provides a better understanding of the formation and transformation of the main phases (γ , γ' , γ'' , δ and Laves phase) in the 3D printed IN718 alloy. A database describing the main phases in Inconel 718 has been established in this work to generate a more accurate thermodynamic description of the main phases in this alloy. The specific goals of this thesis include:

- Identifying and evaluating the main phases present in the IN718 alloy as well as reassessing the binary systems of the alloying elements (Ni, Nb, Fe, Al, Ti, C, Cr) in which these phases are presented.

- Optimizing the thermodynamic models to describe the Gibbs free energy of IN718 phases in the binary systems.
- Establishing a customized database including these phases in the higher-order IN718 alloy through extrapolation and merging assessment.
- Obtaining phase formation and transformation information of the IN718 alloy by performing equilibrium and non-equilibrium calculations using the customized database.
- Verifying and adjusting the customized database and thermodynamic calculations through key experiments, including DSC and SEM tests.

It is worth mentioning here that this work aims at building the thermodynamic database for printed IN718 because currently, there is no optimized database for calculating printed IN718 alloy with correct phase formation and transformation information. This is a first step necessary to obtain the Time-Temperature-Transformation (TTT) diagram in order to understand the kinetics of the printed IN718 alloy and to design a better heat treatment process for IN718 printed components. The printed IN718 shows different mechanical properties and phase assemblage compared with the cast and wrought IN718 alloys. Therefore, the heat treatments used for the cast and wrought materials are not suitable for the printed one. Nevertheless, so far, most of the research has been using the cast and wrought standard heat treatments to improve the microstructure and mechanical properties of the printed IN718. However, the research [6,8,14] is showing that these treatments do not work and different ones need to be designed specifically for the printed material. The research included in this thesis is a first step in building computation tools to simulate and understand the processing and structure of 3D printed IN718.

Chapter 2 Literature Review

This chapter reviews some previous studies on the main phases in Inconel 718, including the main elemental composition of each phase and the different attributes of these phases. In addition, the original forms of these phases in binary systems are described. The findings based on this literature review highlight the need for further research to address the lack of an accurate thermodynamic description of this alloy. Due to the lack of some relevant thermodynamic assessments in the higher-order subsystems, such as the ternary subsystems, which included gamma prime phase, Laves, etc., it becomes difficult to extrapolate to the complex multi-components IN718 alloy by traditional assessment. Therefore, the current research starts from the binary subsystems and directly extrapolates to higher-order systems containing all the elements that are present in the phase, to build the Gibbs free energy of the corresponding phase. The explanation of this process and evaluation of the higher-order systems is described in chapter 3.

2.1 Phases in IN718

IN718 is a multiphase alloy with γ matrix as the primary phase and a variety of secondary phases such as γ' and γ'' strengthening phases, δ , Laves and carbides [17, 18]. Different phase has different chemical formula and crystal structure, which provides different property for the superalloy. The chemical composition and crystal structure of these phases are shown in Table 2-1. The details of the different phases will be discussed later in this chapter.

Table 2-1 Crystal structure and chemical formula of the different phases in the IN718 superalloy [19]

Phase	Chemical formula	Crystal structure	Space group
γ	Ni, Cr, Fe, etc.	FCC	Fm-3m
γ'	$\text{Ni}_3(\text{Al, Ti})$	FCC (ordered L12)	Pm-3m
γ''	Ni_3Nb	BCT (ordered D022)	I4/ mmm
δ	Ni_3Nb	Orthorhombic	Pmmn
Laves	$(\text{Ni, Fe, Cr})_2(\text{Nb, Mo, Ti})$	Hexagonal	P63/ mmc
MC Carbides	$(\text{Nb, Ti})\text{C}$	Cubic	Fm-3m

2.2 Gamma Phase

The matrix of IN718 is the γ phase, which is a solid solution with a face-centered cubic lattice structure. The γ phase mainly contains Ni and Fe along with trace elements (Cr, Fe, Nb, Ti, etc.). The trace elements dissolved in the lattice cause distortion, resulting in solid solution strengthening [20]. In addition, alloying elements form a variety of secondary phases, which affect the microstructure and mechanical properties of the alloy.

2.3 Gamma Prime Phase

γ' phase is an intermetallic phase with an ordered face-centered cubic ($L1_2$) structure, which is one of the strengthening phases in the IN718 alloy. Its main chemical formula is $\text{Ni}_3(\text{Al, Ti})$. As shown in Figure 2-1, Al and Ti atoms are located in the corner of the unit cell, while Ni atoms are in the center of each face.

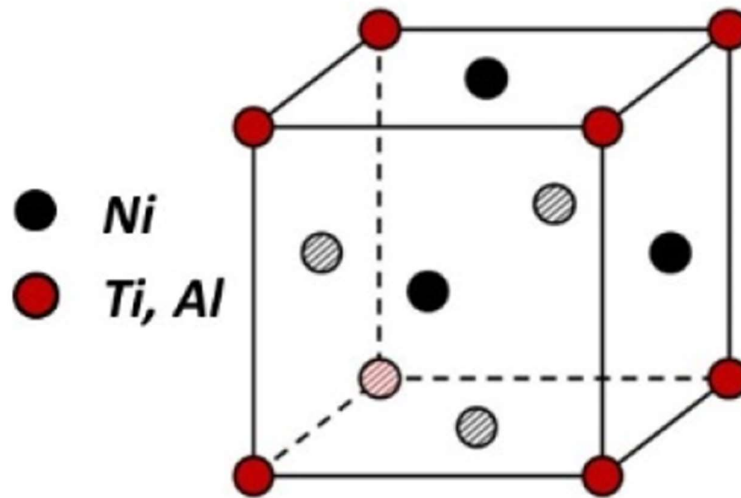


Figure 2-1 Crystal structure of the γ' phase [20]

Generally, the structural stability of the γ' phase is relatively high, and the more γ' in the system, the higher the mechanical properties it has. However, because the wt. % of Al and Ti in the IN718 alloy are relatively small as mentioned earlier, the amount of the γ' phase is less than that of the γ'' phase, which makes it a secondary strengthening phase. The precipitation temperature of the γ' phase is about 650 °C, while the solidus temperature is about 850-870 °C [20].

The relevant binary systems associated with the elements detected in the γ' phase in the IN718 alloy are: Al-Ni, Al-Ti, and Ni-Ti systems. Among them, only the Al-Ni binary system exhibits a stable γ' phase (Ni_3Al ($L1_2$)). The relevant compound with the same atomic ratio in the other two binaries shows a different crystal structure. For example, Ni_3Ti has HCP ($D0_{24}$) structure; Pearson = hP16; Space group = $P63/mmc$. Ni_3Al in the Al-Ni system has a tetragonal FCC ($D0_{22}$) structure, which is the same as the γ'' phase. For a binary system that does not show a stable γ' , adding a positive value to its Gibbs free energy in the sublattice model is necessary to ensure that it does not occur in that binary system. The details of this part will be explained

in the next chapter. Nevertheless, it is still necessary to review the literature for the Al-Ti and Ni-Ti binary systems in which the γ' phase does not stably exist. This is because in order to model this phase, Ni, Al, and Ti need to be included in the sublattice model of the γ' phase to represent it in the higher-order system. As mentioned above, although the solid solution of Ni_3Ti , Ni_3Al and Ni_3Al have the same atomic ratio, it exhibits different crystal structures and thermodynamic behaviour. Therefore, it is necessary to be extremely careful when modelling and optimizing hypothetical end-members related to these elements, which is also the reason for the literature review of all the binary phase diagrams of the constituent elements.

Kaufman and Nesor [21] were the first to model the Al-Ni phase diagram, while they treated the γ' phase as stoichiometric for simplification. Later they also reported the Al-Ni phase diagram using two Gibbs energy equations to model the γ' phase with less accuracy based on the experimental results from Hilpert *et al.* [22]. Ansara *et al.* [23] first used the sublattice model to describe this phase. The sublattice model became more acceptable and widely used to describe phases with solubility in this system. Subsequent studies continue while improving the model description following the guidelines reported by Ansara *et al.* [23]. For example, Huang and Chang [24] used the sublattice model with the same lattice ratio but different parameters to produce the Al-Ni phase diagram which is shown in Figure 2-2 [24], where the γ' phase is highlighted with a red dotted frame.

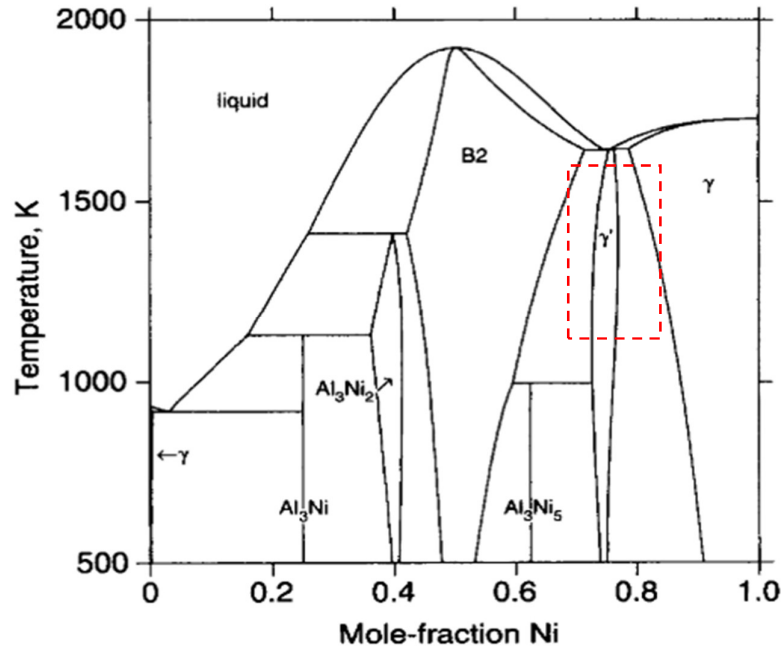


Figure 2-2 The Al-Ni phase diagram calculated by Huang and Chang [24]

As mentioned before, although the Al_3Ti and Ni_3Ti in the Al-Ti and Ni-Ti system show a different crystal structure compared with the γ' (L_{12}) phase in IN718 alloy, it is still necessary to carefully review this solid solution and pertaining binary system when modelling and optimizing hypothetical end-members.

For the Al-Ti system, Kaufman and Nesor [21] were the first to calculate this system. They assumed all the intermetallic compounds to be stoichiometric. Then, Murray [25] applied the unified sublattice model to describe Ti_3Al ($D0_{19}$) and $\alpha\text{-Ti}$ (A_3) in this system. But Al_3Ti ($D0_{22}$) was still treated as a line compound. After that, more experimental results became available. Saunders [26] worked on this system based on their experimental data and the experimental results from Svendsen *et al.* [27], while the homogeneity range of Al_3Ti ($D0_{22}$) was still ignored in the phase diagram because of its small solubility. Kattner *et al.* [28] performed a more accurate thermodynamic assessment combined with the experimental result from Zdziobek *et al.* [29], and then they proposed a Gibbs energy description of the ordered

phases, in which the narrow phase region of Al_3Ti (D0_{22}) was also reproduced. The results of these calculations were consistent with the experimental data, and the diagram reported by Kattner *et al.* [28] is shown in Figure 2-3.

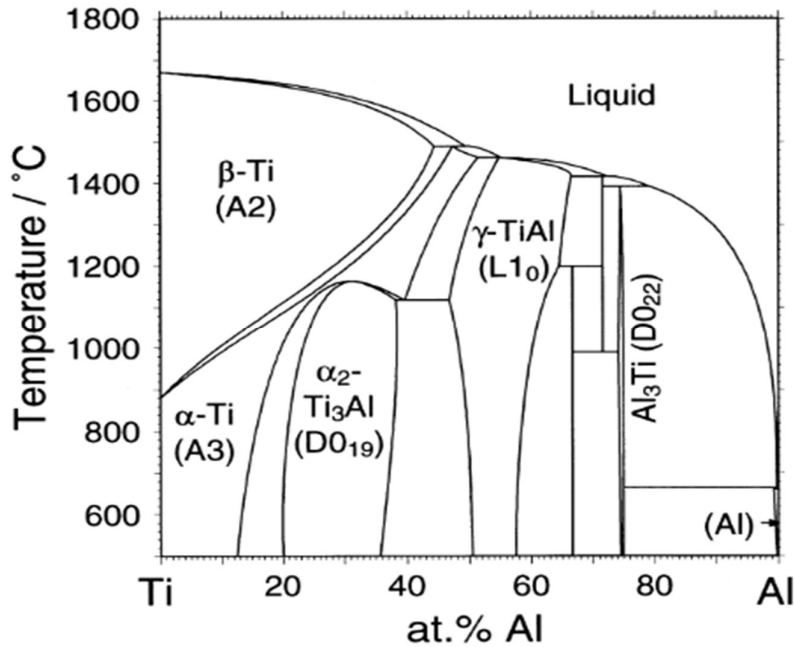


Figure 2-3 The Al-Ti phase diagram calculated by Kattner *et al.* [28]

For the Ni-Ti system, it was evaluated by Kaufman [30], Murraray [31], and Dupin [32]. These assessments simplified the NiTi and Ni₃Ti intermediate compounds as line compounds. Later, Saunders [26] used the sublattice model to take into account the homogeneity ranges, but some invariant reactions were not accurately reproduced compared with the experimental data. Then, Bellen *et al.* [33] used a different sublattice model for the Ni₃Ti compound, combining it with the disordered counterpart, the β -Ti (A_2) phase, which improved the description of the system. The Ni-Ti phase diagram reported by Bellen *et al.* [33] is shown in Figure 2-4.

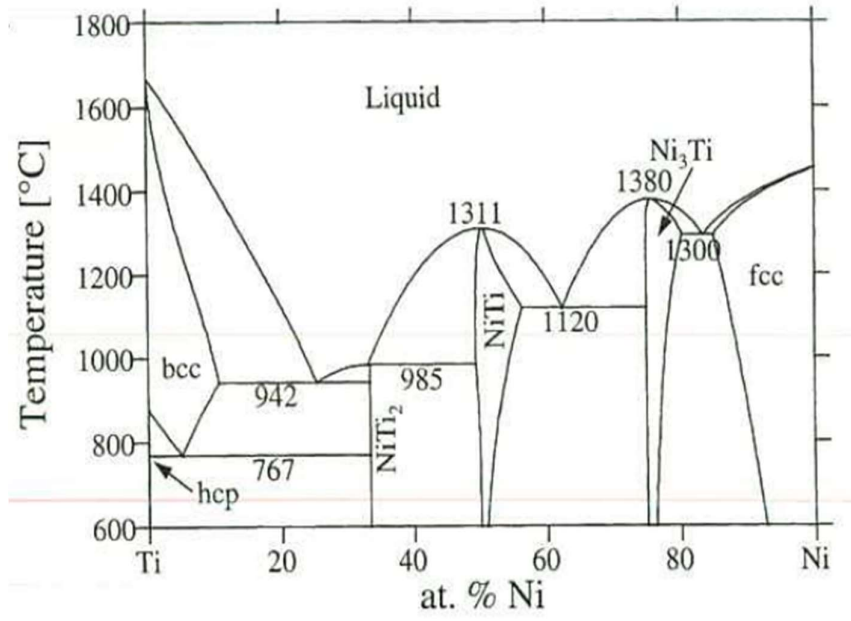


Figure 2-4 The Ni-Ti phase diagram calculated by Bellen *et al.* [33]

2.3 Gamma Double Prime Phase

The γ'' phase is the primary strengthening phase in IN718 alloy, which has an ordered body-centered tetragonal BCT ($D0_{22}$) structure as shown in Figure 2-5 [7]. Its main composition is Ni_3Nb , while some other research showed that it might include Ti [34]. Generally, Nb atoms are located at the corners of the tetragonal cell, while Ni is situated at the center of each face of the unit cell. Sometimes, Ti replaces Nb in the lattice or takes up some space in the cell. It is a metastable phase that normally precipitates during aging and has a tendency to coarsen and transform into the δ phase at high temperature [35]. Thus, this limits the operating temperature of IN718 alloys below 650°C . In addition, it has been proved that the driving force for transferring to the δ phase is reduced by adding Al and Ti in IN718 [7]. The morphology of the γ'' phase is disc-shaped that grows coherently within the γ -matrix.

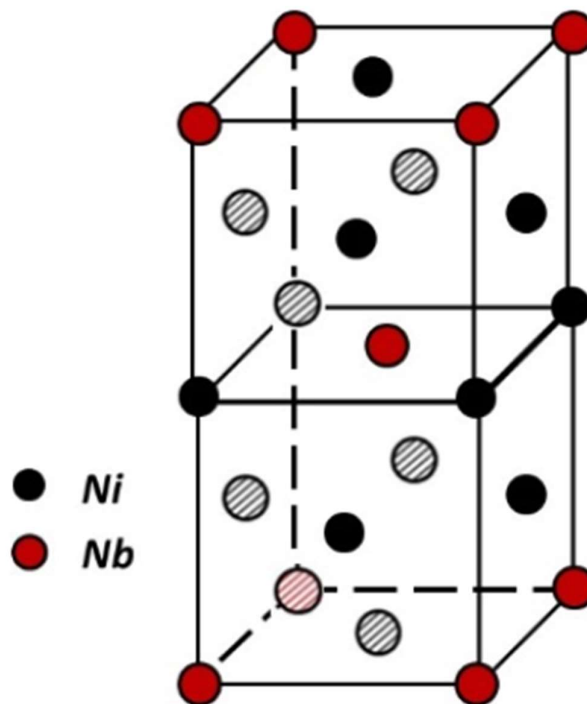


Figure 2-5 Crystal structure of the γ'' phase [7]

The main binary subsystems related to the gamma double prime phase with D0₂₂ structure are Al-Nb and Al-Ti systems with relatively small homogeneity ranges. Meanwhile, the ternary Al-Nb-Co and Al-Nb-Ti are pertinent systems as they both contain γ'' with D0₂₂ structure type. However, due to the incomplete experimental data, thermodynamic models of these ternary systems need more verification and reassessment.

For the Al-Nb phase diagram, Baron and Savitskii [36] studied it via thermal analysis (TA), building the foundation of the experimental Al-Nb phase diagram. After that, Jorda *et al.* [37] refined the Nb side region via differential thermal analysis (DTA), levitation thermal analysis (LTA), and electron probe microprobe analysis (EPMA). Their experimental data are considered to be more accurate and reliable since several experimental methods were performed. Al₃Nb was simplified as a line compound in the earlier calculated phase diagram as well as in the ternary phase diagram containing Al-Nb. Witusiewicz *et al.* [38] reassessed it by describing three intermediate phases with homogeneity ranges, especially, Al₃Nb (D0₂₂ with TiAl₃ tetragonal prototype)

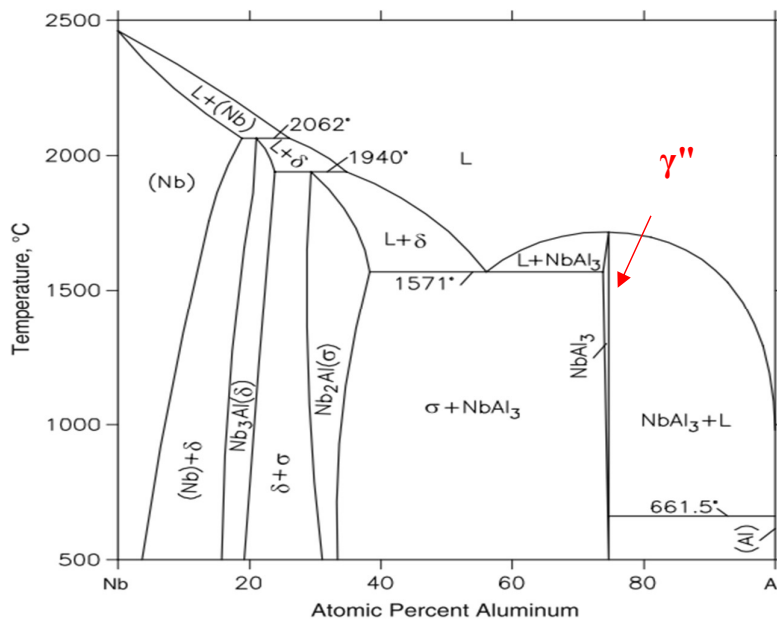


Figure 2-6 The Al-Nb phase diagram calculated by Witusiewicz *et al.* [38]

The Al-Ti system has four intermediate phases, in which Al_3Ti is the phase with the D0_{22} structure type. It is important to note that in some other assessments of this system, the Al_3Ti phase is separated into HT and LT parts because the crystal structure changes with temperature [39]. In addition, different authors used different denotations to represent this phase. For example, Witusiewicz denoted it as ϵ [38], while Cupid *et al.* [40] used the η phase. The range of homogeneity of TiAl_3 is relatively small in the binary system. Therefore, a sublattice model of Al_3Ti following the lattice ratio of 3:1 would be acceptable. However, when modelling it in a higher-order system, for example, adding Nb or B into the system, the homogeneity range of this phase will be increased. In this case, based on the experimental data, added elements shall be included in the first lattice to form a new sublattice model [40].

2.4 Delta Phase

The δ is a stable phase with an orthogonal D0_a structure [41]. It has the same chemical composition as the γ'' phase; Ni_3Nb , but the crystal structure is different. Its unit cell is shown in Figure 2-7 [42]. Generally, there are two different types of morphologies of the δ phase, needle-like and spherical. The morphology stability of the δ phase is dependent on temperature [43]. There is some debate about the nucleation temperature of this phase, and some authors mentioned it to be between 700 to 1000 °C [44], while others mentioned it to be from 750 to 1020 °C [45]. The solvus temperature of the δ phase is also uncertain due to the fluctuations in the chemical composition of the studied alloys, with the Nb content having the most influence on the solvus temperature [46]. The δ phase is more stable than γ'' , although its formation is slower. Therefore, if the alloy is exposed to high temperature for a long time, the δ phase forms as a transformation product of the γ'' phase [47].

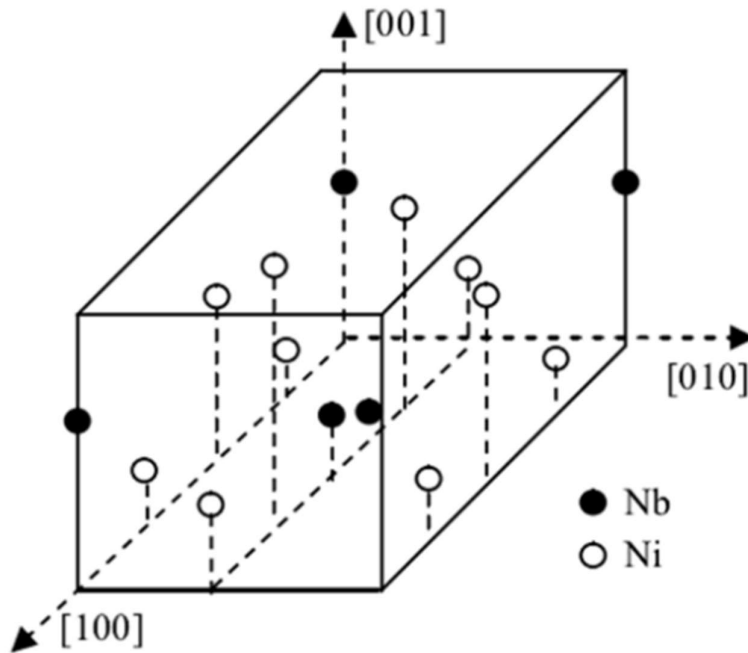


Figure 2-7 Unit cell of the δ phase [42]

The Ni-Nb binary system is the most important binary system related to the IN718 alloy since it contains elements included in γ'' and δ phases. Most noticeably, in this binary system, Ni_3Nb shows stability with the $D0_a$ crystal type, rather than the $D0_{22}$ of the metastable γ'' phase [48]. This phase also precipitates in some higher-order systems under certain conditions. For example, the Co-Al-Nb ternary system includes the γ'' ($D0_{22}$) phase, as shown in the work of He *et al.* [49]. There are three significant assessments of the Ni-Nb system that were carried out successively. Bolcavage and Kattner [41] revised the calculation of Ni-Nb. They included realistic enthalpy of formation values for the intermetallic phases. Besides, the Wagner-Schottky defect model was applied to describe and accommodate crystallographic assessment for the μ phase. Then Joubert *et al.* [42] reassessed this system taking into account new experimental data. Three independent sublattices were used to model the μ phase. The new experimental data are discussed in their paper [42], along with the formation energy of the Ni_3Nb compound calculated from the first-principles calculation, which is very close to the results obtained from

their reaction calorimetry experiment. After that, Chen and Du [43] published new experimental data that included the phase relation associated with the Ni_8Nb line compound. In addition, in their work [43], DTA, XRD, EPMA, and optical microscopy analyses were all performed to obtain more comprehensive data. This improved the accuracy of the calculated solubility range of the δ phase to some extent. Below, Figure 2-8 shows the calculation Ni-Nb phase diagram by Chen and Du [43].

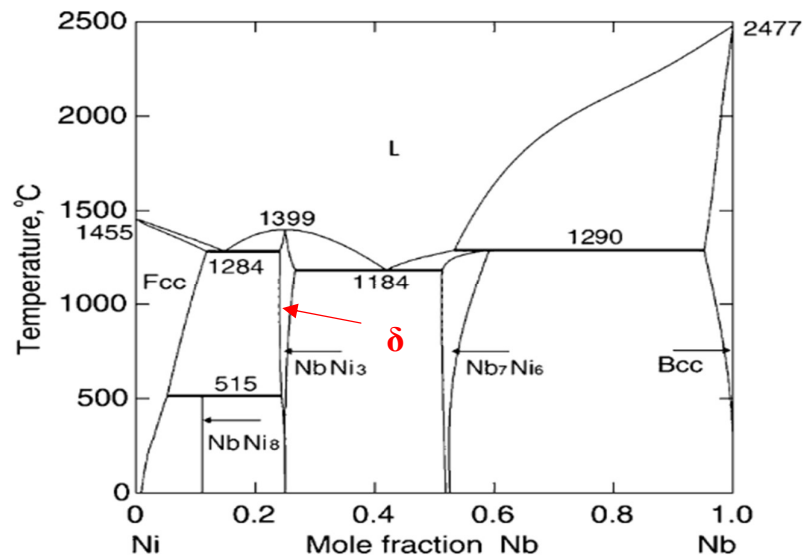


Figure 2-8 The Ni-Nb phase diagram calculated by Chen and Du [43]

2.5 Laves Phase

Laves phase is a common brittle precipitate in IN718, and it often appears as a bright superficial white particle [50]. As shown in Figure 2-9 shows below [51], small white particles in globular and irregular shapes precipitated along the interdendritic boundaries in IN718. They are identified as the Laves phase, and some of them might mix with the minor carbide (MC) phase that is segregated during the fast solidification process. When the alloy contains a large number of refractory elements such as Mo, W, and Ta, the formation of Laves phase is promoted [34]. Besides, the Laves phase consumes a large amount of solution strengthening

element Nb, which is an important element for the strengthening phases and the matrix. Hence, the alloy's mechanical properties, such as creep and fatigue, are seriously reduced when Laves phase forms [50].

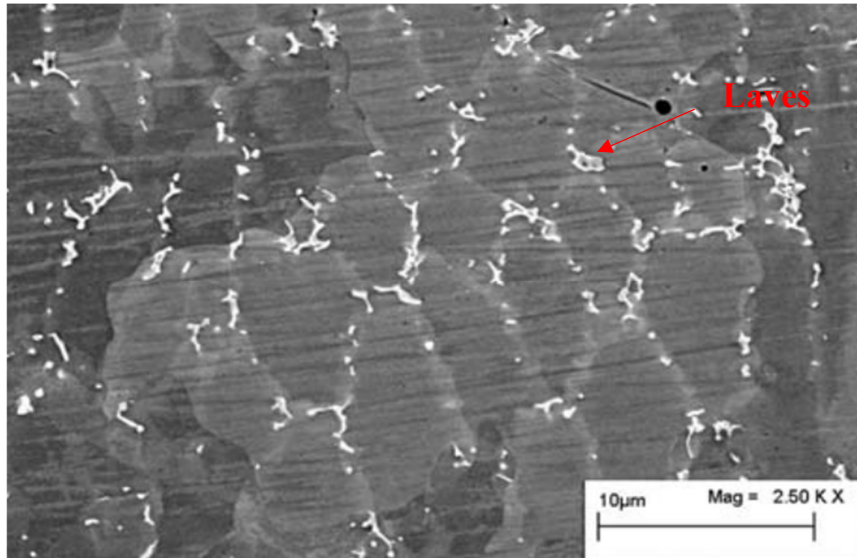


Figure 2-9 high-magnification SEM picture of the as-deposited IN718 sample [51]

According to the chemical composition of Laves phase, binary systems containing Laves phase are identified. It should be noted that the Laves phase in IN718 appears as a C14 hexagonal structure. Therefore, the binary systems discussed here also focus on the Laves phase with this particular structure. There are four main binary systems that contain Laves phase (C14): Cr-Ti, Cr-Nb, Fe-Nb, Fe-Ti.

Cr-Ti system is a relatively complex system, which includes three different structures (C14, C15, and C36) of Laves phase. This system had been critically assessed by Murray [52]. The presence of the C36 Laves phase prototype (the β -TiCr₂ phase) has been controversial in the literature [53]. Chen *et al.* [54] only took into account the C14 and C15 Laves phases in this system and modified the homogeneity ranges of these phases. McQuillan *et al.* [55] then measured the congruent transformation temperature of the γ -TiCr₂ to β -TiCr₂ at 1633 K. As for the thermodynamic description, the substitutional model is used to describe the liquid phase

and the terminal solid solution, and the sublattice model was used to describe the intermediate solid solution. Ghosh [57] then also built his assessment for Laves in the Cr-Ti and Cr-Ti-V systems. The Laves phase (C14, C15, and C36 are described by a two-sublattice model assuming antistructure atoms on both sublattices in his modelling [57]. The calculated thermodynamic quantities and phase diagrams are in good accord with the corresponding experimental data. Recently, Pavlu *et al.* [56] established a new description of the phases. In their report [56], the enthalpies of formation of all end-members of the three Laves phases at 0 K were calculated using the first principal method and combined with a CALPHAD based optimization to determine the Gibbs energy descriptions of each phase. They reported Cr-Ti phase diagram is shown in Figure 2-10 where C14 Laves is highlighted with a red dotted frame.

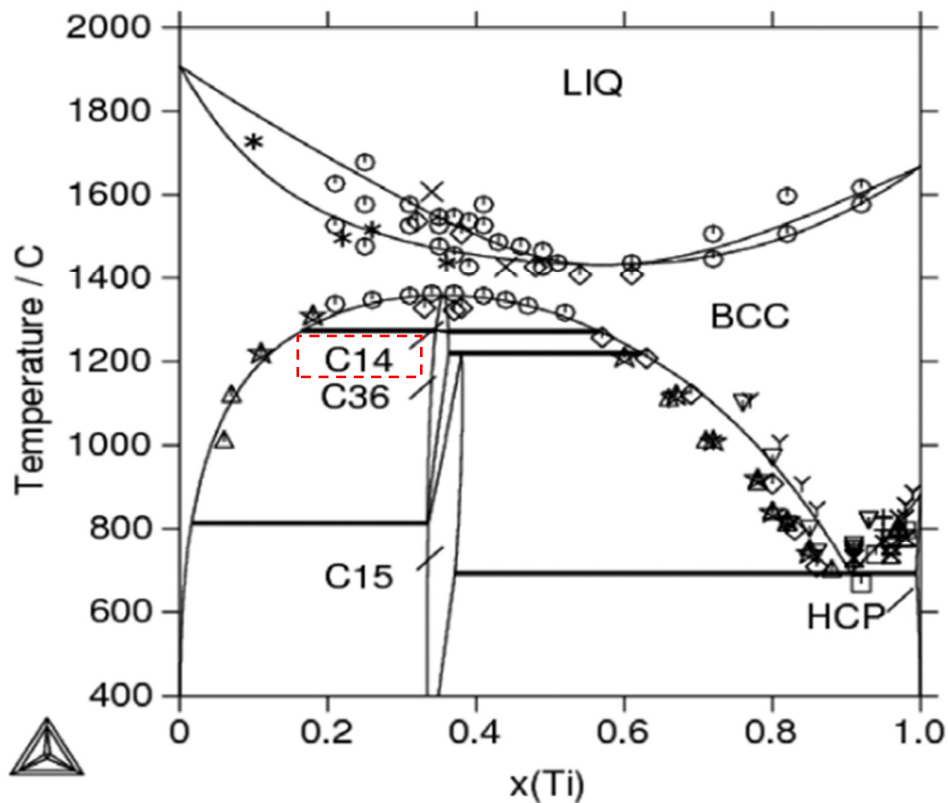


Figure 2-10 The calculated Cr-Ti phase diagram [56]

The Cr–Nb binary system has Laves phase with C15 and C14 forms. Elyutin *et al.* [58] studied the solid phase boundaries in this system. Then, Venkatraman and Neumann [59] determined the phase boundaries of the Laves phases. It is worth noting that Pan *et al.* [60] proposed for the first time that the C14 Laves phase exists in the system when the temperature is higher than 1858 K. Then, Thoma and Perepezko [61] verified the presence of C14 using X-ray diffraction. Recently, Pavlu *et al.* [62] reassessed the Laves phases in the system using the first-principles results at 0 K, which also included Laves with C14 and C15 structural forms. They reported the phase diagram is shown in Figure 2-11 [62]. Later, Hai-Jin Lu *et al.* [63] reported a thermodynamic description of the system using pseudo-potential VASP code to calculate the total energies of Laves phases. They also performed the phonon calculations for the C14 Laves to analyze the phase stability at elevated temperatures, which helps get the more accurate calculated melting temperature of C14 Laves. However, they did not mention C15 Laves in their calculation Cr-Nb phase diagram.

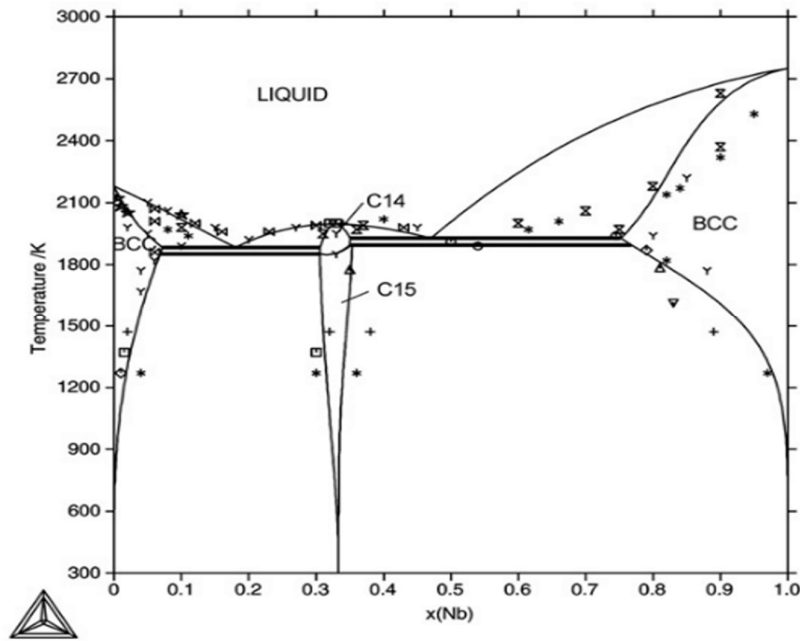


Figure 2-11 The calculated Cr-Nb phase diagram with superimposed experimental results [62]

As for Laves phase in the Fe-Ti and Fe-Nb systems, they both show typical C14 hexagonal structure. A first assessment of the Fe-Ti system was performed in 1978 by Kaufman and Nesor [64], followed by Murray [65], who assessed the same system in 1987. After that, a limited number of new phase diagram data were reported. With the improvement of experimental means, phase boundary and solubility data become accessible. In 1998, Dumitrescu and Hillert [66] comprehensively compared the previous experimental data and the modelling phase diagram of this system. They established a new assessment with particular attention to the properties of volatile solutions of Ti in liquid Fe. In 1999, Kumar [67] evaluated the system and used a three sublattice model for the Laves phase in the system, including a better description of its homogeneity range compared with experimental data. The phase diagram reported by Kumar [67] is shown in Figure 2-12. For the Fe-Nb system, Paul and Swartzendruber [68] were the first to evaluate the system and included a C14-type Laves phase. Recently, the homogeneity range of the Laves phase Fe_2Nb was determined at 1100 °C [69] and 1200 °C [70] by electron probe microanalysis (EPMA). Then, Balam *et al.* [71] observed the Laves phase by EDS analysis of diffusion couples between 950 and 1200 °C. Laves phase in this system was also initially modeled as a line compound, and then the sublattice model was performed to obtain more accurate results. In the work by Lu *et al.* [72] on the Fe-Nb-Zr ternary system, the Laves phase was described by two sublattices to simplify the extrapolation to ternary. Moreover, in the recent work by Vob *et al.* [73], they performed an electron probe microanalysis (EPMA) to obtain more precise data about the homogeneity range of C14 and also reported the re-calculated phase diagram of Fe-Nb. The re-calculated phase diagrams by Vob *et al.* [73] is shown in Figure 2-13.

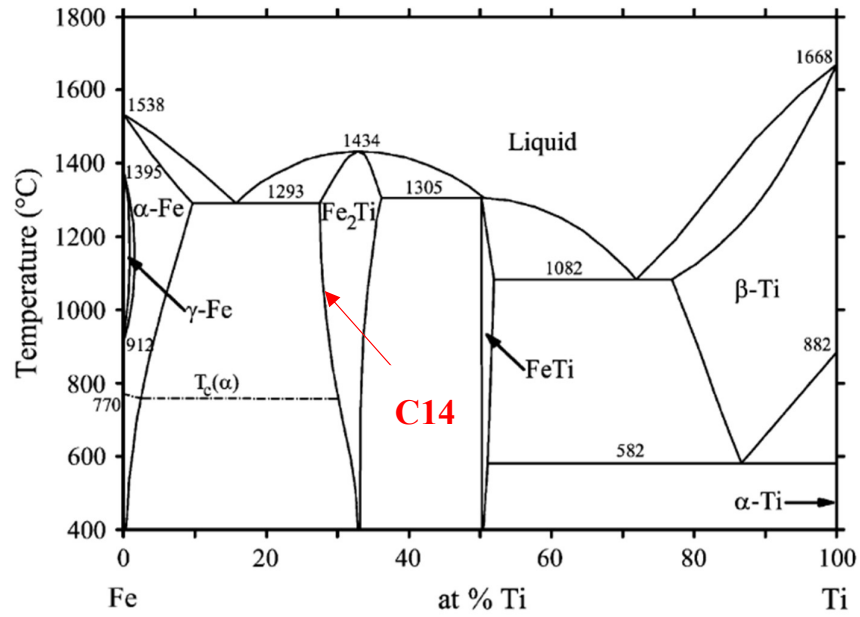


Figure 2-12 The calculated Fe-Ti phase diagram [67]

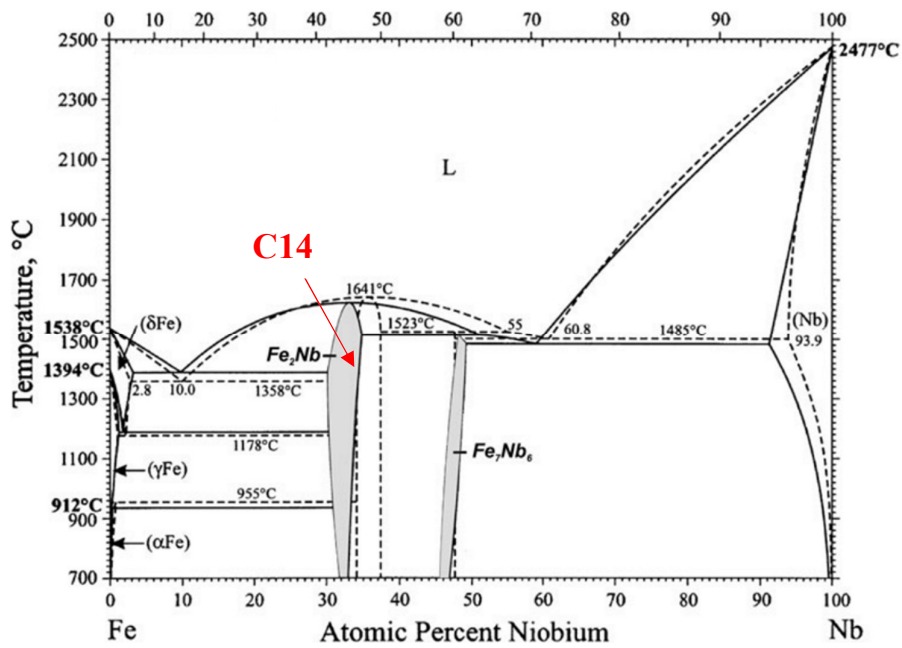


Figure 2-13 The calculated Fe-Nb phase diagram with an overlay of the previous thermodynamic assessment [73]

2.6 Carbides

The carbides that exist in the IN718 alloy are mainly NbC with a face-centered cubic lattice structure. In addition, there are small amounts of $M_{23}C_6$, M_6C , and M_7C_3 carbides reported in the literature [6,7]. Carbides form as gray particles within the grain and the grain boundaries with 'blocky' irregular shapes. Some articles [7,34,74] pointed out that intra-granular and inter-granular carbides can enhance strength by limiting dislocation movements, but their contribution is small compared to that of γ'' . However, the precipitation of MC carbide may cause the dislocations to concentrate at the interface between the matrix and the MC carbide leading to the formation of microcracks which result in the inter-granular fracture [7].

Chapter 3 Thermodynamic Modelling

In this chapter, basic theories of thermodynamic modelling and extrapolation to high-order systems are described.

The CALculation of PHase Diagrams (CALPHAD) method, which was initially introduced by Kaufman *et al.* [75] in the 1970s, and then with the development of computer technology and related software, became a very useful approach for materials thermodynamic calculations. In this study, FactSage [76] is mainly used for modelling and calculations. The core idea of CALPHAD is that the phase diagram is a representation of the equilibrium phases of the system. Hence, according to the known thermodynamic phase equilibrium data, the thermodynamic descriptions of phases in low-order systems can be determined and optimized using Gibbs energy minimization method. Moreover, the Gibbs free energy of these phases can be extrapolated further to high order system. Therefore, the CALPHAD method could be applied to model the thermodynamic properties of each phase and predict the behaviour of multi-component system. The final purpose of CALPHAD is to advance computational thermodynamics by developing self-consistent thermodynamics databases based on critical assessments of existing data, which will help to design new materials and understand various industrial processes. The CALPHAD method is one of the most effective methods for predicting complex thermochemical processes in multi-component systems. Figure 3.1 shows a flow chart summarizing the CALPHAD method [77].

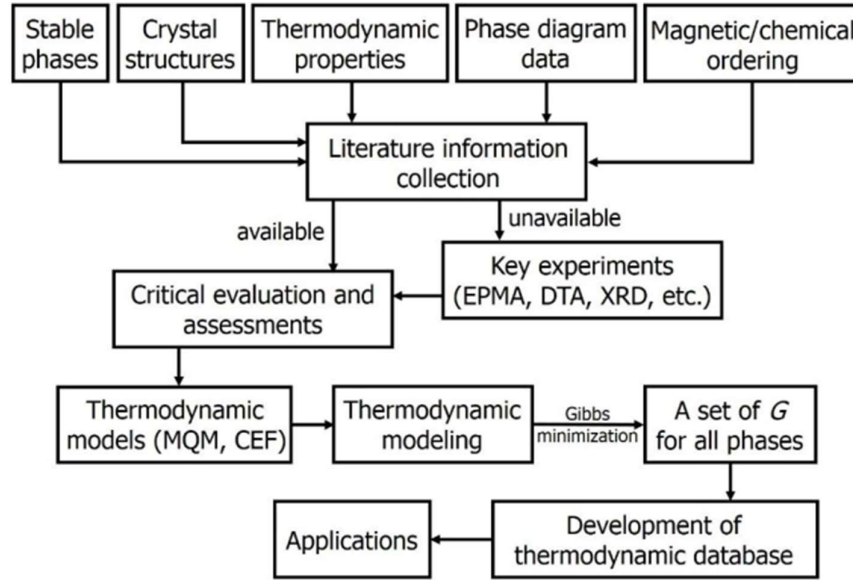


Figure 3-1. Flow chart of the thermodynamic optimization using the CALPHAD method [77]

3.1 Basic Thermodynamic Principle

The key to the thermodynamic calculation is to find an accurate Gibbs free energy equation to describe each phase in the system. By minimizing the total Gibbs free energy, the phase diagram at equilibrium can be calculated. In general, according to the second law of thermodynamics, the criterion for the system to reach equilibrium at constant temperature and pressure can be obtained. Suppose that the system contains total C components and total ϕ phases coexisting in equilibrium. The thermodynamic equilibrium is reached under constant temperature and pressure, when the total free energy of the system reaches the minimum value ($i=1,2, 3... C; \phi=\alpha, \beta... \psi$), i.e.,

$$G = \sum_{i=1}^C \sum_{\phi=\alpha}^{\psi} G_i^{\phi} = \min \dots \dots \dots (3.1)$$

In addition, from the chemical potential perspective, the i component in the system has the same chemical potential in each phase. This means that the system is in equilibrium when,

$$\mu_i^\alpha = \mu_i^\beta = \dots = \mu_i^\psi \dots\dots\dots (3.2)$$

In the formula above $\mu_i^\alpha = \left. \frac{\partial G^\alpha}{\partial n_i^\alpha} \right|_{T,P,n_j^\alpha \neq n_i^\alpha}$, G denotes the free energy of the phase in the system,

and n is the number of moles of the components in the different phases. According to the above two equilibrium criteria, two ways can be used to calculate the phase diagram. One of those is the Gibbs free energy minimization method, which considers species in each phase of the system as the variable and calculates the total minimized energy of the system at certain pressure and temperature. Another method is using the chemical potential of components in each phase, which solves the nonlinear equations to seek the state for components having equal chemical potentials in their phases. No matter which method is used to calculate the phase diagram, the Gibbs free energy expression of the thermodynamic function of each phase must be established first, i.e., to establish a thermodynamic model.

3.2 General Thermodynamic Model

When discussing the Gibbs free energy of a phase, especially for multicomponent systems, it can be defined as the following:

$$G_m = {}^{ref}G_m + {}^{id}G_m + {}^{Ex}G_m \dots\dots\dots (3.3)$$

Where ‘ref’ means the reference state of the mechanical mixing of pure components. It can be further described by the sum of pure components’ Gibbs free energy in equation 3.4, where 0G_i represents the standard Gibbs free energy of pure component i. When performing the thermodynamic modelling, 0G_i is generally taken from the European Thermodynamic research Group (SGTE), which is the database of pure components established by Dinsdale [78] for describing the relationship between the molar free energy of most pure elements and temperature.

$${}^{ref}G_m = \sum_{i=1}^c x_i {}^0G_i \dots\dots\dots (3.4)$$

$${}^{id}G_m = RT \ln \sum_{i=1}^c x_i \ln x_i \dots\dots\dots (3.5)$$

‘id’ in equation 3.3, denotes the ideal mixing contribution, which is the contribution of ideal entropy of mixing to free energy as in equation 3.5. And ‘Ex’ is the excess Gibbs free energy contribution when the interactions happen between the components. In general, the excess term of the Gibbs free energy also indicates the deviation of the thermodynamic properties of the phase from the ideal solution. The proper description of this term is significant to the thermodynamic model. Various expressions about this excess term have been proposed by making some approximations and assumptions regarding the behaviour of real systems.

3.3 Solution Model

If the interaction between the components in the solution is very weak, both mixing enthalpy (ΔH) and excess entropy of mixing (ΔS_{ex}) are negligible. This solution can be described by the ideal solution model, and its excess free energy is zero, i.e., $^{Ex}G_m = 0$. However, the reality is often complicated, and additional terms need to be added to describe the excess Gibbs free energy, so as to model the phase more accurately. Based on this, the following models are generally adopted for different purposes.

3.3.1 Regular Solution Model

The regular solution model was first proposed by Hildebrand *et al.* in 1929 [79] and is the most widely used. The main characteristics of the model are as follows: firstly, it is assumed that any atom in the solution has Z nearest neighbour atoms, Z is constant and independent of the type of central atom. In addition, the model assumes that the distribution of atoms in solution is completely disordered (excess entropy is equal to zero). Therefore, excess Gibbs of mixing can be expressed as:

$${}^E G_m = \sum_{i=1}^{C-1} \sum_{j=i+1}^C L_{ij} x_i x_j \dots\dots\dots (3.6)$$

Where L_{ij} is the interaction parameter for the excess Gibbs free energy term. For example, for simple binary systems 1-2, ${}^E G_m = L_{12} x_1 x_2$.

3.3.2 Associated Solution Model

The model of association solution is mainly used to describe the solution with short-range order. For example, in a binary system containing association compound A_pB_q , the molar Gibbs free energy of mixture can be expressed by the following equation

$$\begin{aligned}
 G_m &= {}^{ref}G_m + {}^{id}G_m + {}^{li}G_m \\
 G_m &= \left(y_A {}^{*0}G_A + y_B {}^{*0}G_B + y_{A_pB_q} G_{A_pB_q} \right) \\
 &\quad + RT \left(y_A \ln y_A + y_B \ln y_B + y_{A_pB_q} \ln y_{A_pB_q} \right) \dots\dots\dots (3.7) \\
 &\quad + \left(y_A y_B L_{AB} + y_A y_{A_pB_q} L_{AA_pB_q} + y_B y_{A_pB_q} L_{BA_pB_q} \right)
 \end{aligned}$$

Where X represents the molar fraction of elements A and B, and their total should be equal to 1 ($X_A + X_B = 1$). G represents the Gibbs free energy of the corresponding element and the associated substance; L is an interaction parameter. It is important to note that y denotes the mole fractions of the associated compound A_pB_q , and A and B are the elements. If 1 mole of A and 1 mole of B produces $n(A_pB_q)$ moles of A_pB_q , then n_A and n_B are the moles of A and B that are present in the association. And at the same time, the total number of moles in the system is $N = n_A + n_B + n(A_pB_q)$. Thus, $y_A = n_A/N$, $y_B = n_B/N$, $y(A_pB_q) = n(A_pB_q)/N$

3.3.3 Sublattice Model

The sublattice model was first proposed by Hillert *et al.* [80] in 1970. Because in many phases, the arrangement of different kinds of atoms is ordered, and one special atom tends to go into a particular lattice position. The sublattice model subdivides the lattice into several sublattices based on crystallographic information. For example, NaCl can be described as a simple cubic lattice, and it also can be treated as two intersecting face-centered cubic lattices, one of which is occupied by Na and the other by Cl. In order to use the sublattice model to accurately describe the solid solution, especially the solid solution with a special solubility range, each sublattice can be set containing multiple elements. The concept of dot matrix

fraction is introduced for calculating the Gibbs free energy because different lattices could contain more than one element. At the same time, attention need to be given the features and assumptions of the sublattice model when doing the modelling. First, it was assumed that each atom in one single sublattice is only adjacent to atoms in the other sublattice, and the interactions between each sublattice are ignored. The excess free energy is only related to the interactions between atoms in the same sublattice and the type of atoms in another sublattice. This means that the interactions between the lattices do not affect the excess free energy [81].

Due to the importance of this model to the current thesis, example of a simple binary sublattice model $(A, B)_p (C, D)_q$ is discussed below to explain the sublattice model in more details. The first lattice is occupied by A and B with the number of atoms N_A and N_B , and the second lattice is occupied by C and D with the number of atoms N_C and N_D . Where P and Q represent the ratio of the two lattices, from this, the lattice fraction can be calculated:

$$\begin{aligned} y_A &= \frac{N_A}{N_A+N_B} = 1 - y_B \\ y_C &= \frac{N_C}{N_C+N_D} = 1 - y_D \end{aligned} \dots\dots\dots (3.8)$$

Based on the above discussion, the ideal molar entropy of mixing can be deduced as:

$$\Delta S_m = pRT \sum_{i=1}^n y'_i \ln y'_i + qRT \sum_{j=1}^n y''_j \ln y''_j \dots\dots\dots (3.9)$$

Where superscripts ' and '' represent the first and second sublattices, respectively. For example, y'_i Represents the fraction of the components in the first sublattice [80].

Since in the sublattice model, entropy of mixing is ideal, so the excess free energy is only related to configurational entropy. Meanwhile, according to the previous hypothesis, there is no interaction between each lattice. So, the Gibbs free energy can be deduced [82]:

$$\begin{aligned} G = \sum_{i=1}^n \sum_{j=1}^n y'_i y''_j G_{ij} + pRT \sum_{i=1}^n y'_i \ln y'_i + qRT \sum_{j=1}^n y''_j \ln y''_j \\ + \sum_{j=1}^n y'_A y'_B y''_j L_{A,B;j} + \sum_{i=1}^n y''_C y''_D y''_j L_{i,C,D} \end{aligned} \dots\dots\dots (3.10)$$

The last two terms in the above equation represent the excess Gibbs free energy, where the parameter $L_{A,B;j}$ is the interaction parameter between A and B in the first lattice when the second sublattice is completely occupied by element j. The parameter $L_{i:C,D}$ has a similar meaning [80]. In addition, it is essential to note that in the above equation, the compound represented by G_{ij} , can be for either an actual or a hypocritical compound.

3.3.4 Interaction Parameters

In the regular solution model and the sublattice model, L_{ij} is the interaction coefficient between components, which is the vital term for thermodynamic modelling. In order to accurately describe the properties of the solution, L_{ij} can be expressed as a function of temperature and the components that make up the system. The relationship between L_{ij} and temperature can be written as follows [80]:

$$L_{ij} = a + bT + cT \ln(T) \dots \dots \dots (3.11)$$

In some thermodynamic modelling and phase diagram assessment, to reduce the limiting conditions and the number of parameters, the above equation is simplified as:

$$L_{ij} = a + bT \dots \dots \dots (3.12)$$

The common mathematical expressions for the relation between L_{ij} and components include Margules power function polynomials, Redlich-Kister polynomials, and Legendre polynomials. Many studies show that the Redlich-Kister polynomial has certain quasi-orthogonality, and its mathematical form is relatively simple, which is beneficial to building the model of a complex system [83]. Therefore, this representation has been widely used in recent years, and its specific mathematical expression is:

$$L_{12} = \sum_{j=0}^n {}^j L(x_1 - x_2)^j \dots \dots \dots (3.13)$$

Substitute equation (3.12) into equation (3.13) and then expand the polynomial to obtain the equation below [83]:

$$L_{ij} = (a_0 + b_0T) + (a_1 + b_1T)(x_1 - x_2) + (a_2 + b_2T)(x_1 - x_2)^2 + \dots \dots \dots (3.14)$$

3.4 Extrapolation and Assessment of Higher-Order Systems

Due to the difficulty of experimental measurement, the thermodynamic model of the multi-components system (i.e., ternary systems and higher) is usually obtained by extrapolation from the binary subsystems. This should give a reasonable first approximation for the higher-order system. Experimental data of multi-components systems are much less available than that of the binary system and ternary systems, so the information in the experimental phase diagram is difficult to meet the needs of practical material development. A large number of the experimental phase diagram and thermodynamic data of the sub-systems are required for the evaluation of the multi-component system of interest. Also, it is necessary to verify and optimize the phase diagram and thermodynamic data of the subsystem in order to establish a more accurate database. Extrapolation techniques include the well-known symmetric Kohler and Muggianu model also the asymmetric Toop model. Each model has its own advantages and disadvantages [84]. Usually, the choice of models is based on experience and the type of components and their chemical interactions. Different models will have some influence on the assessment results. For example, Chartrand and Pelton [76] reported that for dilute solutions, the Kohler or Toop model gives better descriptions for partial properties in the ternary system than the Muggianu model. Lukas *et al.* [84] explained the above three extrapolation methods graphically, as shown in Figure 3-2. Additionally, another symmetrical Colinet model is similar to Kohler and Muggianu models, but treats the three contributions from the three binary systems with different ratios.

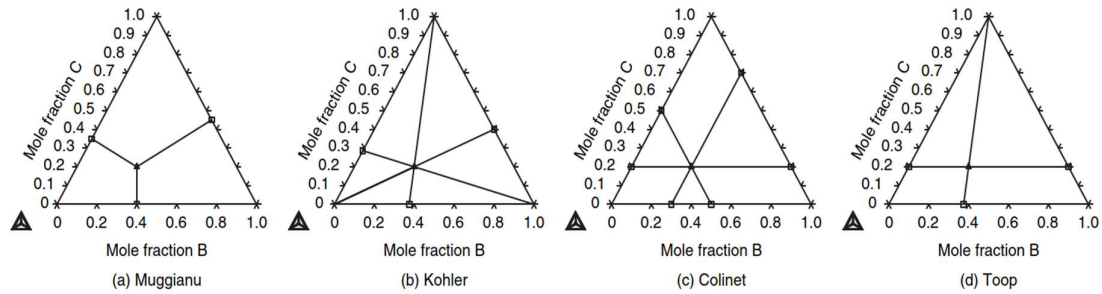


Figure 3-2 Graphical explanation about four different ternary extrapolation methods [84]

Since IN718 alloy contains at least eight elements, it is difficult to build a fully validated database from scratch, which requires a lot of experimentation and validation. In addition, if the assessment of each subsystem is established and then extrapolated to higher-order systems, there will be quite a lot of redundant assessment. Thus, in this work, is established by merging of the corresponding Gibbs energies of the phase from the binary systems. For example, the Laves phase exists in two binaries systems, A-B and A-C. Meanwhile, it is assessed via sublattice models: $(A, B)_2(A, B)$ and $(A, C)_2(A, C)$. When Laves phase needs to be modeled in the ternary A-B-C model, it can be modeled as $(A, B, C)_2(A, B, C)$. At this time, the parameters $G_{B:C}$ and $G_{C:B}$ are unassessed. It can be treated as zero in most cases, or if there is assessed data about the B-C subsystem, it can be applied. This approach proved to be reliable, especially when modelling higher-order systems in the absence of some experimental data (e.g., solubility range and activity)

Chapter 4 Calculation Results of the Binary Systems in the IN718 Alloy

This chapter explains the process of building a modified, customized database for 3D-printed IN718 and explains the modelling results of each phase. In addition, some calculation results of Thermo-Calc for IN718 are included for comparison. Finally, relevant experiments are carried out to verify the current models.

4.1 γ' Phase

As mentioned in chapter 3, the main form of the γ' phase in IN718 is $\text{Ni}_3(\text{Al}, \text{Ti})$. Al and Ti have a reciprocal substitution in the lattice. The stable phase only exists in Al-Ni with the form of Ni_3Al ($L1_2$), while the relevant compound with the same elemental ratio (A_3B) in the remaining two subsystems shows other crystal types. For modelling this phase, the sublattice model is suitable due to the solubility range of this phase, as discussed earlier. In the binary alloy, the configuration of the sublattice model is that both two elements dissolve into each of the lattices, i.e. $(A, B)_3(A, B)$. It is worth noting that, in the higher-order system, there is a lack of experimental solubility data, especially for the IN718 system. Therefore, in this work, three elements are introduced to dissolve in each lattice by default, i.e. $(\text{Ni}, \text{Al}, \text{Ti})_3(\text{Ni}, \text{Al}, \text{Ti})$. It is necessary to review the crystallographic information of the stable γ' phase to ensure that the correct phase present in the IN718 alloy. The available crystallographic information of the stable γ' phase is summarized in Table 4-1.

Table 4-1. Crystallographic information of γ' phase

Phase	Crystal information		Reference
γ'	Prototype	AuCu ₃	[85] [51]
	Pearson Symbol	cP4	
	Strukturbericht Designation	L1 ₂	
	Space Group	Pm $\bar{3}$ m	
	Space Group Number	221	
	Lattice Parameters	a=b=c=3.92447; $\alpha=\beta=\gamma=90^\circ$	

Table 4-2 lists the calculated phase equilibria transitions related to the γ' in the Al-Ti system. The calculated eutectic and peritectic temperatures in this work are 1650.6 K and 1651.9 K, respectively, which show good agreement with all the available data listed in Table 4-2. In particular, it is important to note the close agreement between these values and the measurement of Verhoeven *et al.* [86].

Table 4-2 Comparison between this work and the different experimental results from the literature of the γ' invariant equilibria in the Al-Ni system

Reaction	Type	Compositions of Ni (at. %)	Temperature (K)	Reference
Liquid + Al_FCC \rightarrow γ'	Peritectic	0.7606; 0.7950; 0.7725	1651.9	This work
		0.7560; 0.7880; 0.7600	1643.4	[87]
		0.7600; 0.7880; 0.7700	1649	[88]
		0.7583; 0.8128; 0.7644	1643.2	[89]
		0.7550; 0.7850; 0.7616	1645	[90]
Liquid \rightarrow AlNi_BCC + γ'	Eutectic	0.7554; 0.7057; 0.7703	1650.6	This work
		0.7460; 0.7070; 0.7500	1642.2	[87]
		0.7555; 0.7180; 0.7660	1646	[88]
		0.7571; 0.6946; 0.7647	1642.9	[89]
		0.7520; 0.7100; 0.7600	1642	[90]

The optimized thermodynamic parameters for γ' phase are shown in Table 4-3, where the Gibbs energy of pure elements Ni, Al, and Ti are all taken from the SGTE database [78], as mentioned earlier. Except for the γ' phase, the rest of the phases in the Al-Ni system are taken from the FTLite database. The parameters of the hypothetical and real end-members of the γ' phase were optimized in this work. In addition, when describing the excess Gibbs free energy of a phase, it was necessary to use the minimum number of interaction parameters (L) to avoid complicating the model as complex models result in less accurate extrapolation to higher order systems [24,28]. Figure 4-1 shows that the calculated phase diagram agrees reasonably with the available experimental data in the literature. In some of the earlier work, the γ' phase is considered as a stoichiometric compound which is not correct and hence not compared with this work. The phase without homogenous range will affect the liquidus temperature and result in a steeper liquidus and inaccurate phase transformation temperatures. Attention was paid to have the homogeneity range of γ' in the Al-Ni (Figure 4-1) consistent with the work of Hilpert *et al.* [90] and Bremer *et al.* [91] because they are the most recent.

Table 4-3 Optimized thermodynamic parameters of the γ' phase in the IN718 alloy

Phase	End-members	Thermodynamic description & parameter	
		ΔG (J/mol-atom)	Interaction parameter L (J/mol-atom)
γ' (Ni,Al,Ti) ₃ (Ni,Al,Ti)	Ni:Ni	$G_{Ni:Ni}^{Ni3Ni} - 3 * G_{Ni}^{Fcc} - 1 * G_{Ni}^{Fcc} = 20000$	$L_{Al:Ni,Al} = -155700$ $L_{Ni:Ni,Al} = -155700$ $L_{Al,Ni:Ni} = -7500$ $L_{Al,Ni:Al} = -7500$
	Ni:Ti	$G_{Ni:Ti}^{Ni3Ti} - 3 * G_{Ni}^{Fcc} - G_{Ti}^{Hcp} = -151504 + 24.15 * T$	
	Ni:Al	$G_{Ni:Al}^{Ni3Al} - 3 * G_{Ni}^{Fcc} - G_{Al}^{Fcc} = -184944 + 34.5 * T$	
	Ti:Ni	$G_{Ti:Ni}^{Ti3Ni} - 3 * G_{Ti}^{Hcp} - G_{Ni}^{Fcc} = 2885 + 1.17 * T$	
	Ti:Al	$G_{Ti:Al}^{Ti3Al} - 3 * G_{Ti}^{Hcp} - G_{Al}^{Fcc} = 20000 + 1.05 * T$	
	Ti:Ti	$G_{Ti:Ti}^{Ti3Ti} - 3 * G_{Ti}^{Hcp} - G_{Ti}^{Hcp} = 20000$	
	Al:Ti	$G_{Al:Ti}^{Al3Ti} - 3 * G_{Al}^{Fcc} - G_{Ti}^{Hcp} = -135344 + 37 * T$	
	Al:Ni	$G_{Al:Ni}^{Al3Ni} - 3 * G_{Al}^{Fcc} - G_{Ni}^{Fcc} = -114744 + 34.55 * T$	
Al:Al	$G_{Al:Al}^{Al3Al} - 3 * G_{Al}^{Fcc} - G_{Al}^{Fcc} = 20000$		

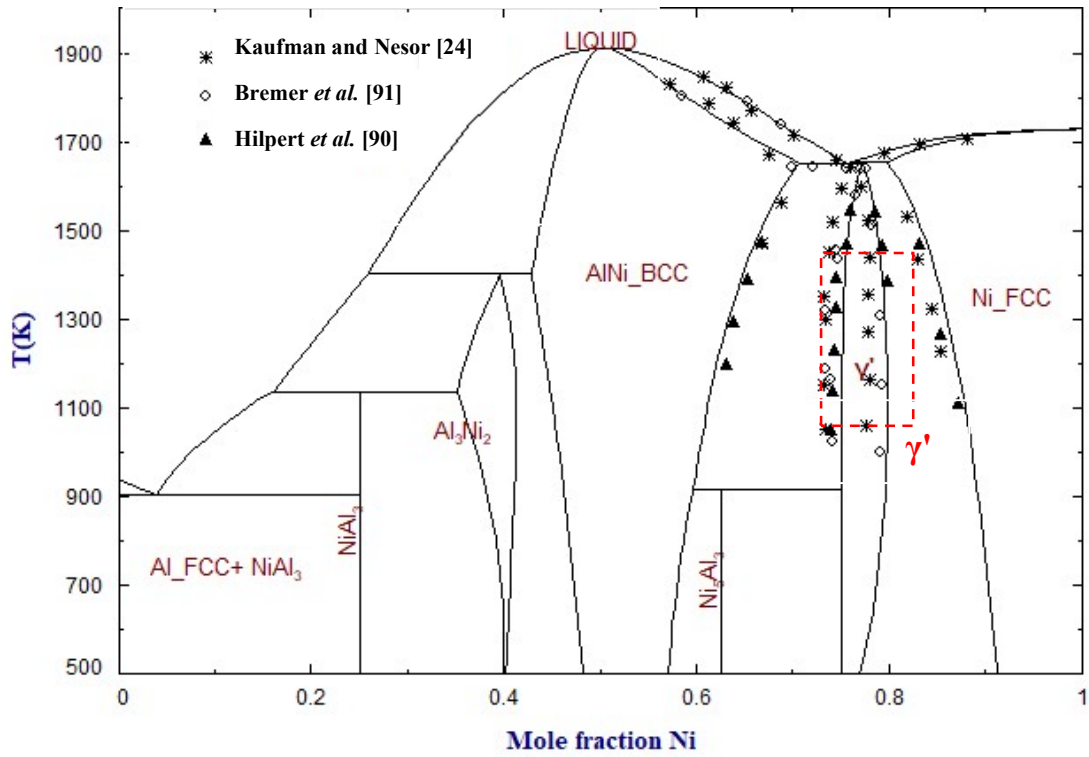


Figure 4-1 The calculated Al-Ni phase diagram using the optimized parameter of γ' combined with the FTlite database. Phase boundaries of γ' (highlighted with red dotted frame) are compared with the relevant data from the literature.

4.2 γ'' Phase

From previous research, it is understood that γ'' is a metastable phase with a BCT crystal structure based on Ni_3Nb . It has been mentioned that a small amount of Ti to stabilizes this phase [34]. According to the investigation of the binary phase diagrams, γ'' with the crystal structure of BCT in the binary system exists in Al-Ti and Al-Nb binary system, but it has a narrow solubility, almost a linear compound. The γ'' (Al_3Ti) in the Al-Ti system is described by the sublattice model, which allows elements to be dissolved into two lattices, namely, $(\text{Ti}, \text{Al})_3(\text{Ti}, \text{Al})$ [49]. For the thermodynamic description of Al_3Nb in the Al-Nb system, He *et al.* [49] also adopted the same approach, randomly mixing each element into two lattices. However, an alternative approach has been proposed instead of using the complete mixing in two sublattices, Zhu *et al.* [92] used the $(\text{Al}, \text{Nb})_3(\text{Nb})$ model to represent γ'' in the Al-Nb system, which changes the homogeneity range 25-100% Nb. This can reduce the number of adjustable parameters in the model. However, Du *et al.* [88] reverted to the $(\text{Ni}, \text{Nb})_3(\text{Al}, \text{Nb}, \text{Ni})$ model to describe γ'' (Ni_3Nb) in the ternary Al-Nb-Ni system. It is worth noting here that, there is also a stable γ'' phase in the ternary Al-Nb-Ti system. Cupid *et al.* [40] modeled it using a sublattice model that allows the three elements to uniformly dissolve into two lattices resulting in an accurate assessment. They also reported that experiments show a significant widening of the range of homogeneity with respect to the Al concentration in the ternary Al-Nb-Ti system. The elemental composition of the IN718 alloy used in the 3D printing contains a large amount of Fe along with many other trace elements, including Ti and Al. Therefore, including these elements in the sublattice model improves the high-order thermodynamic model and makes it more suitable for the IN718 alloy. In the current work, the $(\text{Al}, \text{Nb}, \text{Ni}, \text{Ti})_3(\text{Al}, \text{Nb}, \text{Ni}, \text{Ti}, \text{Fe})$ model is used to describe γ'' in the IN718 alloy. The crystallographic information for the γ'' is summarized in the Table 4-4.

Table 4-4 Crystallographic information of the γ'' phase

Phase	Crystal information		Reference
γ''	Prototype	Al_3Ti	[34] [93]
	Pearson Symbol	tI8	
	Strukturbericht Designation	D0 ₂₂	
	Space Group	I4/mmm	
	Space Group Number	139	
	Lattice Parameters	$a=b=3.62; c=7.41;$ $\alpha=\beta=\gamma=90^\circ$	

Table 4-5 lists the phase equilibria transitions of the γ'' phase in the Al-Nb binary system. The congruent melting temperature of the γ'' phase is calculated to be about 2005 K in this work. Additionally, the eutectic and peritectic reactions related to the γ'' phase are also listed in Table 4-5. Compared with the experimental results from the literature, it can be seen that they are in good agreement. Especially, the pyrometric results of γ'' from Witusiewicz *et al.* [94] and the DTA results measured by Stein *et al.* [95] both show close values to this work. Also, the LTA (levitation thermal analysis) + DTA results measured by Jorda *et al.* [96] are consistent with this work. For the Al-Ti system, it is worth noting that although the same model was used for describing γ'' , the literature [97] modeled the adjacent phases γ'' differently, which affected the phase boundary of γ'' to a certain extent. For example, when Saunders [97] modeled the adjacent line compound as $\text{Al}_{11}\text{Ti}_5$, the γ'' -related peritectic reaction occurred at about 1627.7 K ($\text{Liquid} + \text{Al}_{11}\text{Ti}_5 \rightarrow \gamma''$). However, Kattner *et al.* [28] set the line compound as Al_5Ti_2 , so that the peritectic reaction takes place at about 1663 K ($\text{Liquid} + \text{Al}_5\text{Ti}_2 \rightarrow \gamma''$). Thus, only the experimental results from the literature [88-90,92] were used to compare in this work, as

shown in Table 4-6. The peritectic temperature calculated in this work is close to the temperature obtained from the literature, and the error is within ± 10 K.

Table 4-5 Comparison between this work and the different experimental results from the literature of the γ'' invariant equilibria in the Al-Nb system

Reaction	Type	Compositions of Al (at. %)	Temperature (K)	Reference
Liquid $\rightarrow \gamma''$	Congruent	0.75	2005	This work
		0.75	1953 ± 5	[96]
		---	1988 ± 6	[94]
		---	2000	[95]
Liquid $\rightarrow \gamma'' + \text{Nb}_2\text{Al}$	Eutectic	0.56; 0.44; 0.74	1851	This work
		0.55; 0.42; ---	1863 ± 5	[96]
		---; 0.46; ---	1845 ± 7	[94]
Liquid + $\gamma'' \rightarrow \text{Al_FCC}$	Peritectic	0.99; 0.75; 0.98	936	This work
		---; 0.75; ---	931 ± 5	[94]
		---; ---; 0.99	934 ± 0.5	[92]

Table 4-6 Comparison between this work and the different experimental results from the literature of the γ'' invariant equilibria in the Al-Ti system

Reaction	Type	Compositions of Al (at. %)	Temperature (K)	Reference
Liquid + Al ₁₇ Ti ₈ → γ''	Peritectic	0.73; 0.68; 0.76	1655	This work
		0.75; 0.71; 0.78	1698	[98]
		0.75; 0.71; 0.81	1660	[94]
Liquid + γ'' → Al_FCC	Peritectic	0.99; 0.75; 0.98	935	This work
		0.99; 0.75; 0.98	938.7	[94]
		0.99; 0.75; 1	938	[100]

The optimized thermodynamic parameters of γ'' in the IN718 alloy are shown in the following Table 4-7, where the Gibbs energy of pure elements are all taken from the SGTE database [78] as mentioned earlier. Except for the γ'' , the rest of the phases in the Al-Nb phase diagram are taken from the FTlite database. Parameters of the hypothetical and real end-members of the γ'' phase were adjusted and optimized in this work. For the Al-Nb binary system, the calculated and enlarged phase diagrams (Figure 4-2 and 4-3) show detailed comparison of the γ'' phase by superimposing with the experimental data points from the literature [94-96,98]. Especially in the recent year 2019, Silva *et al.* [98] used electron probe microanalysis (EPMA) measurements to confirm the composition of this system. Their work [98] is given high weight and the current work is consistent with their measurement. For the Al-Ti binary system, although the experimental solubility range of the γ'' phase in high order systems is still uncertain, there are some accurate thermodynamic descriptions of the γ'' phase in the Al-Ti binary system [40,47,90,92]. Similar sublattice structure to assess γ'' has been adopted in the present work. The only difference is that other elements in IN718 have been added to describe the γ'' phase. The calculated phase diagram and enlarged part in the vicinity of γ'' are shown in Figure 4-4

and 4-5, which exhibits great agreement with the most recent available experimental data reported by Palm *et al.* [99].

Table 4-7 Optimized thermodynamic parameters of γ'' in the IN718 alloy

Phase	End-members	Thermodynamic description & parameter	
		ΔG (J/mol-atom)	Interaction parameter L (J/mol-atom)
γ'' (Al,Nb,Ni,Ti) ₃ (Al,Nb,Ni,Ti,Fe)	Ni:Ni	$G_{Ni:Ni}^{Ni3Ni} - 3 * G_{Ni}^{Fcc} - G_{Ni}^{Fcc} = 40000$	L _{Al, Nb, Ti} = -5000 L _{Nb, Al, Nb} = 120000 L _{Al, Ti, Nb} = -50000
	Ni:Fe	$G_{Ni:Fe}^{Ni3Fe} - 3 * G_{Ni}^{Fcc} - G_{Fe}^{Bcc} = 14666.66 + 19.32 * T$	
	Ni:Nb	$G_{Ni:Nb}^{Ni3Nb} - 3 * G_{Ni}^{Fcc} - G_{Nb}^{Bcc} = 5517.21 + 9.74 * T$	
	Ni:Ti	$G_{Ni:Ti}^{Ni3Ti} - 3 * G_{Ni}^{Fcc} - G_{Ti}^{Hcp} = -151504.79 + 24 * T$	
	Ni:Al	$G_{Ni:Al}^{Ni3Al} - 3 * G_{Ni}^{Fcc} - G_{Al}^{Fcc} = -153134.4 - 3.8 * T$	
	Ti:Ni	$G_{Ti:Ni}^{Ti3Ni} - 3 * G_{Ti}^{Hcp} - G_{Ni}^{Fcc} = 2885.11 + 1.17 * T$	
	Ti:Al	$G_{Ti:Al}^{Ti3Al} - 3 * G_{Ti}^{Hcp} - G_{Al}^{Fcc} = 20000 + 1.05 * T$	
	Ti:Ti	$G_{Ti:Ti}^{Ti3Ti} - 4 * G_{Ti}^{Hcp} = 40000$	
	Ti:Fe	$G_{Ti:Fe}^{Ti3Fe} - 3 * G_{Ti}^{Hcp} - G_{Fe}^{Bcc} = 9194.45 + 9.6 * T$	
	Ti:Nb	$G_{Ti:Nb}^{Ti3Nb} - 3 * G_{Ti}^{Hcp} - G_{Nb}^{Bcc} = 20000 + 1.05 * T$	
	Al:Ti	$G_{Al:Ti}^{Al3Ti} - 3 * G_{Al}^{Fcc} - G_{Ti}^{Hcp} = -144592 - 36.98 * T$	
	Al:Ni	$G_{Al:Ni}^{Al3Ni} - 3 * G_{Al}^{Fcc} - G_{Ni}^{Fcc} = -192095.8 + 45.9 * T$	
	Al:Nb	$G_{Al:Nb}^{Al3Nb} - 3 * G_{Al}^{Fcc} - G_{Nb}^{Bcc} = -136008 - 24.13 * T$	
	Al:Fe	$G_{Al:Fe}^{Al3Fe} - 3 * G_{Al}^{Fcc} - G_{Fe}^{Bcc} = -107465.5 + 24 * T$	
	Al:Al	$G_{Al:Al}^{Al3Al} - 3 * G_{Al}^{Fcc} - G_{Al}^{Fcc} = 40000$	
	Nb:Al	$G_{Nb:Al}^{Nb3Al} - 3 * G_{Nb}^{Bcc} - G_{Al}^{Fcc} = 20000 + 1.5 * T$	
	Nb:Nb	$G_{Nb:Nb}^{Nb3Nb} - 4 * G_{Nb}^{Bcc} = 40000$	
	Nb:Ni	$G_{Nb:Ni}^{Nb3Ni} - 3 * G_{Nb}^{Bcc} - G_{Ni}^{Fcc} = 1839 + 3.27 * T$	
	Nb:Ti	$G_{Nb:Ti}^{Nb3Ti} - 3 * G_{Nb}^{Bcc} - G_{Ti}^{Hcp} = 20000 + 1.5 * T$	
	Nb:Fe	$G_{Nb:Fe}^{Nb3Fe} - 3 * G_{Nb}^{Bcc} - G_{Fe}^{Bcc} = 9500 + 10.2 * T$	

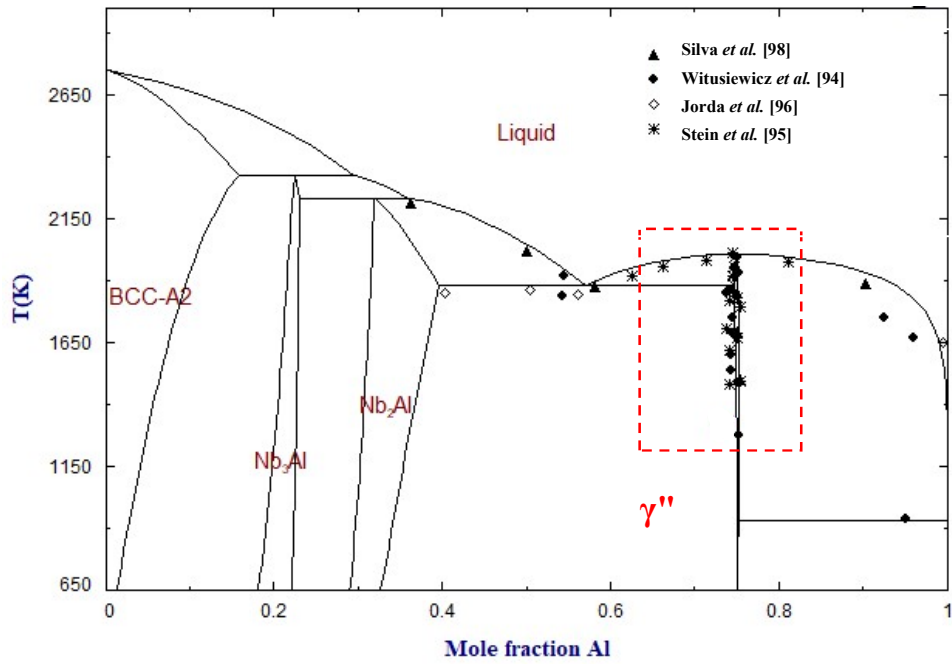


Figure 4-2 The calculated Al-Nb phase diagram using the optimized parameter of γ' combined with the FTlite database. Phase boundaries of γ'' are compared with the relevant data from the literature.

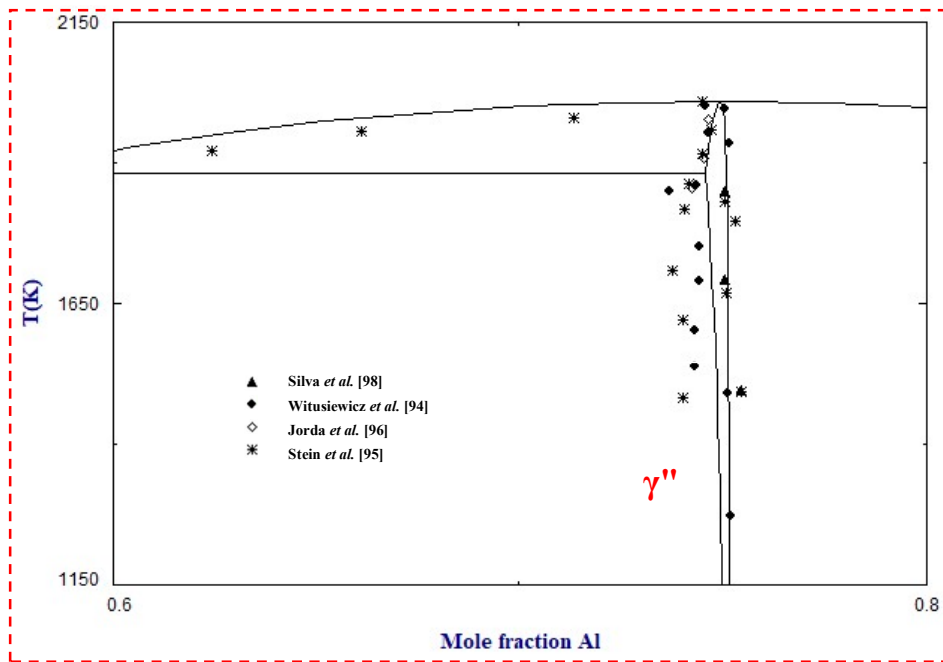


Figure 4-3 Enlarged area in the vicinity of γ'' shown in Figure 4-2.

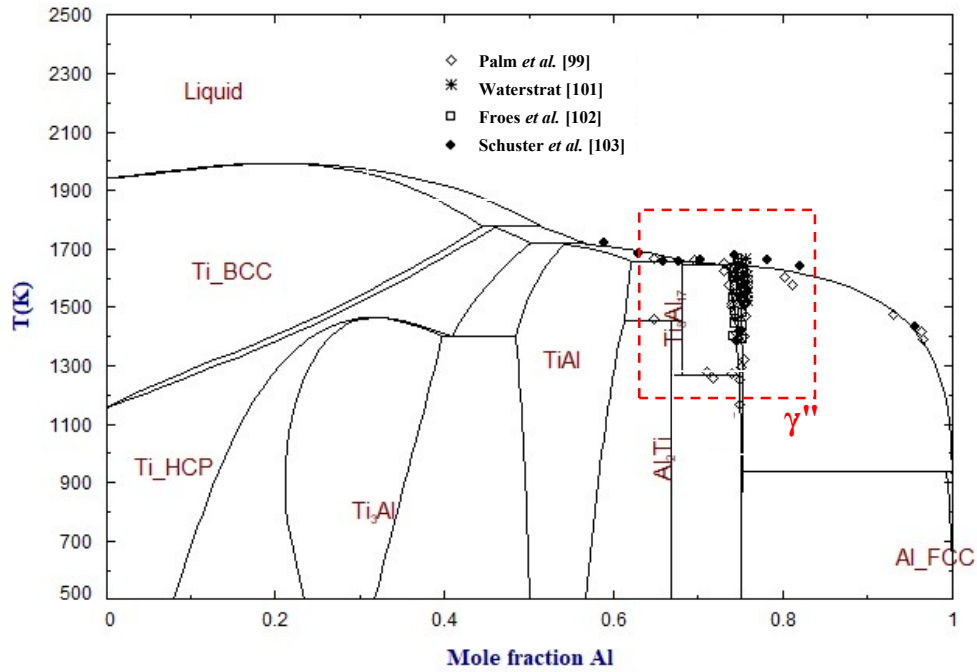


Figure 4-4 The calculated Al-Ti phase diagram using the optimized parameter of γ'' combined with the FTlite database. Phase boundaries of γ'' are compared with the relevant data from the literature.

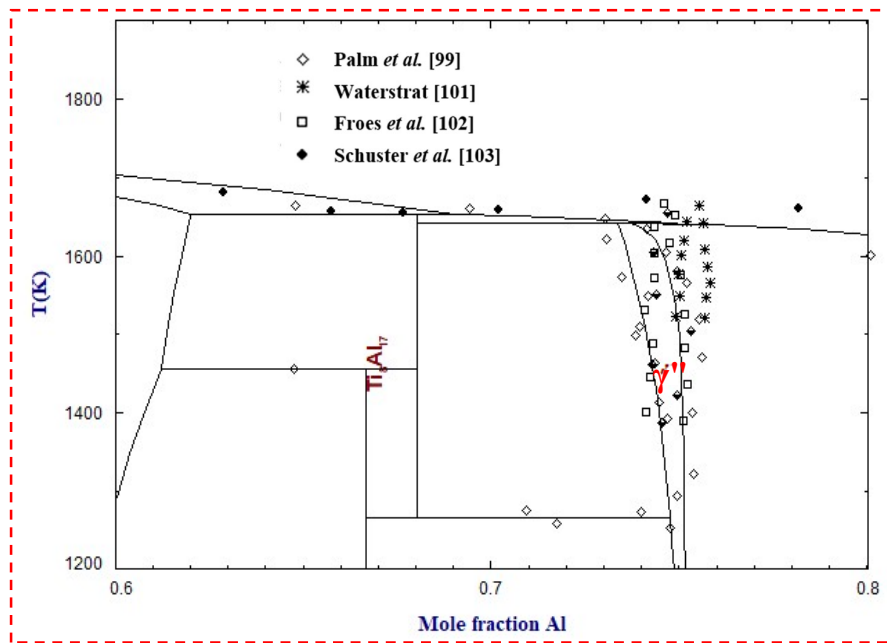


Figure 4-5 Enlarged area in the vicinity of γ'' shown in Figure 4-4.

4.3 Laves Phase

The Laves phase is a common brittle precipitate in IN718 with bright white particles. A high proportion of it is detrimental to the mechanical properties of IN718. In addition, due to the complexity of its composition and uncertainty of its occurrence, detailed experimental and modelling results of this phase are lacking. Hence, it is necessary to build a thermodynamic description for this phase. According to the discussion earlier, the Laves phase has $(\text{Ni, Cr, Fe})_2(\text{Nb, Ti, Mo})$ chemical composition. However, Ferreri *et al.* [34] described the Laves phase with the $(\text{Ni, Cr, Fe})_2(\text{Nb, Ti})$ model. Qi *et al.* [51] reported the elemental distribution of the interdendritic Laves phase using EDS analysis of printed IN718, and found that it is rich in Ni, Nb, Mo, and Cr but with very low Al content. A stable Laves phase exists in the Cr-Ti, Cr-Nb, Fe-Nb and Fe-Ti systems. As discussed in chapters 2 and 3, to describe the homogenous ranges of this phase accurately, the two respective elements are set to mix within each lattice. Following this approach, the $(\text{Ni, Nb, Fe, Ti, Cr})_2(\text{Ni, Nb, Fe, Ti, Cr})$ model is used in the current work to describe the Laves phase in the IN718 alloy. The model is consistent with all the literature and reproduces the homogeneity range. The Mo element has conflict when doing calculations via FactSage and has been found to be a trace element in the IN718 system. Therefore, it has not been included in the customized database. However, another thermodynamic calculation software Thermo-Calc [104] was used to calculate equilibrium and non-equilibrium conditions of the IN718 alloy with Mo. These results will be discussed in chapter 5. The crystallographic information for the Laves phase is summarized in Table 4-8 below.

Table 4-8 Crystallographic information of the Laves phase

Phase	Crystal information		Reference
Laves	Prototype	MgZn ₂	[34] [51]
	Pearson Symbol	hP12	
	Strukturbericht Designation	C14	
	Space Group	P6 ₃ /mmc	
	Space Group Number	194	
	Lattice Parameters	a=b=5.15; c=8.48; $\alpha=\beta=90^\circ$; $\gamma=120^\circ$	

The optimized thermodynamic parameters of Laves phase (C14) are shown in Table 4-9, where the Gibbs energy of pure elements are all taken from the SGTE database [78] as mentioned earlier. Similarly, when doing the phase diagram calculation, except for the Laves phase, the rest of the phases in the following sub-binary systems are taken from the FTlite database [76]. Parameters of the hypothetical and real end-members were adjusted and optimized in this work.

Table 4-9. Optimized thermodynamic parameters for the Laves phase in the IN718 alloy

Phase	End-members	Thermodynamic description & parameter	
		ΔG (J/mol-atom)	Interaction parameter L (J/mol-atom)
Laves (Ni,Nb,Fe,Ti,Cr) ₂ (Ni,Nb,Fe,Ti,Cr)	Ni:Ni	$G_{Ni:Ni}^{Ni2Ni} - 2 * G_{Ni}^{Fcc} - G_{Ni}^{Fcc} = 15000$	
	Ni:Fe	$G_{Ni:Fe}^{Ni2Fe} - 2 * G_{Ni}^{Fcc} - G_{Fe}^{Bcc} = 12827.59 + 1.32 * T$	$L_{Fe: Nb, Fe} = -2379+13.92*T$
	Ni:Nb	$G_{Ni:Nb}^{Ni2Nb} - 2 * G_{Ni}^{Fcc} - G_{Nb}^{Bcc} = 3878.14 + 5.31 * T$	
	Ni:Ti	$G_{Ni:Ti}^{Ni2Ti} - 2 * G_{Ni}^{Fcc} - G_{Ti}^{Hcp} = 3678.14 + 2.05 * T$	
	Ni:Cr	$G_{Ni:Cr}^{Ni2Cr} - 2 * G_{Ni}^{Fcc} - G_{Cr}^{Bcc} = 13319.62 + 5.86 * T$	$L_{Nb: Nb, Fe} = -2379+13.92*T$
	Ti:Ni	$G_{Ti:Ni}^{Ti2Ni} - 2 * G_{Ti}^{Hcp} - G_{Ni}^{Fcc} = -70305.59 + 8.57 * T$	$L_{Fe, Nb: Nb} = 114+44.22*T$
	Ti:Cr	$G_{Ti:Cr}^{Ti2Al} - 2 * G_{Ti}^{Hcp} - G_{Cr}^{Bcc} = 15009.68 + 1.05 * T$	
	Ti:Ti	$G_{Ti:Ti}^{Ti2Ti} - 2 * G_{Ti}^{Hcp} - G_{Ti}^{Hcp} = 15000$	$L_{Fe, Nb: Fe} = 114+44.22*T$
	Ti:Fe	$G_{Ti:Fe}^{Ti2Fe} - 2 * G_{Ti}^{Hcp} - G_{Fe}^{Bcc} = 9194.45 + 9.6 * T$	
	Ti:Nb	$G_{Ti:Nb}^{Ti2Nb} - 2 * G_{Ti}^{Hcp} - G_{Nb}^{Bcc} = 20000 + 1.05 * T$	$L_{Fe, Ti: Ti} = 10500$
	Cr:Ti	$G_{Cr:Ti}^{Cr2Ti} - 2 * G_{Cr}^{Bcc} - G_{Ti}^{Hcp} = -1879.79 - 5.91 * T$	$L_{Fe: Ti, Fe} = 4200$
	Cr:Ni	$G_{Cr:Ni}^{Cr3Ni} - 2 * G_{Cr}^{Bcc} - G_{Ni}^{Fcc} = 1858.43 + 5.9 * T$	
	Cr:Nb	$G_{Cr:Nb}^{Cr2Nb} - 2 * G_{Cr}^{Bcc} - G_{Nb}^{Bcc} = -5430 - 10.57 * T$	$L_{Cr, Ti: Cr} = 47634.9$
	Cr:Fe	$G_{Cr:Fe}^{Cr2Fe} - 2 * G_{Cr}^{Bcc} - G_{Fe}^{Fcc} = 9168.81 + 24 * T$	$L_{Cr, Ti: Ti} = 47634.9$
	Cr:Cr	$G_{Cr:Cr}^{Cr2Cr} - 2 * G_{Cr}^{Bcc} - G_{Cr}^{Bcc} = 15000$	$L_{Cr: Ti, Cr} = 23360$
	Nb:Cr	$G_{Nb:Cr}^{Nb2Cr} - 2 * G_{Nb}^{Bcc} - G_{Cr}^{Bcc} = 229560 - 4.46 * T$	
	Nb:Nb	$G_{Nb:Nb}^{Nb2Nb} - 2 * G_{Nb}^{Bcc} - G_{Nb}^{Bcc} = 15000$	$L_{Ti: Ti, Cr} = 23360$
	Nb:Ni	$G_{Nb:Ni}^{Nb2Ni} - 2 * G_{Nb}^{Bcc} - G_{Ni}^{Fcc} = 1839.07 + 1.27 * T$	$L_{Cr, Nb: Nb} = 88673$
	Nb:Ti	$G_{Nb:Ti}^{Nb2Ti} - 2 * G_{Nb}^{Bcc} - G_{Ti}^{Hcp} = 20000 + 1.46 * T$	
	Nb:Fe	$G_{Nb:Fe}^{Nb2Fe} - 2 * G_{Nb}^{Bcc} - G_{Fe}^{Bcc} = 103200 - 17.45 * T$	$L_{Cr, Nb: Cr} = 88673$
	Fe:Fe	$G_{Fe:Fe}^{Fe2Fe} - 2 * G_{Fe}^{Bcc} - G_{Fe}^{Bcc} = 15000$	$L_{Nb: Nb, Cr} = 18511$
	Fe:Ti	$G_{Fe:Ti}^{Fe2Ti} - 2 * G_{Fe}^{Bcc} - G_{Ti}^{Hcp} = -103200 + 25.41 * T$	$L_{Cr: Nb, Cr} = 18511$
	Fe:Cr	$G_{Fe:Cr}^{Fe2Cr} - 2 * G_{Fe}^{Bcc} - G_{Cr}^{Bcc} = 18308.58 - 1.45 * T$	
	Fe:Ni	$G_{Fe:Ni}^{Fe2Ni} - 2 * G_{Fe}^{Bcc} - G_{Ni}^{Fcc} = 20137.97 - 0.5 * T$	
Fe:Nb	$G_{Fe:Nb}^{Fe2Nb} - 2 * G_{Fe}^{Bcc} - G_{Nb}^{Bcc} = -73200 + 17.45 * T$		

The Cr-Ti binary system includes three different structures (C14, C15, and C36) of Laves phase, but only C14 exists in IN718. Thus, this work mainly focuses on the modelling of the C14 phase to include it in the customized database, while the other two types of Laves are taken from the FSstel database [76] from FactSage software. It is worth noting that FSstel has ambiguous naming of these three phases. As Lukas *et al.* [16] mentioned in their book, in some thermodynamic databases, the phase names used for several important crystal structures do not belong to any of the general nomenclature systems. For example, the names FCC structure and BCC were initially designated for Bravais lattices (face-centered cubic and body-centered cubic), but they are very commonly used as names for the crystal structures denoted by prototype, Strukturbericht, and Pearson symbols as Cu-type, A1, cF4, and W-type, A2, cI2, respectively. For instance, in some thermodynamic modelling software, “ordered bcc” is used for the CsCl-type (B2, cP2) and FeAl₃-type (cF16) structures that in fact have cubic primitive or face-centered cubic Bravais lattices, respectively; “ordered fcc” on the other hand is used for the CuAu-type (L1₀, tP2) and Cu₃Au-type (L1₂, cP4) structures which have tetragonal or cubic primitive Bravais lattices, respectively. Based on this, when employing phase modelling, crystal structure and nomenclature of specific phases should be examined in detail to avoid mistakes.

When optimizing this phase diagram, not enough experimental data is available about the enthalpy of formation for end-members, especially, Cr₂Ti. And the standard enthalpy of formation of the stable end-member Cr₂Ti of the Laves phases is assessed differently in different articles. For example, Cupid *et al.* [105] used -2741 J/mol, which is significantly larger than the values obtained from the ab-initio work of Pavlu *et al.* (-30486 J/mol) [56]. Thus, in this work, the value -1789 J/mol is adopted, which is within the assessment range of suggestion from Cupid *et al.* [105] (from -1779 J/mol to -29569 J/mol).

Due to lack of experimental descriptions of the homogeneity ranges and polymorphic transformation of C36 and C15, only C14 can be compared with experimental data as shown in Figure 4-6. Additionally, there are also missing experimental data about some of the reactions related to C36 and C15. Thus, only some of the other calculated invariant reaction data are listed in Table 4-10 and marked as calculation results from the literature. It could be concluded that calculation of the Cr-Ti phase diagram and the invariant reactions are consistent with the experimental results from the literature. Especially, the Cr_BCC \rightarrow Laves_C14 reaction that is shows great consistent with the data from the literature. By comparing with the latest studies on this reaction, Ghosh [106] and Cupid *et al.* [105] reported this reaction to occur at about 1642 K and 1643 K respectively, which is also close to the calculated value in this work at about 1645 K. For the peritectoid reaction (Cr_BCC + Laves_C14 \rightarrow Laves_C36), the temperature is found as 1542 K in this work, which is also close to the results of Minaeva *et al.* [107] as 1545 K.

Table 4-10 Comparison between this work and different experimental results from the literature of the C14-Laves invariant equilibria in the Cr-Ti system

Reaction	Type	Compositions of Cr (at. %)	Temperature (K)	Reference
Cr_BCC → C14	Congruent	0.65	1645	This work
		0.65	1647 ± 1	[108]
		0.65	1639	[109] *
		0.65	1648	[110]
		0.65	1642	[106] *
		0.65	1643	[105] *
C14 + Cr_BCC → C36	Peritectoid	0.64; 0.46; 0.64	1542	This work
		0.64; 0.44; 0.64	1544	[106] *
		0.63; 0.41; 0.63	1545	[105] *
		0.63; 0.42; 0.63	1543	[109]

Note: * calculation results from the literature

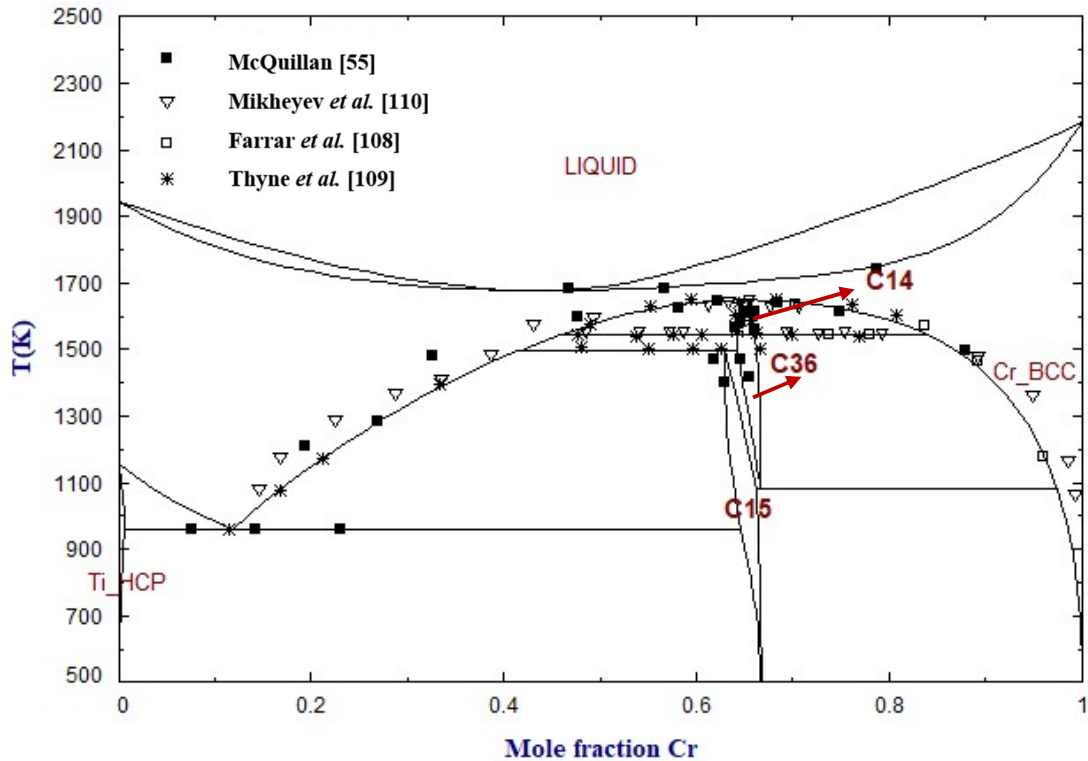


Figure 4-6 The calculated Cr-Ti phase diagram using the optimized parameter of C14 Laves combined with the FTLite database. Phase boundaries of C14 Laves are compared with the relevant data from the literature.

The Cr-Nb binary system has two types of Laves phase with structures C14 and C15. There are not enough experimental data of the two eutectic reactions related to C14. Thus, some of the other calculated invariant equilibria reaction data are listed when comparing with the current results. The details are shown in Table 4-11. It could be seen that the two eutectic reactions and the congruent melting temperature of C14 are all close to the experimental and modelling results from the literature. Especially, the congruent melting temperature of the C14 in this work (2002 K) reveals good agreement. This indicates that the thermodynamic description of the C14 phase in the Cr-Nb system accurately assesses the Gibbs free energy of this phase and the phase region. The calculated Cr-Nb phase diagram is shown in the Figure 4-7.

Table 4-11 Comparison between this work and different experimental results from the literature of the C14-Laves invariant equilibria in the Cr-Nb system

Reaction	Type	Compositions of Cr (at. %)	Temperature (K)	Reference
Liquid → C14 + Cr_BCC	Eutectic	0.71; 0.83; 0.93	1892.64	This work
		0.70; 0.88; 0.94	1893 ± 40	[111]
		0.71; 0.82; 0.93	1893	[112]
Liquid → C14 + Nb_BCC	Eutectic	0.25; 0.52; 0.65	1924.68	This work
		0.15; 0.50; 0.61	1923 ± 50	[111]
		0.25; 0.52; 0.65	1924	[112] *
Liquid → C14	Congruent	0.67	2001.55	This Work
		0.67	2001± 20	[111]
		0.67	2001	[112]
		0.67	2000	[61] *
		0.67	2002	[63] *

Note: * calculation results from the literature

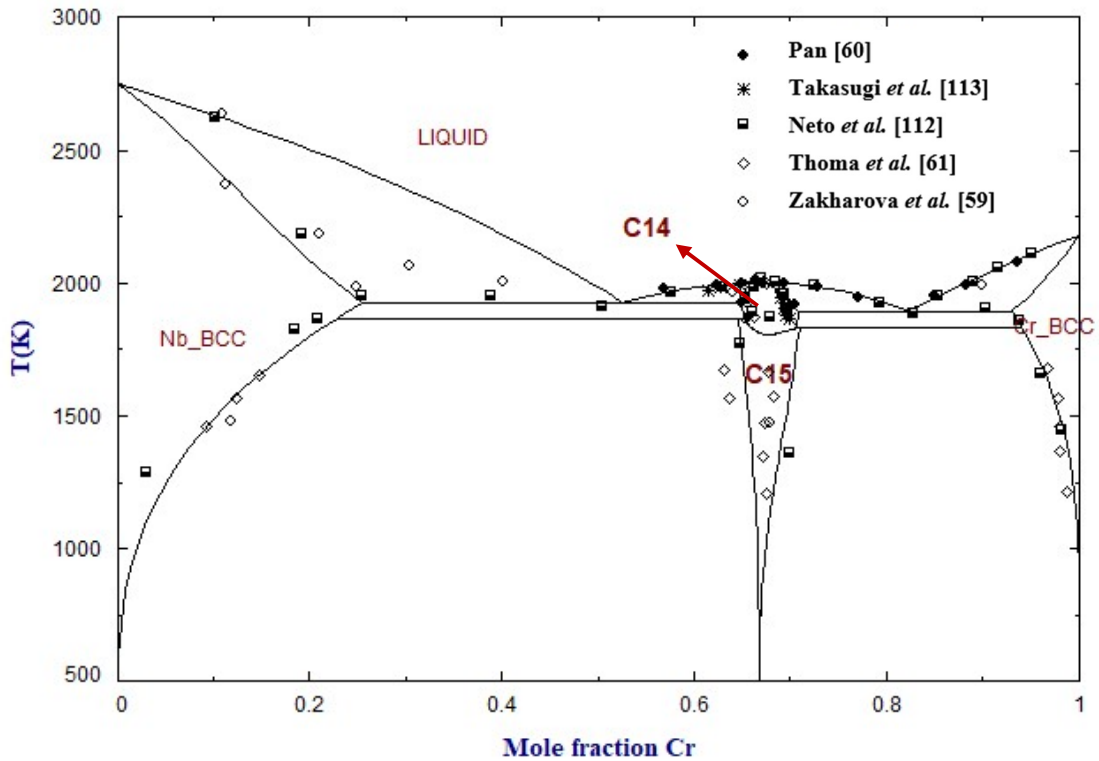


Figure 4-7 The calculated Cr-Nb phase diagram using the optimized parameter of C14 Laves combined with the FTlite database. Phase boundaries of C14 Laves are compared with the relevant data from the literature.

The Fe-Nb binary system has only the C14 type of Laves phase. Some experimental data on the region of this phase are available. The comparison of experimental invariant equilibria and this work are shown in Table 4-12 below. It could be found that the eutectic reaction, peritectic reaction and the congruent melting temperature of C14 are all close to the experimental results from the literature [73,114,115]. Especially, the eutectic reaction of C14 in this work reveals good agreement with the experimental result of both Vob *et al.* [73] and Bejarano *et al.* [114].

Table 4-12 Comparison between this work and different experimental results from the literature of the C14-Laves invariant equilibria in the Fe-Nb system

Reaction	Type	Compositions of Nb (at. %)	Temperature (K)	Reference
Liquid \rightarrow C14 + Fe_BCC	Eutectic	0.03; 0.09; 0.31	1642.3	This work
		0.03; 0.08; 0.25	1646 \pm 1	[73]
		0.03; 0.1; 0.32	1643	[114]
Liquid + C14 \rightarrow Fe ₇ Nb ₆	Peritectic	0.35; 0.51; 0.49	1811.54	This work
		0.38; 0.52; 0.47	1796 \pm 2	[73]
		0.37; 0.56; 0.49	1793	[114]
Liquid \rightarrow C14	Congruent	0.33	1911.35	This Work
		0.33	1913	[115]
		0.33	1903	[114]
		0.33	1909.3	[116]

Figure 4-8 shows the calculated Fe-Nb system along with the experimental data from different literature sources. It can be seen that the thermodynamic description of the homogeneity range of the C14 Laves phase and the Fe-rich side eutectic reaction in this work are consistent with the accurate EPMA experimental data of Bejarano *et al.* [114]. The calculated solubility range of the Laves phase at 1642 K in this work is about 30.4 - 33.6 at. % Nb. And it comes about 32.1 - 34.9 at. % Nb as the temperature reaches 1810 K. These results are in good agreement with the narrower solubility range (32-37.5 at. % Nb; 32-37 at. % Nb; 30-35 at. % Nb) measured by EPMA by Vob *et al.* [73].

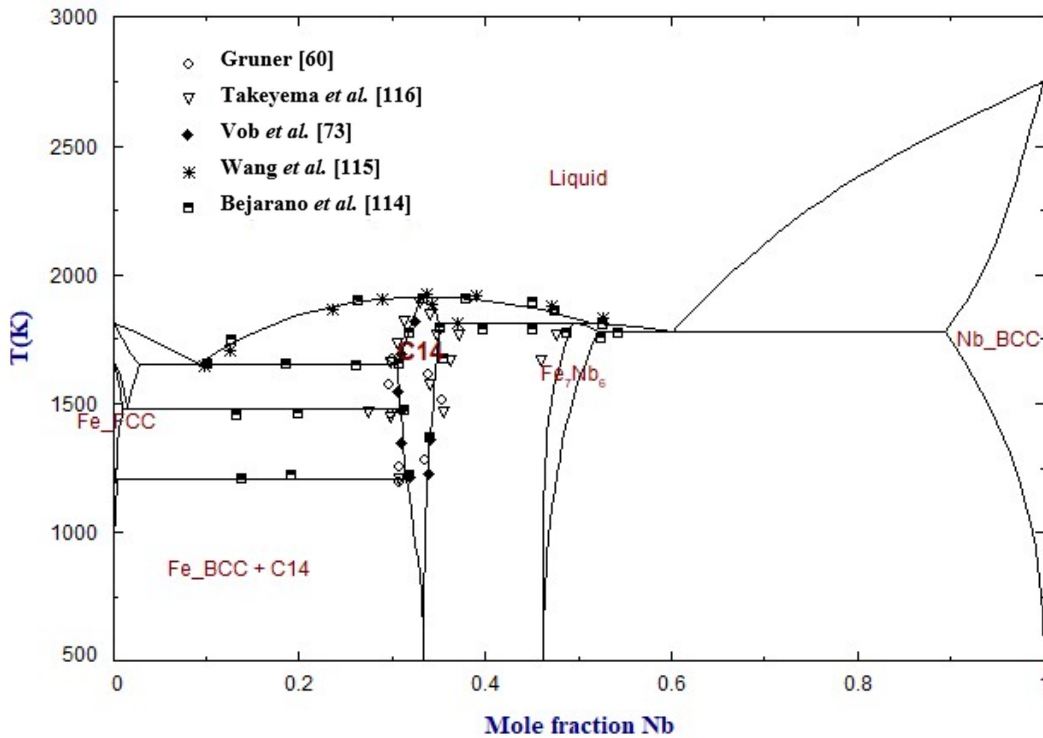


Figure 4-8 The calculated Fe-Nb phase diagram using the optimized parameter of C14 Laves combined with the FTlite database. Phase boundaries of C14 Laves are compared with the relevant data from the literature.

For the Fe-Ti system, Dumitrescu *et al.* [66] mentioned that some of the old versions of modelling results, such as Murray's [65] were not accurate due to the lack of experimental information. Different thermodynamic calculations have different interpretations of the melting point and homogeneity range of FeTi in the literature, which affects the overall equilibrium reactions of the system. The higher the melting point of FeTi, the more likely it is to have a eutectic reaction between this compound and the Fe-side. This explains the reason why some authors treated it as a peritectic reaction, but others, such as Wierzba *et al.* [117], recently considered it as a eutectic reaction instead. Thus, only the experimental data from the literature are listed and used to compare with the current work. The calculated invariant reactions and compositions related to the C14 Laves phase are summarized in Table 4-13. It is worth noting that this system requires further experimental information for a more comprehensive

thermodynamic assessment. The relevant Fe-Ti calculated phase diagram is shown in Figure 4-9, superimposing with the experimental data from the literature, which exhibits great agreement with the most recent available experimental data reported by Qiu *et al.* [118].

Table 4-13 Comparison between this work and different experimental results from the literature of the C14-Laves invariant equilibria in the Fe-Ti system

Reaction	Type	Compositions of Ti (at. %)	Temperature (K)	Reference
Liquid \rightarrow C14 + Fe_BCC	Eutectic	0.09; 0.16; 0.31	1574.04	This work
		0.098; 0.16; 0.30	1566	[119]
		0.09; 0.17; 0.28	1561	[120]
		---; ---; 0.30	1559	[121]
Liquid \rightarrow C14	Congruent	0.34	1695	This work
		0.34	1709	[119]
		0.35	1704	[120]
Liquid + C14 \rightarrow FeTi	Peritectic	0.39; 0.5; 0.51	1607.03	This work
		0.39; 0.49; ---	1600.1	[119]
		---; 0.47; ---	1603.17	[120]
		0.4; ---; ---	1614	[121]

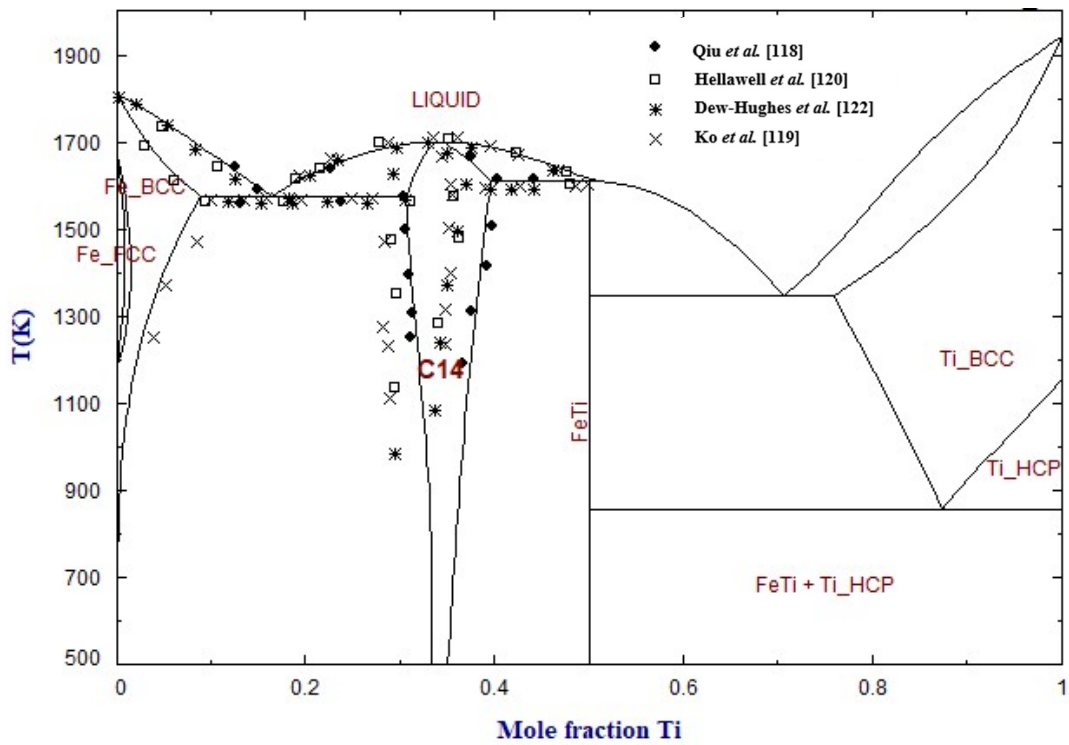


Figure 4-9 The calculated Fe-Ti phase diagram using the optimized parameter of C14 Laves combined with the FTlite database. Phase boundaries of C14 Laves are compared with the relevant data from the literature.

4.4 δ Phase

The delta phase is an important stable phase with an orthogonal D0a structure. It has the Ni₃Nb primary composition. The crystallographic information for the Ni₃Nb δ phase is summarized in Table 4-14 below. However, a recent paper by Ferreri *et al.* [34] provided the nominal composition of the delta phase in the IN718 alloy, which included Ti dissolved in the lattice. Meanwhile, from the phase diagram perspective, the delta phase is stable in the Ni-Nb binary system and Ni-Nb-Ti ternary system. This indicates that Ti has a certain solubility in the Delta phase. Hence, in order to establish a more comprehensive thermodynamic description of delta in IN718, Ti is introduced in the sublattice model in this work. As Santhy and Kumar [123] suggested, due to the solubility of Ti in the delta phase, the (Nb, Ni)₃(Nb, Ni, Ti) sublattice model is used. By doing so, two additional hypothetical end members have been introduced compared with a relatively simple Ni-Nb binary type description. This work follows the same idea of description, and some excess free energy parameters are modified. These optimized thermodynamic parameters are shown in Table 4-15, where the Gibbs energy of pure elements are all taken from the SGTE database [78]. And except for the δ phase, the rest of the phases are taken from the FTLite database.

Table 4-14 Crystallographic information of the δ phase

Phase	Crystal information		Reference
Delta	Prototype	Cu ₃ Ti	[34] [123]
	Pearson Symbol	oP8	
	Strukturbericht Designation	D0a	
	Space Group	Pmmn	
	Space Group Number	59	
	Lattice Parameters	a=5.12;b=4.26; c=4.57; $\alpha=\beta=\gamma=90^\circ$	

Table 4-15 Optimized thermodynamic parameters for the δ phase in the IN718 alloy

Phase	End-members	Thermodynamic description & parameter	
		ΔG (J/mol-atoms)	Interaction parameter L (J/mol-atoms)
Delta (Ni,Nb) ₃ (Ni,Nb,Ti)	Ni:Ni	$G_{Ni:Ni}^{Ni3Ni} - 3 * G_{Ni}^{Fcc} - * G_{Ni}^{Fcc} = 20000$	$L_{Ni : Ni, Nb} = 67712$ $L_{Ni,Nb: Ti} = -64320 + 17.652 * T$ $L_{Ni,Nb: Ni} = -2780$
	Ni:Ti	$G_{Ni:Ti}^{Ni3Ti} - 3 * G_{Ni}^{Fcc} - G_{Ti}^{Hcp} = -160000 + 208 * T$	
	Ni:Nb	$G_{Ni:Nb}^{Ni3Nb} - 3 * G_{Ni}^{Fcc} - G_{Nb}^{Bcc} = -113184 + 5.866 * T$	
	Nb:Nb	$G_{Nb:Nb}^{Nb3Nb} - 3 * G_{Nb}^{Bcc} - G_{Nb}^{Bcc} = 20000$	
	Nb:Ni	$G_{Nb:Ni}^{Nb3Ni} - 3 * G_{Nb}^{Bcc} - G_{Ni}^{Fcc} = 163184 - 5.866 * T$	
	Nb:Ti	$G_{Nb:Ti}^{Nb3Ti} - 3 * G_{Nb}^{Bcc} - G_{Ti}^{Hcp} = 57520$	

The two eutectic reactions and congruent melting temperature pertaining to the delta phase exhibit good consistency with the experimental results from literature, which is summarized in Table 4-13. Moreover, the calculated results of the congruent melting temperature of the δ phase are very close to the experimental data recently measured using DTA by Chen *et al.* [124]. Figure 4-10 shows the reassessed calculation of the Ni-Nb phase diagram with the available equilibria data from the literature [123-126]. It could be seen that the current results are generally consistent with the data from the literature.

Table 4-13 Comparison between this work and different experimental results from the literature of the δ phase invariant equilibria in the Ni-Nb system

Reaction	Type	Compositions of Nb (at. %)	Temperature (K)	Reference
Liquid \rightarrow Delta	Congruent	0.25	1680.7	This work
		0.25	1684	[126]
		0.25	1677	[125]
Liquid \rightarrow Ni_FCC + Delta	Eutectic	0.10; 0.14; 0.25	1581.5	This work
		0.12; 0.15; 0.24	1559.5	[126]
		0.12; 0.15; 0.24	1558	[125]
Liquid \rightarrow Delta + Ni ₆ Nb ₇	Eutectic	0.27; 0.43; 0.53	1454.5	This work
		0.28; 0.41; 0.5	1449	[126]
		0.27; 0.42; 0.5	1453	[125]
		0.275; 0.41; 0.5	1448	[124]

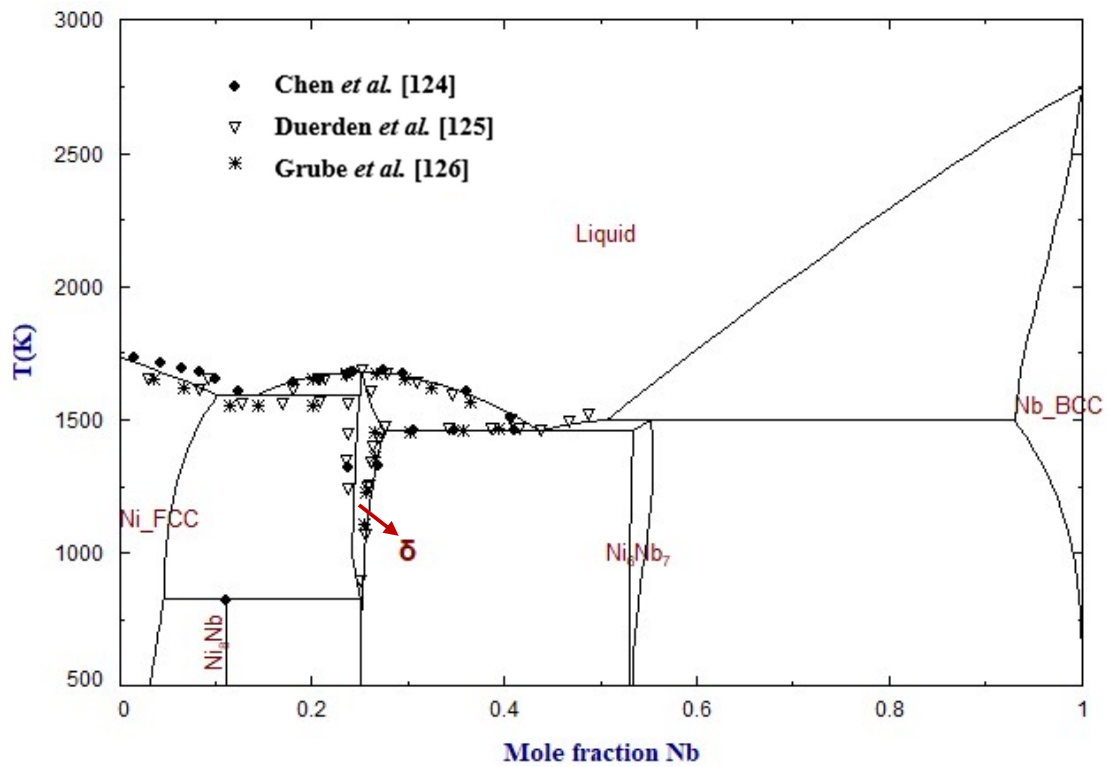


Figure 4-10 Calculated Ni-Nb phase diagram using the optimized parameter of δ phase combined with the FTlite database. Phase boundaries of δ are compared with the relevant data from the literature.

Chapter 5 Thermodynamic Calculation Results of the IN718 Alloy

In this chapter, thermodynamic calculation results of the IN718 alloy are shown using the database customized in the current work. The customized database built in this work reveals a better description of IN718 when compared with other databases from FactSage and Thermo-Calc [76,104]. It was necessary to compare them to improve the accuracy of the IN718 thermodynamic model. Moreover, some experiments were employed to verify the accuracy of the current database. Differential scanning calorimetry (DSC) tests were used to obtain the phase transition temperature. Scanning electron microscopy (SEM) was adopted along with the image processing technique to obtain phase fraction data. This validates the model from both temperature and phase fraction perspectives.

5.1 Equilibrium Calculation

In this section, the equilibrium calculation results of IN718 are discussed. The IN718 alloy has a metastable γ'' phase, which has the same chemical composition as the delta phase. Thus, when performing calculations, the two phases must be evaluated separately. The equilibrium calculation will only consider the delta phase and suppresses the γ'' phase in the system because γ'' is a metastable phase. Nevertheless, information related to the formation of γ'' phase is obtained through non-equilibrium calculations. In order to explain the improvement of the current database, different results were obtained using FactSage, Thermo-Calc and the customized database for comparison purposes. Figures 5-1 and 5-2 display the calculated equilibrium weight percentage of different phases in IN718 using the FactSage [76] and Thermo-Calc [104] databases. It could be seen that both of these results are different and not accurate. In Figure 5-1, the solvus temperature of the γ' phase is about 800 K, which is far from the experimental value that is about 1173 K [34], and the amount of this phase is as high as 55 wt. % below 800 K, which is unrealistic. Similarly, the descriptions of the Laves and δ phases

are not accurate enough as well. The same problem occurs when using Thermo-Calc. This time the Laves phase is not well described by Thermo-Calc, showing almost 25 wt. % at low temperature. In addition, the descriptions of the other phases also deviate from the practical observations from the literature [34,121,127].

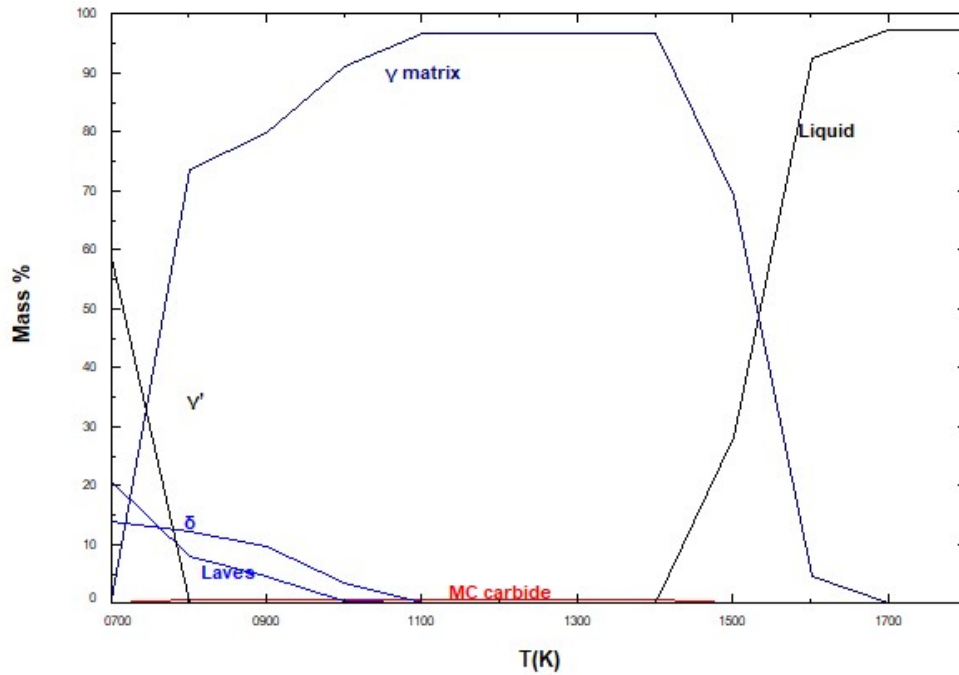


Figure 5-1 Equilibrium calculation of the mass percentage of phases as a function of temperature for the IN718 alloy using the FactSage database [76]

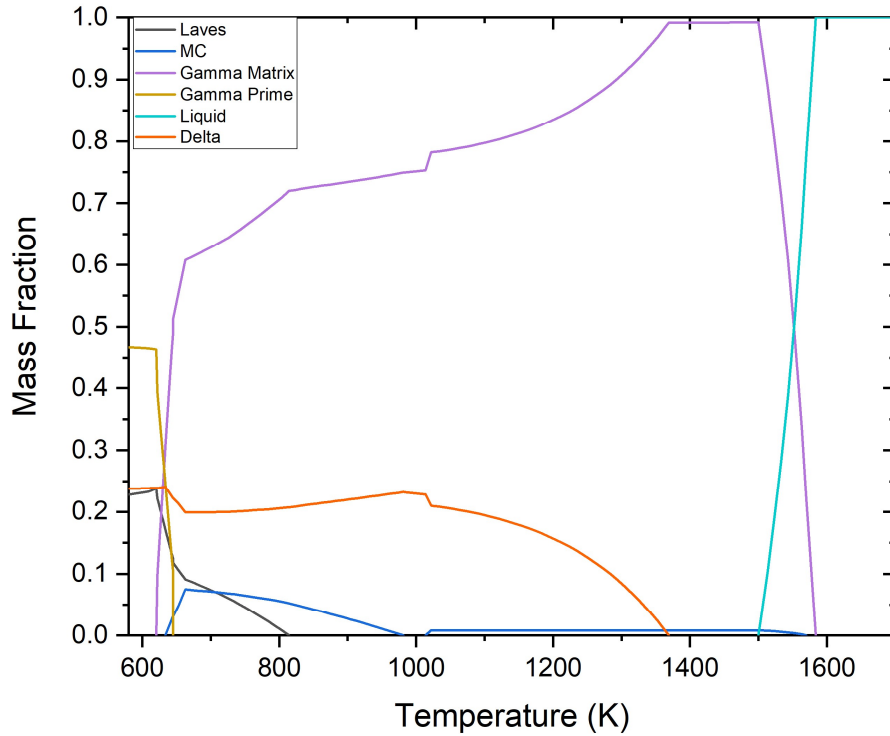


Figure 5-2 Equilibrium calculation of the mass fraction of phases as a function of temperature for the IN718 alloy using Thermo-Calc database [104]

Figures 5-3 and 5-4 show this work's calculated results of mass percentage as a function of temperature under the equilibrium condition compared with the other available calculations results from the literature [128,129]. It should be noted that since the liquid and γ matrix are substitutional random solutions, they were not re-optimized, and the descriptions of these phases are selected from the FTlite database [76]. Since similar experimental diagram is not available in the literature, the current calculations are only compared with previous calculations from the literature [128,129]. It could be seen that the overall trends of the phase change are consistent. It is important to note that the Laves phase was missing in the calculations results from the literature [128,129], while it is included in the current assessment. The solvus temperature of Laves phase in this work is about 1288.7 K, which is within the experimental solvus temperature range (1263-1423 K) reported by Ferreri *et al.* [34] and close to 1283 K

measured by Kwon *et al.* [130]. A detailed comparison of the solvus temperatures of the various IN718 phases with the current experiments will be presented in the section 5.3.

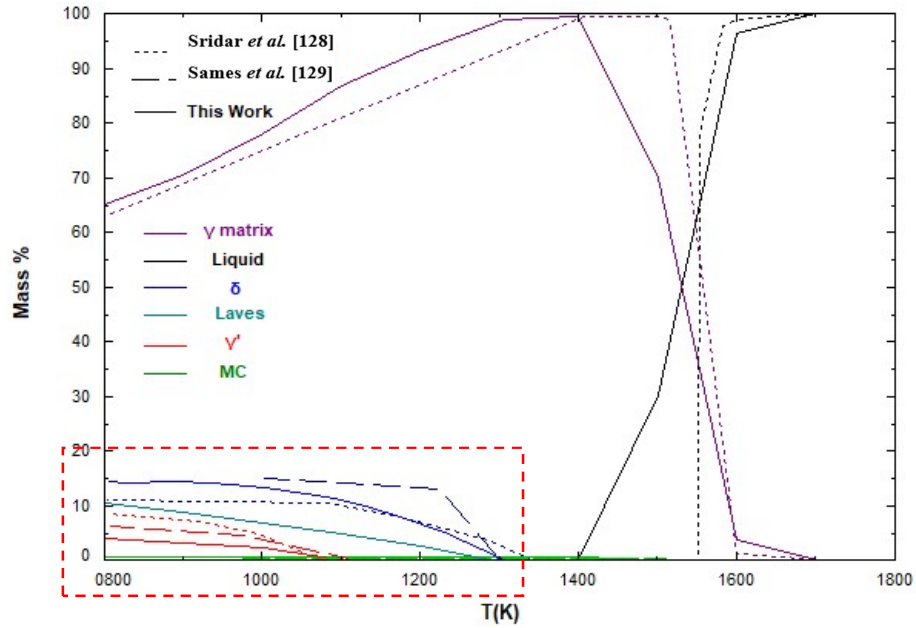


Figure 5-3 Equilibrium calculation of the mass percentage of phases as a function of temperature for the IN718 alloy using the current customized database combined with the

FTlite database

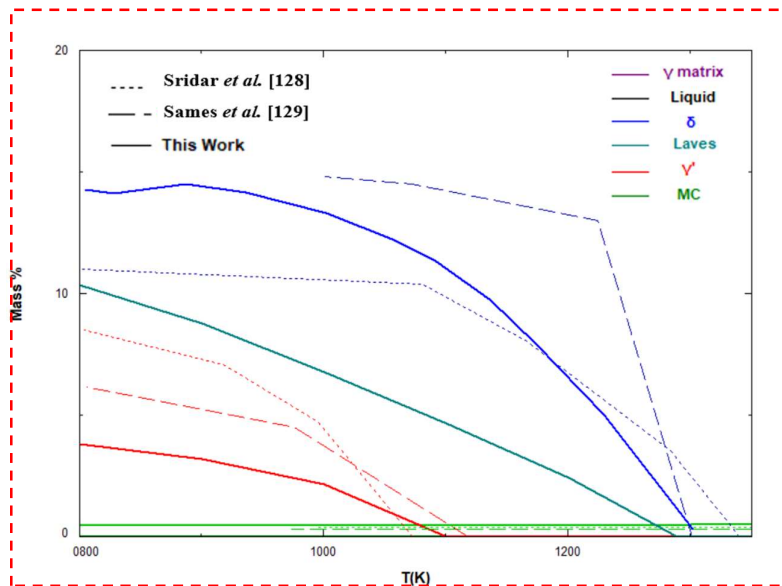


Figure 5-4 Enlarged area of Figure 5-3

5.2 Non-Equilibrium calculation

In this section, the non-equilibrium calculation results of IN718 are discussed. As mentioned earlier, the equilibrium calculation does not allow the δ and the γ'' phases to occur at the same time since these two phases have the similar composition. However, when conducting a non-equilibrium calculation, the FactSage allows to force the γ'' phase be set as metastable phase. The different calculations were performed for non-equilibrium conditions using FactSage with the customized database optimized in this work and compared with Thermo-Calc and FactSage using FTlite database. Figures 5-5 and 5-6 show the calculated non-equilibrium mass percentage of different phases in IN718 obtained using FTlite database [76] and the database of Thermo-Calc [104]. It could be seen that these two calculated results are also not correct. In the result obtained from the FTlite database, the solvus temperature of the γ' , γ'' and Laves phases are all about 1050 K, which is far from the experimental value from the literature [34,127] that is about 1200 K. Especially, the phase fraction of γ' dramatically increases when the temperature drops down to 800 K to reach around 55 %. Some issues are also observed in the Thermo-Calc's non-equilibrium calculation of IN718. Although the trend of the γ' phase is flatter than the modelling results obtained using FTlite database, the Laves phase is not well described as its amount unrealistically increases to reach around 30 % below 650 K.

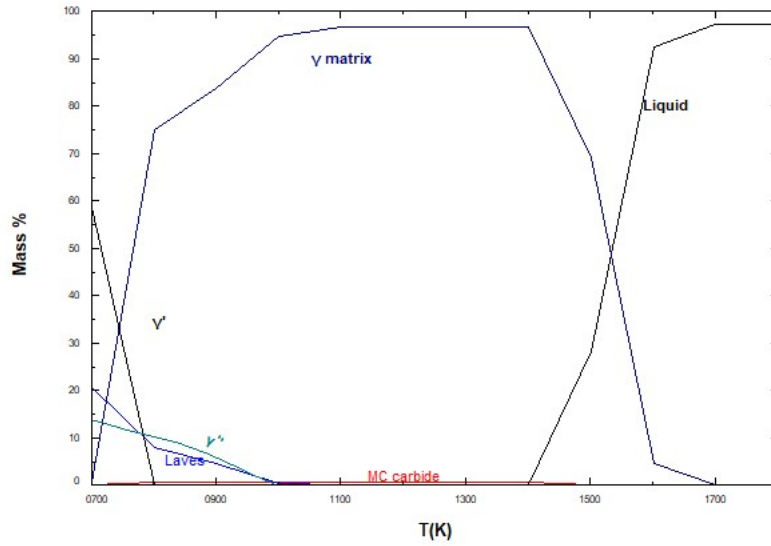


Figure 5-5 Non-equilibrium calculation of the mass percentage as a function of temperature for IN718 by FTlite database [76] without the current database

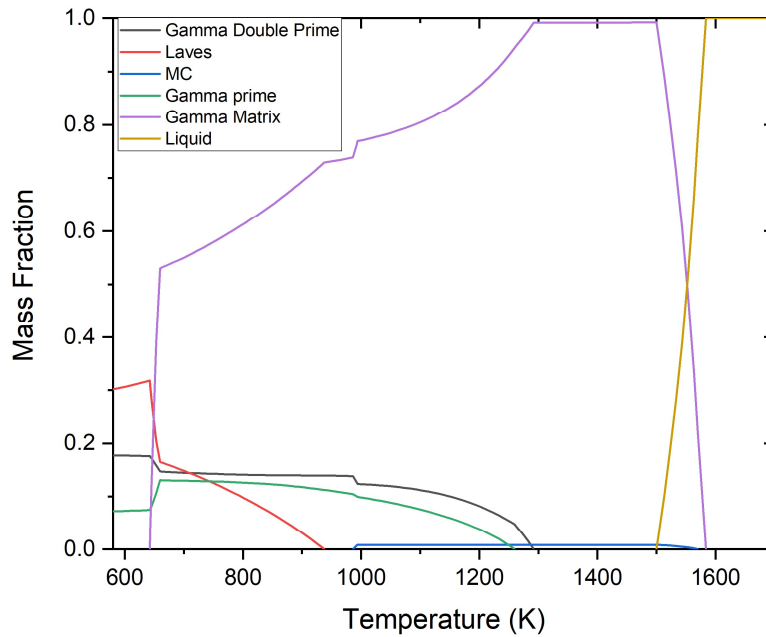


Figure 5-6 Non-equilibrium calculation of the mass fraction of phases as a function of temperature for IN718 alloy using Thermo-Calc database [104]

Figures 5-7 and 5-8 show the calculated non-equilibrium mass percentage of phases as a function of temperature using that current database. It needs to be noted that there are not any

non-equilibrium calculations mentioned in the literature which help estimate the γ'' phase. Based on the previous discussion, the customized database made in this work fix this issue and predicts the γ'' phase in the IN718 alloy. The solvus temperature of the γ'' phase in this work is about 1180 K, which is close to the experimental result 1183 K – 1193 K mentioned by Ferreri *et al.* [34] for additively manufactured IN718. A detailed discussion of solvus temperatures of these phases will be clarified further in the following section.

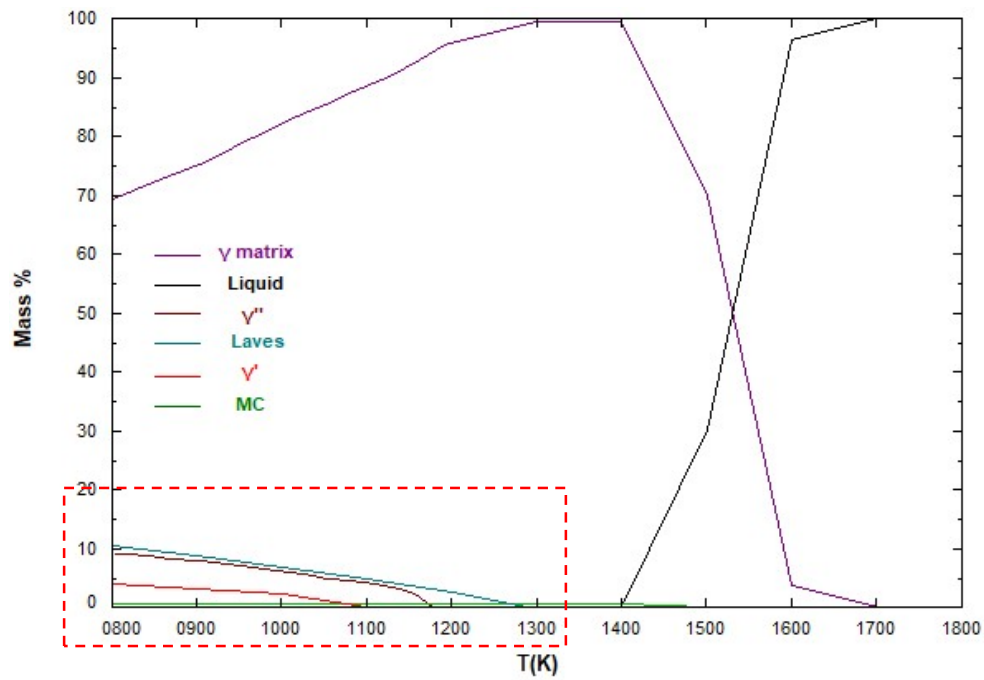


Figure 5-7 Non-equilibrium calculation of the mass percentage of phases as a function of temperature for IN718 alloy using the current customized database combined with FTLite

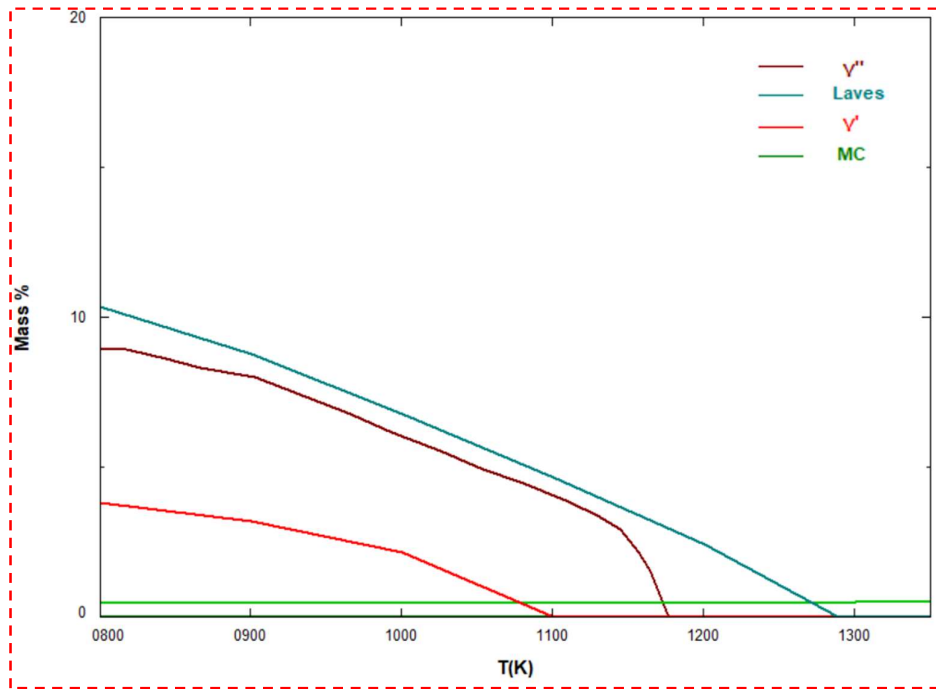


Figure 5-8 partially enlarged area of Figure 5-7

5.3 Experimental Verification

The current thermodynamic calculations have been verified experimentally in this work. Differential scanning calorimetry (DSC) tests were used to obtain the phase transition temperature of different phases. Scanning electron microscopy (SEM) was used along with an image processing technique to obtain phase fraction data. This validates the model from both temperature and phase fraction perspectives.

5.3.1 Sample Preparation

Figure 5-9 shows SEM micrographs of the original IN718 powder used in this work. The gas-atomized IN718 powder, which is supplied by EOS-GmbH (Krailing, Germany) [131], was used to fabricate test samples by the LPBF process. It can be seen that the IN718 powder particles are mainly spherical, and some particles are surrounded by smaller satellite particles. Meanwhile, the microstructure on the surface of the particles could be attributed to the rapid solidification during the gas atomization process [132]. EDS analysis is employed in

this work to obtain the chemical composition of the IN718 powder as shown in Table 5-1, "Supplier data sheet" in the table is the chemical composition of powder provided by the supplier [131], and "EDS all area" is the result of the EDS test for the entire area of Figure 5-9 (a). By calculating the average of EDS results tested by this work, it can be concluded that the average results for each element are all in the standard range of IN718 provided from the literature [133]. Also, trace elements such as carbon are classified as "balance" together with Fe in the table because the content of these elements is small, and carbon tape is used in SEM, which can bring certain errors to the measurement of carbon.

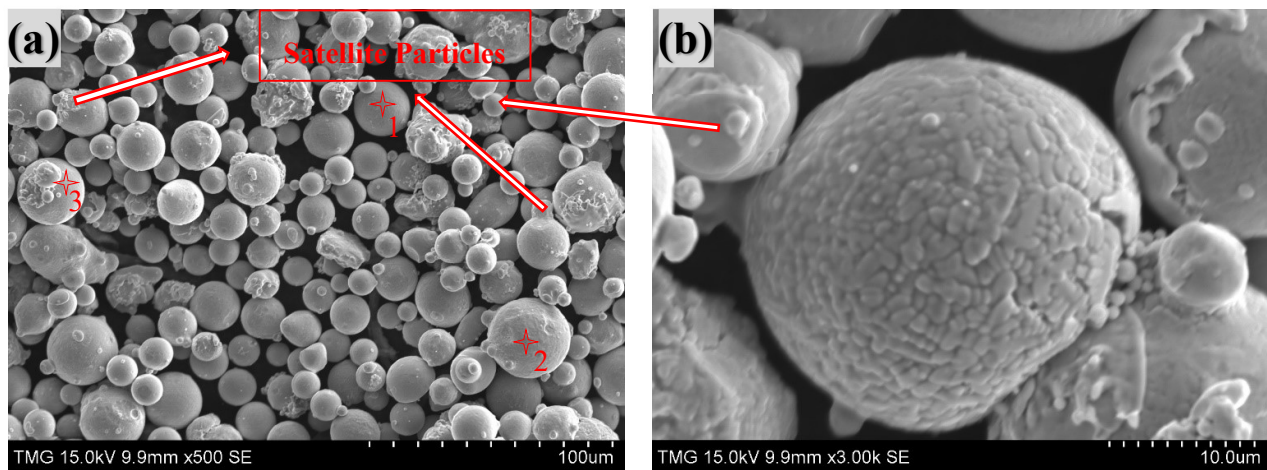


Figure 5-9 (a) Scanning electron microscopy (SEM) micrograph of original Inconel 718 powder (b) single particle of original Inconel 718 powder

Table 5-1 EDS chemical composition of the IN718 powder.

Chemical composition (wt.%)							Reference
Ni	Cr	Nb	Mo	Ti	Al	Fe + Traces	
52.7	18.50	4.8	2.9	1.1	0.45	Bal.	Supplier data sheet [131]
51.31	18.99	4.55	3.42	0.52	0.53	Bal.	EDS Spot.1*
50.22	18.25	6.12	3.33	1.07	0.31	Bal.	EDS Spot.2*
50.25	17.66	7.06	3.62	1.29	0.49	Bal.	EDS Spot.3*
49.19	19.04	4.92	2.70	1.08	0.58	Bal.	EDS all area
50.24	18.49	5.51	3.27	0.99	0.48	Bal.	Average of EDS results
50-55	17-21	4.75-5.55	2.8-3.3	0.65-1.15	0.2-0.8	Bal.	Typical composition [133]

* Spot number corresponds to Figure 5-9

For the 3D-printing machine, the EOS M280 (EOS, Krailling, Germany) was used to fabricate the IN718 test samples. The printing parameters were the EOS Original Parameter Set for LPBF IN718 (285 W laser with 100 μm beam diameter, 1000 mm/s scanning speed, 110 μm hatching space with 67 hatching angle, and 40 μm layer thickness). To reduce thermal stresses, the building platform was pre-heated. Meanwhile, argon was used to limit oxidation during the printing process. Figure 5-8 shows the geometry and dimensions of the as-printed IN718 samples used in this work. The samples were heat treated to homogenize and control the precipitation of the primary phases in IN718 alloy. Then, high-resolution SEM is used to estimate the amounts of the different phases and to compare them with the current calculations.

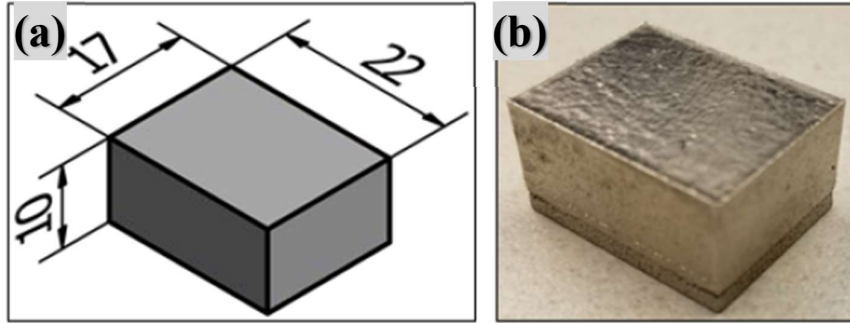


Figure 5-10 (a) Dimensions of the printed IN718 sample (b) appearance of the printed IN718 sample

5.3.2 Phase Transformation Analysis

In order to measure phase transformation temperatures of the different phases in the IN718 alloy, differential scanning calorimetry (DSC) was performed. This experiment consists of two parts. The first part is a DSC test on the original IN718 powder that is used for printing. Then, the second part is the DSC test of the powder obtained by grinding an as-printed sample. The powder material generally results in more accurate and smoother data compared with the bulk sample. IN718 contains a variety of complex phases, and some of the solid-solid phase transformations might be hard to detect. Therefore, the DSC tests for ground powder were performed to increase the accuracy and detect the solid-solid phase transformations as much as possible. There are three batches of tests for ground powder. The first and second tests were conducted on the ground powder from the same as-printed sample. The third one was performed on the same sample used for the second test under the same heating and cooling conditions. In this way, it helps evaluate and detect the phase transformations as much as possible. These tests were performed on a SETARAM differential scanning calorimeter with a 10 K/min rate, and the sample's weight was about 50 milligrams.

As shown in Figure 5-11, the DSC curve of the original IN718 powder is smooth in the whole range for both heating and cooling cycles. Other than liquid-solid transition, no transitions could be observed.

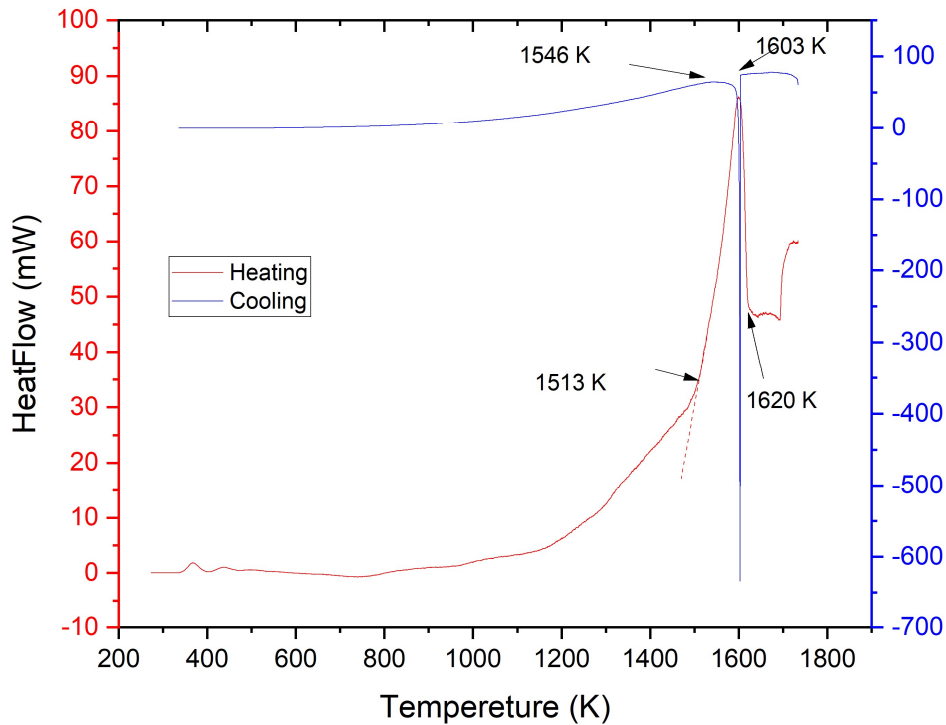


Figure 5-11 DSC spectra and reaction temperatures of the IN718 powder.

Concerning the printed sample, Figures 5-12 and 5-13 show the three heating and cooling experiments. When looking at Figure 5-12, the cooling experiments, it could be concluded that the initial γ phase starts to nucleate and grow in the liquid phase at about 1620 K, which will release large amounts of heat, resulting in a distinct peak in the curve ending at about 1513 K. And this liquid-solid change is confirmed in the heating process (Figure 5-13) as well. For all three tests, this liquid-solid reaction temperature range is repeatable and close to each other. Also, Wang *et al.* [134] reported this reaction to happen between 1625 K to 1651 K in the heating process, supporting the current DSC results.

In Figure 5-13, when the temperature is below the γ nucleation, additional endothermic peaks are observed in the vicinity of 1543 K and 1460 K. These temperatures can be considered as solvus temperature of the carbide and Laves phases. Solid-solid phase transformations can also be observed as the low-intensity peaks at 1548 K and 1445 K in the corresponding cooling curve shown in Figure 5-13.

It is worth noticing that the different peaks correspond to changes in metallurgical conditions during each cooling cycle. Some small peaks were also observed in all three heating curves at about 1286 K, especially in the first and second heating cycles. This peak was not observed in the cooling curves. This solid-solid transformation can be inferred as the metastable γ'' phase transformation, since the γ'' phase dissolves at high temperature. Moreover, according to the latest XRD analysis reported by Kumar *et al.* [135], the heat treated IN718 alloy contains this γ'' phase. Thus, this phase should be detected in the heating process and will not be observed in the subsequent cooling process in the DSC test.

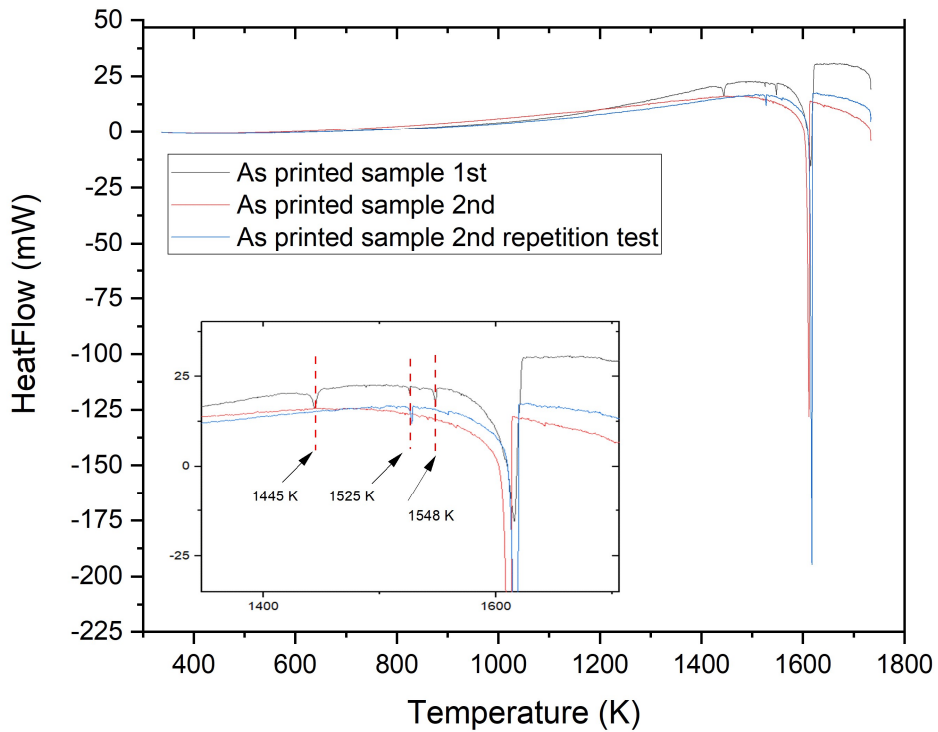


Figure 5-12 DSC cooling curve and phase transformation temperatures of IN718.

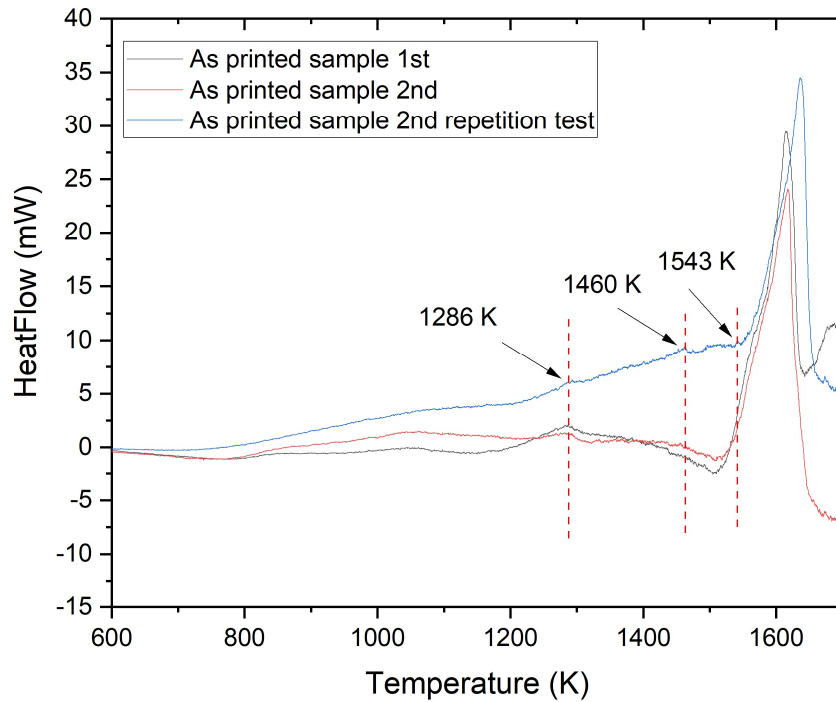


Figure 5-13 DSC heating curve and reaction temperatures of IN718.

In order to verify the accuracy of the calculated phase transformation temperatures, available experimental and calculation results from the literature [34,121,128,129] have been compared with the current work. Tables 5-2 and 5-3 list the equilibrium and non-equilibrium calculation results done in this work using different databases compared with other calculation results from the literature [121,128], and current DSC testing results along with other experimental results from the literature [34,127]. It could be concluded that the customized database fixed the problem of the missing γ'' and the Laves phase in the calculation results obtained using the commercial databases. Meanwhile, this customized database significantly improves the accuracy of modelling the γ' phase under both equilibrium and non-equilibrium conditions, where the results are consistent with the experimental results from the literature [34,127]. It is necessary to clarify that the solvus temperature for γ' and δ phase were not captured by the current DSC experiments. And the solvus temperature of the Laves phase shows more than 100 K gap between the previous experimental result from Ferreri *et al.* [34] and the current

measurement. In order to resolve this inconsistency, further research on experimental determination of phase transformation of 3D printed IN718 is recommended.

Table 5-2 Precipitation temperature for main phases in the 3D printed IN718 alloy under equilibrium condition.

Precipitation temperature for phases (K)					Reference
γ	γ'	δ	Laves	MC	
1573-1636	-	-	1400-1455	1523-1543	Current DSC results
1695	1103	1298	1288	1502	Calculation this work
1700	790-798	1100	1050	1480	Calculation by the FTlite database
1591	643	1371	813	1563	Calculation by the Thermo-Calc's database
1600-1620	1112	1295	-	1531	Calculations [114]
1630-1635	1163	1278	-	1473	Calculations [121]
1605-1650	1173-1243	1278	1283	1313-1473	Experiments [34,127]

Table 5-3 Precipitation temperature for main phases in the 3D printed IN718 alloy under non-equilibrium condition.

Precipitation temperature for phases (K)					Reference
γ	γ'	γ''	Laves	MC	
1573-1636	-	1273-1373	1400-1455	1523-1543	Current DSC results
1699	1100	1184	1290	1505	Calculation this work
1700	790-798	998	1050	1480	Calculation by the FTlite database
1581	1258	1291	923	1567	Calculation by the Thermo-Calc's database
1600-1620	1112	-	-	1531	Calculations [114]
1630-1635	1163	-	-	1473	Calculations [121]
1605-1650	1173-1243	1183-1203	1283	1313-1473	Experiments [34,127]

5.3.3 Microstructural and Phase Analysis

To verify the phase contents of the 3D-printed IN718 alloy, scanning electron microscopy was used to examine the morphology of the precipitates and to identify their composition. Image processing software (ImageJ) was used to obtain the phase amounts by adjusting the grayscale and contrast of the image to highlight some specific precipitated phases. It should be noted that since MC and the Laves phase could be similar in morphology, it is necessary to perform the EDS analysis for some specific regions to identify these two phases. By combining EDS analysis with image processing, more accurate information about phase amounts is obtained.

The samples used for SEM have experienced the same heat treatment: homogenization at 1353 K, following solution at 1253 K and double aging at 993 and 893 K, respectively. This heat treatment follows the current general industrial standard [7,13] in order to achieve good mechanical properties of this alloy. To characterize the γ' and γ'' phases, a relatively high magnification to see sub-micron features is required. Also, an etching process was carried out in order to observe these phases. The image in Figure 5-14 shows the morphology and the needle-like δ phase. It is difficult to distinguish γ' and γ'' phases from the γ matrix by EBSD (Electron backscatter diffraction) due to their similar crystal structure. Also, these three phases are coherent due to similar lattice parameters. Therefore, the γ matrix, γ' and γ'' phases are grouped into one category during image processing. Through SEM image processing and EDS analysis, the composition and morphology of each phase could be obtained. The needle-like δ phase is mainly concentrated in the grain boundary as can be seen in Figure 5-14. Figure 5-15 shows the original SEM image and the sequence of analysis using ImageJ for each step of image processing. Firstly, a special filter was applied to the image to obtain features within a range of a few pixels. By doing so, the precipitated phase can be highlighted to a certain extent. Meanwhile, it could be used to denoise images by reducing the low-frequency artifacts such as

uneven illumination. Then, specific thresholds were assigned to obtain an improved contrast. This step allows the image to be rendered in black and white, further enhancing the discernibility of the precipitated phase. Finally, the different phases are filtered out by setting the size and the circularity of the particle.

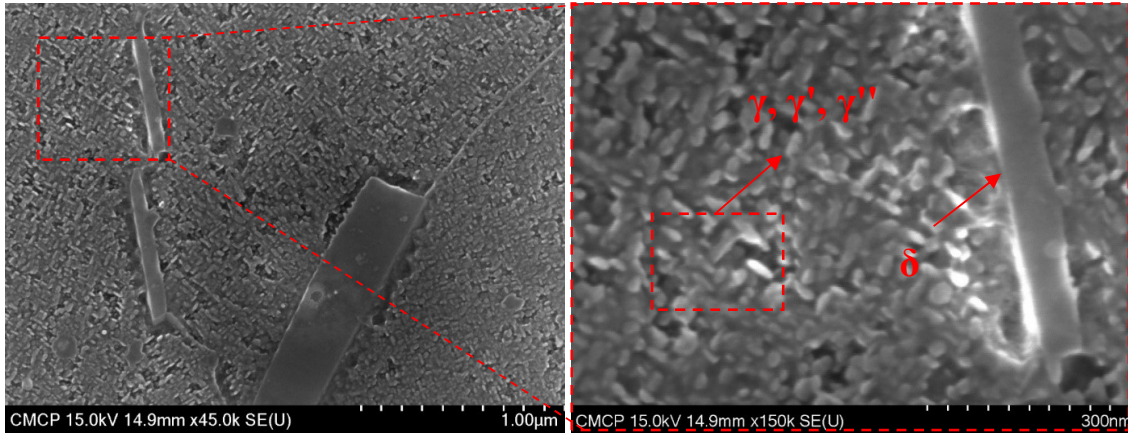


Figure 5-14 High magnification SEM images showing the γ , γ' , γ'' and δ phases

Table 5-3 lists the EDS spot analysis results which correspond to the spot number in Figure 5-16. In this table, spots 9 and 10 exhibit relatively high amounts of Ni and Nb, which are necessary for the delta phase precipitation. MC is determined mainly by the carbon content. Spots 1, 2 and 3 reveal higher content of carbon compared with other regions. Moreover, the content of Nb in these spots are comparatively high, indicating the presence of the NbC. The Laves phase is also difficult to identify due to its morphology. However, it can be indirectly identified by the content of Fe and Cr (trace amount) and the atomic ratio between Ni and Nb which should be close to 2:1 following the chemical composition of the Laves phase (Ni, Cr, Fe)₂(Nb, Ti) reported in the literature [34,51,69]. Therefore, spots 4-8 and 13 can be identified as the Laves phase. These results are close to the chemical composition of the Laves phase. It is important to note that when using EDS to measure small or thin precipitates, measurement errors occur due to the larger volume of interaction than the size of the precipitates. Therefore,

to identify phases, it is necessary to consider a combination of morphology, precipitation position, and composition obtained by SEM and EDS analysis.

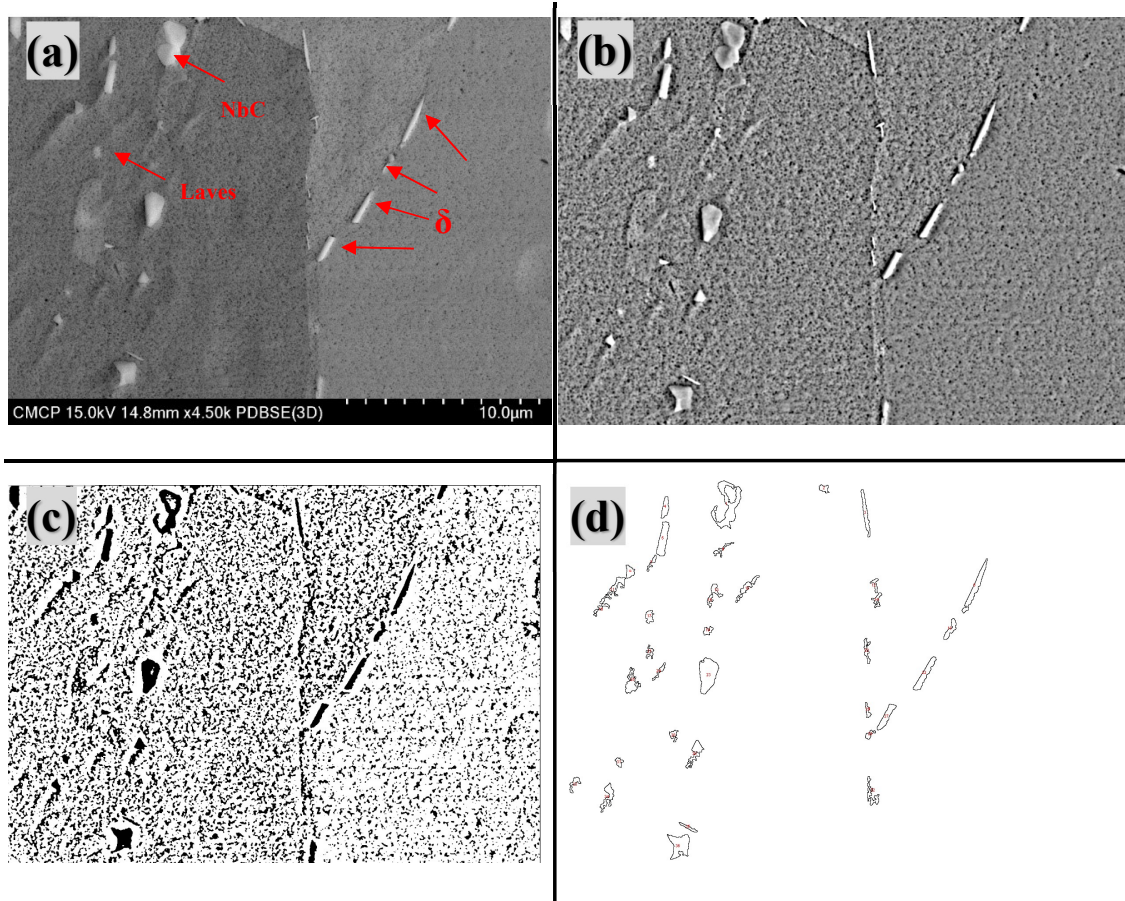


Figure 5-15 (a) Original high magnification SEM image; (b) image after the filter process; (c) image after setting the contrast thresholds; (d) final image for filtering out the phases.

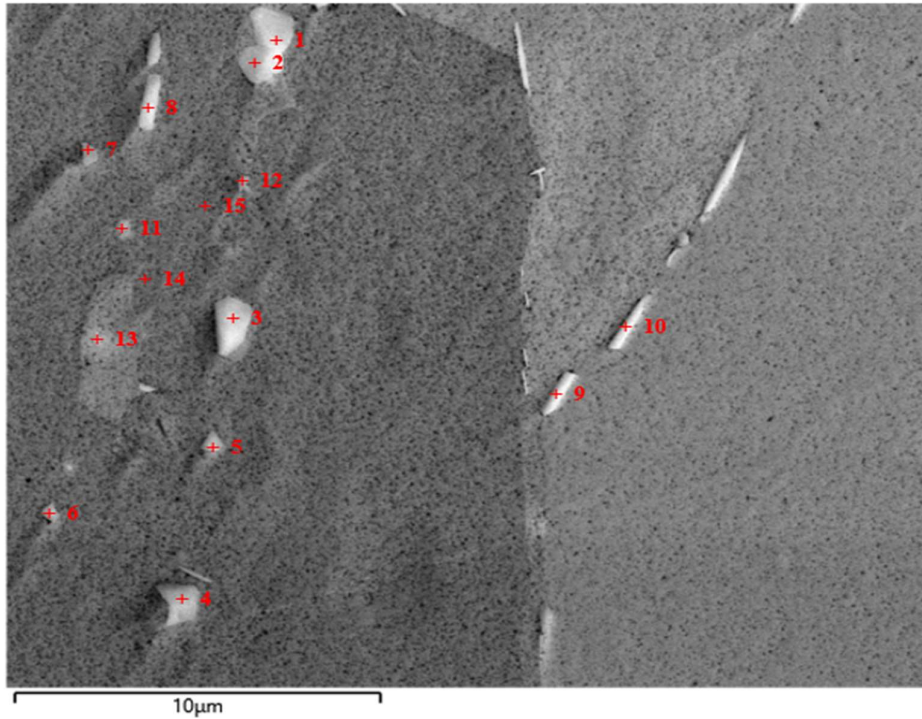


Figure 5-16 High magnification SEM images with EDS spot analysis

Table 5-3 EDS spot analysis results (The spectrum number correspond to the spot number in Figure 5-16)

Spot No.	C	Ti	Cr	Fe	Ni	Nb	Mo	Total (at. %)
1	51.77	7.11	3.75	2.94	6.95	27.45	0.04	100.00
2	52.44	8.06	1.89	1.43	3.27	32.90	0	100.00
3	51.07	5.90	4.79	3.65	8.71	25.69	0.19	100.00
4	42.65	3.96	9.29	7.42	19.11	17.10	0.48	100.00
5	44.40	4.22	8.69	6.82	16.80	18.67	0.40	100.00
6	39.56	3.85	10.47	8.49	21.84	15.14	0.65	100.00
7	29.46	1.68	14.43	12.22	34.31	6.60	1.30	100.00
8	37.11	2.91	11.40	9.36	25.43	13.04	0.76	100.00
9	17.14	1.31	14.93	12.74	46.93	5.69	1.25	100.00
10	14.47	1.10	17.94	15.16	46.20	3.65	1.48	100.00
11	15.77	1.96	17.29	14.66	41.69	7.26	1.38	100.00
12	16.07	1.16	18.19	15.40	44.56	3.06	1.55	100.00
13	23.27	5.32	12.07	9.86	27.73	21.00	0.76	100.00
14	13.21	1.03	18.88	16.36	46.05	2.80	1.67	100.00
15	15.03	0.97	18.55	15.88	45.33	2.69	1.55	100.00

Additional four SEM images (Figure 5-17 a-d) are analysed to increase the reliability of phase fraction measurements. These images are taken from different locations on the sample surface and processed the same as mentioned above for Figure 5-14. The processing steps are shown in Figure 5-17 e-l. Similarly, after image processing, EDS results for each image were considered together with the microstructural features to identify the phases. The results are summarized in Table 5-4.

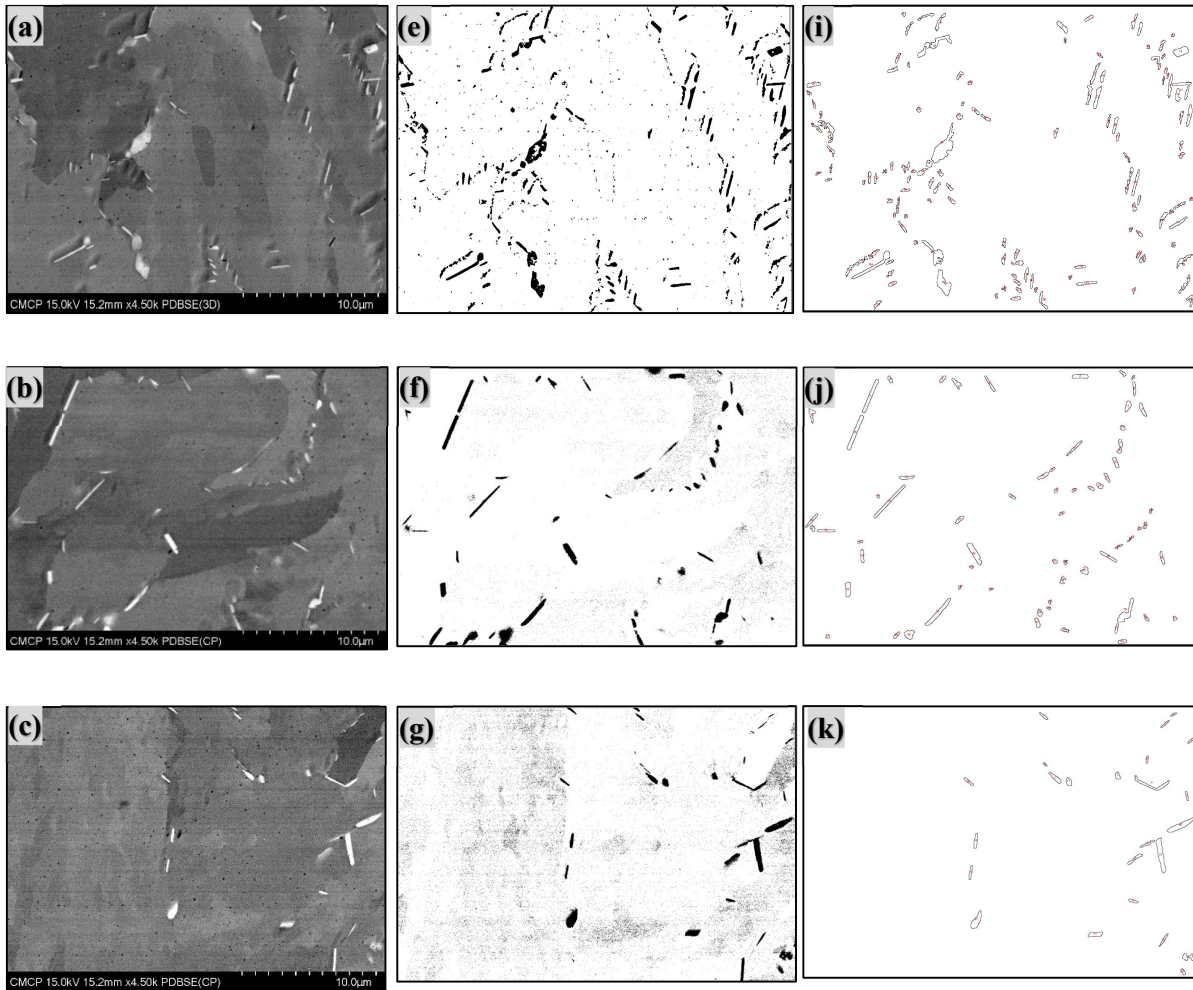




Figure 5-17 (a-d) Original high magnification SEM micrographs; (e-h) images after setting the contrast thresholds; (i-l) final image after filtering out the phases.

Table 5-4 Phase content in the 3D-printed IN718 alloy.

	$\gamma + \gamma' + \gamma''$	δ	MC	Laves
Image No.1 (vol.%)	88.42	5.56	2.70	3.32
Image No.2 (vol.%)	86.54	9.34	0.65	3.47
Image No.3 (vol.%)	89.35	8.11	0.45	2.09
Image No.4 (vol.%)	95.05	3.83	0.48	0.64
Image No.5 (vol.%)	96.62	2.12	0.59	0.67
Average No.1-5 (vol.%)	91.21	5.79	0.97	2.03
Ferreri <i>et al.</i> [34] (vol.%)	-	5.9	1.9	-
Average No.1-5 (mass %)	90.98	6.32	0.89	1.81
Modelling results (mass %)	77.5	14	0.5	8

Table 5-4 contains the volume percentage of phases obtained in this work and the converted mass percentage based on the theoretical density of each phase. It is necessary to clarify that the calculation of theoretical density is done following the equation $D = (n \cdot A) / (V \cdot N)$ [136], where D refers to the density, n is the number of atoms per unit cell, A is the

atomic weight (g/mol), V is the volume of the unit cell and N is Avogadro's number. The calculated density of MC carbides is about 7.6 g/cm^3 , for the Laves phase, it is about 7.06 g/cm^3 and for the δ phase, it is about 8.96 g/cm^3 . Since the γ matrix, γ' and γ'' are hard to distinguish from one another when performing SEM image analysis, they are being treated as one group. The theoretical density for this group is estimated to be equal to the density of the overall IN718 alloy, which is 8.19 g/cm^3 [134]. It could be inferred that the average volume percentage of MC in this work is about 1% which is relatively close to the experimental results of 1.9 % from Ferreri et al. [34] via neutron diffraction. The average volume percentage of the δ phase is consistent with Ferreri et al. [34] as well. While comparing the converted mass percentage of the δ and Laves phases with this work's modelling results, the thermodynamic modelling results show about 5-8 wt. % overestimation. Modelling indicates that there are about 14 wt. % of the δ phase and 8 wt.% of the Laves phase at 893 K, which is the final aging temperature used in this work. These numbers are significantly higher than the experimental values. Theoretically, from this temperature to room temperature, only a tiny change should occur in the sample. So ideally, the equilibrium calculated phase content of this alloy at this final HT temperature should be close to the experimental results. However, this indicates that further research is still needed to improve both the thermodynamic modelling and the experimental results.

In summary, in this work, DSC tests were performed to verify the phase transformation temperatures calculated by the customized database. It could be said that the customized database resolved the issue of the missing Laves phase and improved the accuracy of describing the solvus temperature of the main phases in the 3D printed IN718 alloy. Meanwhile, from the phase percentage perspective, although SEM and EDS analysis combined with image processing techniques, the phase percentage information of the δ , MC and Laves phases are estimated, which provides a starting point for obtaining the phase percentage data for the 3D

printed IN718 alloy. This type of analysis required a considerable number of micrographs from various locations in the sample. At the same time, performing this type of analysis for more images could technically increase the accuracy of the phase fraction information. More detailed experimental investigations need to be carried out based on which the thermodynamic models of the different phases in the 3D printed IN718 alloy can be improved in the future. Moreover, the SEM and image analysis performed in this work provide only the area fraction of phases which can have different sizes in the other direction. This results in an inevitable error in estimating phase volume fraction using area fraction. Therefore, analysis of volume fraction of the phases in the 3D printed IN718 is highly recommended in the future.

Chapter 6 Conclusions, Contributions and Recommendations for Future Work

In this chapter, the main findings of this work are summarized. Important research contributions of the current study are discussed. Finally, based on this work and the literature, suggestions for future work are provided.

6.1 Conclusion

The current research work presents a thermodynamic assessment and customized database for the main phases in the 3D-printed IN718 superalloy. The reliability of the database was verified by experiments. Based on this, the following points can be concluded:

- A comprehensive literature review and re-optimization of the pertinent binary systems are performed, where the primary phases (γ' , γ'' , δ and Laves) in the IN718 alloy exist. Thermodynamic parameters of these phases were evaluated. The phase regions and the associated invariant reactions are verified by comparison with the experimental and calculated phase diagrams from the literature.
- Thermodynamic descriptions of these phases in the multi-component IN718 alloy are obtained by combining the various binary contributions in a sublattice model. Thus, a customized database is established for describing the main phases in the IN718 alloy.
- To illustrate the improvement in the current model's accuracy, thermodynamic calculations of the printed IN718 alloy are compared with those obtained using two commercial databases. Although the current database has some overestimation for the weight percentage of the δ and Laves phases, the modelling results for the solvus temperature of the γ' , γ'' and Laves phases are

improved compared with the commercial databases and the calculation results in this work are in general closer to the experimental results.

- DSC experiments were employed to verify the formation and transformation temperatures of different phases (γ' , γ'' , δ , and Laves). These results demonstrate that the calculated temperatures using the current database are more consistent with the experimental temperatures for most phases. However, there is a discrepancy between the experimental results and the calculation results for the Lave phase. This requires further experiments to verify the phase transformation temperature of this phase, as there is too little experimental data existing in the literature.
- Scanning electron microscopy was used to study the morphology and amounts of the precipitates. Meanwhile, EDS was performed to identify the various precipitates.
- The estimated phase percentages are obtained by image processing of the SEM micrographs. These results show that the estimated Carbide amount is in good agreement with the values reported in the literature and is consistent with the current thermodynamic calculations. However, the Laves and δ phases need additional experiments to improve the thermodynamic model.

6.2 Contributions

In recent years, the utilization of 3D printing to manufacture IN718 components has been gaining attention. In particular, LPBF printing technology has demonstrated its potential in producing IN718 3D printed parts with acceptable mechanical properties. Therefore, it is necessary to develop a unique thermodynamic database for IN718, especially for the 3D printing condition. Although some commercial databases generally contain an accurate representation of the constituent binary systems, they are not as accurate for the more complex

high-order alloys such as IN718. This shows that further optimization of the database is imperative. Thus, this work provides the first attempt to improve the thermodynamic description of the 3D printed IN718 alloy. The current calculations have been verified experimentally in this work, using DSC and SEM. Due to the systematic approach used in this research, this database is expected to be suitable for simulating other Ni-based alloys containing similar elements but with different proportions. This will provide an important roadmap for the development of superalloys 3D printing and their heat treatments. In future work, the time effect can be included to establish a database containing the kinetics of this alloy to obtain a time-temperature-transformation (TTT) diagram, which will be very helpful for the understanding of 3D printing of the current Inconel and for the development of new Ni-based alloys suitable for additive manufacturing.

6.3 Recommendations for Future Work

Based on this work, there is still plenty of room and necessity for future research. The essence of more studies can be summarized as follows:

- The modelling method followed in this work is to directly construct Gibb's free energy description for different high-order phases. These phases have only been verified for the stability and homogeneity range in the related binary systems. Ternary and quaternary systems are not systematically examined. According to most literature, step-by-step extrapolation is widely used following the traditional thermodynamic modelling and CALPHAD method. However, this method requires a lot of time and workforce to build, optimize and build the database. It is recommended that the constituent ternary and quaternary systems be included in a future study.

- Because there are at least eight major elements involved in IN718, a lot of experimental data is still missing for the constituent ternary and quaternary systems. It is essential to establish more accurate experimental research and thermodynamic assessment for these systems.
- For thermodynamic modelling and calculation, the different databases from different providers are not compatible. Even some compatible databases are generally built with different reference states. It will save a lot of time if they all use standard modelling criteria and common file types for databases.
- For the phase fraction in IN718, because γ , γ' and γ'' have very similar crystal structures and require very high magnification SEM to observe, it is difficult to distinguish these three phases by SEM and acquire their relative amounts. In this work, EBSD with high magnification SEM was attempted to distinguish these phases, but the results were not accurate. Therefore, the establishment of an experimental method to obtain the relative amounts of these phases could be the focus of future research.
- It is recommended to develop an experimental technique to measure the volumetric percentage of the main phases in the 3D printed IN718 alloy instead of relying only on 2D SEM micrographs.

Reference

- [1] D. F. Paulonis, and J. J. Schirra: Alloy 718 at Pratt & Whitney-Historical perspective and future challenges, *Superalloys*. 2001, Vol. 718, pp. 13–23.
- [2] J. Belan: GCP and TCP phases presented in nickel-base superalloys, *Metals and Materials*, 2016, Vol. 3, No. 4, pp. 936–941.
- [3] M. Sundararaman, P. Mukhopadhyay, and S. Banerjee: Precipitation of the δ -Ni₃Nb Phase in Two Nickel Base Superalloys. *Metals and Materials*, 1988, Vol. 19, pp. 453–465.
- [4] R. Cozar, and A. Pineau: Morphology of γ' and γ'' precipitates and thermal stability of Inconel 718 type alloys, *Metals and Materials*, 1973, Vol. 4, pp. 47–59.
- [5] A. Thomas, M. El-Wahabi, J. M. Cabrera: High-temperature deformation of Inconel 718. *J. Mater. Process. Technol.*, 2006, Vol. 177, pp. 469–472.
- [6] D. Deng: Additively manufactured Inconel 718: microstructures and mechanical properties, Licentiate Thesis Degree, Linköping University, 2018.
- [7] E. Akca, and A. Gürsel: A review on superalloys and IN718 nickel-based Inconel superalloy, *Periodicals of Engineering and Natural Sciences*, 2015, Vol. 3, pp. 15–27.
- [8] P. Liu, J. Hu, S. Sun, K. Feng, Y. Zhang, and M. Cao: Microstructural evolution and phase transformation of Inconel 718 alloys fabricated by selective laser melting under different heat treatment, *Journal of Manufacturing Processes*, 2019, Vol. 39, pp. 226–232.
- [9] S. Bremen, W. Meiners, and A. Diatlov: Selective laser melting: a manufacturing technology for the future, *Laser Technik Journal*, 2012, Vol. 9, pp. 33–38.
- [10] M. Monzón, Z. Ortega, A. Martínez, and F. Ortega: Standardization in additive manufacturing: activities carried out by international organizations and projects, *The International Journal of Advanced Manufacturing Technology*, 2015, Vol. 76, pp. 1111–1121.
- [11] I. Gibson, D. Rosen, and B. Stucker: Additive manufacturing technologies: 3D printing, rapid prototyping, and direct digital manufacturing, 2nd ed., Springer-Verlag, New York, 2015.
- [12] D. Gu: Laser additive manufacturing (AM): classification, processing philosophy, and metallurgical mechanisms, in *laser additive manufacturing of high-performance materials*, Berlin, Heidelberg: Springer Berlin Heidelberg, 2015, pp. 15–71.

- [13] D. Zhang, W. Niu, X. Cao, and Z. Liu: Effect of standard heat treatment on the microstructure and mechanical properties of selective laser melting manufactured Inconel 718 superalloy, *Materials Science and Engineering*, 2015, pp. 32–40.
- [14] E. M. Fayed, D. Shahriari, M. Saadati, V. Brailovski, M. Jahazi, and M. Medraj: Influence of homogenization and solution treatments time on the microstructure and hardness of inconel 718 fabricated by laser powder bed fusion process, 2020, Vol. 13, pp. 25–35.
- [15] U. R. Kattner: The CALPHAD method and its role in material and process development, *Tecnologia em Metalurgia Materiais e Mineração*, 2016, Vol. 13, No 1, pp. 3–15.
- [16] H. L. Lukas, S. G. Fries, and B. Sundman: *Computational thermodynamics: the CALPHAD method*, Cambridge University Press, 2007, pp. 1–3.
- [17] N. J. Harrison: *Selective laser melting of nickel superalloys: solidification, microstructure and material response*, Thesis for Doctor of Philosophy Degree, University of Sheffield, 2016.
- [18] W. M. Tucho, P. Cuvillier, A. Sjolyst-Kverneland, and V. Hansen: Microstructure and hardness studies of Inconel 718 manufactured by selective laser melting before and after solution heat treatment, *Materials Science and Engineering*, 2017, Vol. 689, pp. 220–232.
- [19] X. Li, J. Shi, C. Wang, G. Cao, A. Russell, Z. Zhou, C. Li, and G. Chen: Effect of heat treatment on microstructure evolution of Inconel 718 alloy fabricated by selective laser melting, *Journal of Alloys and Compounds*, 2018, Vol. 764, pp. 639-649.
- [20] G. Cao, T. Sun, C. Wang, X. Li, M. Liu, Z. Zhang, P. Hu, A.M. Russell, R. Schneider, and D. Gerthsen: Investigations of γ' , γ'' and δ precipitates in heat-treated Inconel 718 alloy fabricated by selective laser melting, *Materials Characterization*, 2018, pp. 398–406.
- [21] L. Kaufman, and H. Nesor: Coupled phase diagrams and thermochemical data for transition metal binary systems — I, *Calphad*, 1978, Vol. 2, pp. 55-80.
- [22] K. Hilpert, M. Miller, and H. Gerads: Thermodynamic Study of the Liquid and Solid Alloys of the Nickel-Rich Part of the Al-Ni Phase Diagram Including the AlNi₃ Phase, *Berichte der Bunsengesellschaft für physikalische Chemie*, 1990, Vol. 94, pp. 40-47.
- [23] I. Ansara, N. Dupin, H. L. Lukas, and B. Sundman: Thermodynamic assessment of the Al-Ni system. *Journal of Alloys and Compounds*, 1997, Vol. 1, pp. 20–30. [https://doi.org/10.1016/S0925-8388\(96\)02652-7](https://doi.org/10.1016/S0925-8388(96)02652-7)
- [24] W. Huang, and Y. A. Chang: A thermodynamic analysis of the Al-Ti system, *Intermetallic*, 1998, Vol. 6, No. 6, pp. 487–498.

- [25] J. L. Murray: Phase diagrams of binary titanium alloys. Metals Park, OH, USA: ASM International, 1987, pp. 12-24.
- [26] N. Saunders: Thermodynamic parameters characterising the phase diagrams of the Al-Ti, Al-V and Ti-V binary systems. Internal Report, University of Surry, 1990.
- [27] L. Svendsen, A. Jarfors: Al-Ti-C phase diagram, Materials science and technology, 1993, Vol. 9, pp. 948-957.
- [28] U. R. Kattner, J. C. Lin, and Y. A. Chang: Thermodynamic assessment and calculation of the Al-Ti system, Metallurgical and Materials Transactions A, 1992, Vol. 23, no. 8, pp. 2081–2090, doi: 10.1007/BF02646001.
- [29] A. Zdziobek, M. Durand-Charre, and J. Driole: Experimental investigation of high temperature phase equilibria in the Nb-Al-Ti system, International Journal of Materials Research, 1995, Vol. 86, pp. 334-340.
- [30] L. Kaufman, and H. Nesor: Coupled phase diagrams and thermochemical data for transition metal binary systems - II, Calphad. 1978, Vol. 2, pp. 81-108.
- [31] J. L. Murray: Nickel-Titanium, Phase Diagrams of Binary Nickel Alloys, ASM International, 1991, pp. 342-355.
- [32] N. Dupin : Contribution l'évaluation thermodynamique des alliages polyconstitués base de nickel", PhD thesis, Institut National Polytechnique de Grenoble, 1995.
- [33] P. Bellen, K. C. H. Kumar, and P. Wollants: Thermodynamic assessment of the Ni-Ti phase diagram, International Journal of Materials Research, 1996, Vol. 87, pp. 972-978.
- [34] N. C. Ferreri, S. C. Vogel, and M. Knezevic: Determining volume fractions of γ , γ' , γ'' , δ , and MC-carbide phases in Inconel 718 as a function of its processing history using an advanced neutron diffraction procedure, Mater. Sci. Eng. A, 2020, Vol. 781, pp. 139-228. doi: 10.1016/j.msea.2020.139228.
- [35] D. Keiser, and H. Brown: Review of the physical metallurgy of Alloy 718, Idaho National Engineering Lab Idaho Falls (USA), 1976, No. ANCR-1292.
- [36] V. V. Baron, and E. M. Savitskii: Constitution diagram and properties of niobium-aluminum alloys, 1961, Vol. 6, pp. 18-22.
- [37] J. L. Jorda, R. Flukiger, and J. Muller: A new metallurgical investigation of the Niobium-Aluminium system, Journal of the Less Common Metals, 1980, Vol. 75, pp. 227– 239.
- [38] V. T. Witusiewicz, A. A. Bondar, U. Hecht, S. Rex, and T. Y. Velikanova: The Al-B-Nb-Ti system III. Thermodynamic re-evaluation of the constituent binary system Al-Ti, Alloys Compound, 2008, Vol. 1, pp. 64-77

- [39] J. C. Schuster and M. Palm: Reassessment of the binary aluminum-titanium phase diagram, *Journal of phase equilibria and diffusion*, 2006, Vol. 27, pp. 255-277.
- [40] D. M. Cupid, O. Fabrichnaya, O. Rios, F. Ebrahimi, and H. J. Seifert: Thermodynamic re-assessment of the Al-Ti-Nb system, *Metallurgical and Materials Transactions A*, 2009, Vol. 100, pp. 218-233.
- [41] A. Bolcavage, and U. R. Kattner: A reassessment of the calculated Ni-Nb phase diagram, *Phase Equilibria*, 1996, Vol. 17, no. 2, pp. 92–100, doi: 10.1007/BF02665782.
- [42] J. M. Joubert, B. Sundman, and N. Dupin: Assessment of the niobium-nickel system, *Calphad*, 2004, Vol. 28, no. 3, pp. 299–306, doi: 10.1016/j.calphad.2004.09.004.
- [43] H. Chen, and Y. Du: Refinement of the thermodynamic modelling of the Nb-Ni system, *Calphad*, 2006, Vol. 30, no. 3, pp. 308–315, doi: 10.1016/j.calphad.2006.02.005.
- [44] M. Sundararaman, P. Mukhopadhyay, and S. Banerjee: Precipitation of the δ -Ni₃Nb Phase in Two Nickel Base Superalloys, *Metallurgical Transactions A*, 1988, Vol. 19, pp. 453-465.
- [45] H. Zhang, S. Zhang, M. Cheng, and Z. Li: Deformation characteristics of δ phase in the delta-processed Inconel 718 alloy, *Materials Characterization*, 2010, pp. 49–53.
- [46] S. Azadian, L. Wei, R. Warren: Delta phase precipitation in Inconel 718, *Mater Charact*, 2004, Vol. 53, pp. 7–16.
- [47] C. He, F. Stein, and M. Palm: Thermodynamic description of the systems Co-Nb, Al-Nb and Co-Al-Nb, *J. Alloys Compd.*, 2015, Vol. 637, pp. 361–375, doi: 10.1016/j.jallcom.2015.02.182.
- [48] V. Beaubois, J. Huez, and S. Coste: Short term precipitation kinetics of delta phase in strain free Inconel 718 alloy. *Metallurgical Transactions A*, 2004, Vol. 20, pp. 1019–1026.
- [49] Y. Huang, and T. G. Langdon: The evolution of delta-phase in a superplastic Inconel 718 alloy, *Journal of Materials Science*, 2007, Vol. 42, pp. 421–427
- [50] K. Praveen, and V. Singh: Effect of cold rolling on the Coffin–Manson relationship in low-cycle fatigue of superalloy IN718, *Metallurgical and Materials Transactions A*, 2008, Vol. 39, pp. 79-86.
- [51] H. Qi, M. Azer, and A. Ritter: Studies of standard heat treatment effects on microstructure and mechanical properties of laser net shape manufactured Inconel 718, *Metall. Mater. Trans. A Phys. Metall. Mater. Sci.*, 2009, Vol. 40, no. 10, pp. 2410–2422, doi: 10.1007/s11661-009-9949-3.

- [52] J. L. Murray: The Cr-Ti (chromium-titanium) system, *Bull Alloy Phase Diagrams*, 1981, Vol. 2, pp. 174.
- [53] F. Stein, M. Palm, and G. Sauthoff: Structure and stability of Laves phases part II-structure type variations in binary and ternary systems. *Intermetallics*, 2005, Vol. 13, pp. 1056.
- [54] K. C. Chen: Compositional influences on the microstructures, phase stability, and mechanical properties of TiCr₂ Laves phase alloys, Ph.D. thesis, Massachusetts Institute of Technology, 1995.
- [55] M. K. McQuillan: A provisional constitutional diagram of the chromium-titanium system. *Journal of Materials Science*, 1951, Vol. 80, pp. 379.
- [56] J. Pavlů, J. Vřešťál, and M. Šob: Thermodynamic modelling of Laves phases in the Cr-Hf and Cr-Ti systems: Reassessment using first-principles results, *Calphad*, 2010, Vol. 34, no. 2, pp. 215–221, doi: 10.1016/j.calphad.2010.03.003.
- [57] G. Ghosh: Thermodynamic and kinetic modelling of the Cr-Ti-V system, *J. Phase Equilibria*, 2002, Vol. 23, no. 4, pp. 310–328, doi: 10.1361/105497102770331569.
- [58] V. P. Elyutin, and V. F. Funke: Some data on the phase diagram of the chromium-columbium system, *Bulletin of Alloy Phase Diagrams*, 1956, Vol. 7, pp. 68–76
- [59] M. Venkatraman, and J. P. Neumann: The Cr–Nb (Chromium-Niobium) system, *Bull. Alloy Phase Diagrams*, 1986, Vol. 7, no. 5, pp. 462–466, doi: 10.1007/BF02867811.
- [60] V. M. Pan: Definition of equilibrium diagrams for Cr–Nb and NbCr₂–Ni₃Nb systems, *Dopov. Akad. Nauk Ukr. RSR.*, 1961, pp. 332–334.
- [61] D. J. Thoma, and J. H. Perepezko: An experimental evaluation of the phase relationships and solubilities in the Nb-Cr system, *Materials Science and Engineering*, 1992, Vol. 156, pp. 97–108.
- [62] J. Pavlů, J. Vřešťál, and M. Šob: Re-modelling of Laves phases in the Cr-Nb and Cr-Ta systems using first-principles results, *Calphad*, 2009, Vol. 33, no. 1, pp. 179–186, doi: 10.1016/j.calphad.2008.04.006.
- [63] H. Lu, W. Wang, N. Zou, J. Shen, X. Lu, and Y. He: Thermodynamic modeling of Cr–Nb and Zr–Cr with extension to the ternary Zr–Nb–Cr system, *Calphad*, 2015, Vol. 50, pp. 134–143.
- [64] L. Kaufman, and H. Nesor: Coupled phase diagrams and thermochemical data for transition metal binary systems — V, *Calphad*, 1978, Vol. 2, pp. 325–348, [https://doi.org/10.1016/0364-5916\(78\)90020-2](https://doi.org/10.1016/0364-5916(78)90020-2)
- [65] J. L. Murray: Phase diagrams of binary titanium alloys. ASM International, 1987.

- [66] L. F. S. Dumitrescu, and M. Hillert: Comparison of Fe-Ti assessments, *J. Phase Equilibria*, 1998, Vol. 19, no. 5, pp. 441–448.
- [67] K. C. Harikumar, L. Dumitrescu, B. Sundman, P. Wollants: Thermodynamic assessment of the Fe–Ti system with special emphasis on the modelling of the FeTi(B2) phase, *Calphad*, 1999, Web.
- [68] E. Paul, and L. J. Swartzendruber: The Fe-Nb system, *Bull. Alloy Phase Diagrams*, 1986, Vol. 7, pp. 248-254.
- [69] D. Gruner: Investigation of the nature of Laves phases in the systems with transition Metals, Fakultät Mathematik und Naturwissenschaften, Technische Universität Dresden, 2007, pp. 1-272
- [70] M. Takeyama, N. Gomi, S. Morita, and T. Matsuo: Phase equilibria and lattice parameters of Fe₂Nb Laves phase in Fe-Ni-Nb ternary system at elevated temperatures, *Mater. Res. Soc. Symp. Proc.*, 2005, Vol. 842, pp. 461-466
- [71] S. K. Balam, and A. Paul: Interdiffusion study in the Fe-Nb system, *Metall. Mat. Trans. A*, 2010, Vol. 41A, pp. 2175- 2179
- [72] C. Servant, C. Gueneau, and I. Ansara: Experimental and thermodynamic assessment of the Fe-Zr system, *Journal of Alloys and Compounds*, 1995, Vol. 220, pp. 19-26.
- [73] S. Vob, M. Palm, F. Stein, and D. Raabe: Phase equilibria in the Fe-Nb system, *J. Phase Equilibria Diffus.*, 2011, Vol. 32, no. 2, pp. 97–104, doi: 10.1007/s11669-010-9808-3.
- [74] C. Luke Nelson: Selective laser melting of nickel superalloys for high temperature applications, Thesis for Doctor of Philosophy Degree, University of Birmingham, 2013
- [75] L. Kaufman, and H. Bernstein: *Computer Calculation of Phase Diagrams*. Academic Press, 1970, ISBN 0-12-402050-X.
- [76] C. W. Bale, E. Bélisle, P. Chartrand, S. A. Deckerov, G. Eriksson, A.E. Gheribi, K. Hack, I. H. Jung, Y. B. Kang, J. Melançon, A. D. Pelton, S. Petersen, C. Robelin. J. Sangster, P. Spencer, and M-A. Van Ende: FactSage thermochemical software and databases - 2010 - 2016, *Calphad*, Vol. 54, pp. 35-53, 2016
- [77] Z. You, and I. H. Jung: Thermodynamic optimization of the Mn–P and Fe–Mn–P systems, *Calphad*, 2021, Vol. 72, pp. 102-109.
- [78] A. T. Dinsdale: SGTE data for pure elements. *Calphad*, 1991, Vol. 15, pp. 317-425.
- [79] J. H. Hildebrand, and H. Joel: Solubility. XII. Regular Solutions, *Journal of the American Chemical Society* 1929, Vol. 51, pp. 66-80.
- [80] M. Hillert: The compound energy formalism, *Journal of Alloys and Compounds*, 2001, Vol. 320, pp. 161-176.

- [81] M. Hillert, and L.-I. Staffansson. The regular solution model for stoichiometric phases and ionic melts, *Acta Chemica Scandinavica*, 1970, Vol. 24, pp. 3618-3626.
- [82] B. Sundman, and J. Ågren: A regular solution model for phases with several components and sublattices, suitable for computer applications, *Journal of Physics and Chemistry of Solids*, 1981, Vol. 42, pp. 297–301.
- [83] H. K. Hardy: A “sub-regular” solution model and its application to some binary alloy systems, *Acta Metallurgica*, 1953, Vol. 1, pp. 202-209.
- [84] H. Lukas, B. Sundman, S. Fries, *Computational thermodynamics*, Cambridge: University Press, 2007, pp.112-251.
- [85] A.V. Grytsiv, P. Rogl, H. Schmidt, G. Giester, G. Wiesinger, P. Hundegger, and V. Pomjakushin: Formation and crystal chemistry of cubic ternary phases with filled ($\text{Th}_6\text{Mn}_{23}$)-type and (AuCu_3)-type in the systems TieM(VIII)-Al , *Intermetallics*, 2004, Vol. 12, pp. 563-577.
- [86] J. D. Verhoeven, J. H. Lee, F.C. Laabs, and L. L. Jones: The phase equilibria of Ni_3Al evaluated by directional solidification and diffusion couple experiments, *Phase Equilibria*, 1991, Vol. 12, pp. 15-23.
- [87] B. S. I. Ansara, N. Dupin, and H. L. Lukas: Thermodynamic assessment of the Al-Ni system, *J. Alloys Compd.*, 1997, Vol. 247, no. 1–2, pp. 20–30, doi: 10.1016/j.jallcom.2004.05.007.
- [88] Y. Du: Thermodynamic properties of the Al-Nb-Ni system, *Intermetallics*, 2003, Vol. 11, no. 10, pp. 995–1013, doi: 10.1016/S0966-9795(03)00123-7.
- [89] Y. Du and N. Clavaguera: Thermodynamic assessment of the Al-Ni system, *J. Alloys Compd.*, 1996, Vol. 237, no. 1–2, pp. 20–32, doi: 10.1016/0925-8388(95)02085-3.
- [90] K. Hilpert, D. Kobertz, V. Venugopal, M. Miller, H. Gerads, F. J. Bremer, and H. Nickel: Phase diagram studies on the Al- Ni system, *Zeitschrift für Naturforschung A*, 1987, Vol. 42, no. 11, pp. 1327-1332.
- [91] F. J. Bremer, M. Beyss, E. Karthaus, A. Hellwig, T. Schober, J. M. Welter, and H. Wenzl: Experimental analysis of the Al-Ti phase diagram, *Journal of crystal growth*, 1988, Vol. 87, pp. 185-192.
- [92] Z. Zhu, Y. Du, L. Zhang, H. Chen, H. Xu, and C. Tang: Experimental identification of the degenerated equilibrium and thermodynamic modelling in the Al-Nb system, *J. Alloys Compd.*, Vol. 460, no. 1–2, pp. 632–638, 2008, doi: 10.1016/j.jallcom.2007.06.033.

- [93] A. Kaufman, N. J. Hoffman, H. Lipson: Intensity anomalies in the X-ray diffraction pattern of Ni_3Nb and their relationship to those for martensite, *Scripta Metallurgica*, 1969, Vol. 3, pp. 715–719. [https://doi.org/10.1016/0036-9748\(69\)90220-8](https://doi.org/10.1016/0036-9748(69)90220-8)
- [94] V. T. Witusiewicz: The Al–B–Nb–Ti system: IV. Experimental study and thermodynamic re-evaluation of the binary Al–Nb and ternary Al–Nb–Ti systems, *J. Alloys Compound*, 2009, Vol. 472, pp. 133–161.
- [95] F. Stein, C. He, and I. Wossack: The liquidus surface of the Cr–Al–Nb system and re-investigation of the Cr–Nb and Al–Cr phase diagrams, *J. Alloys Comp*, 2014, Vol. 598, pp. 253–265.
- [96] J. L. Jorda, R. Flükiger, and J. Muller: A new metallurgical investigation of the niobium–aluminium system, *J. Less Common Met.* 1980, Vol. 75, pp. 227–239
- [97] N. Saunders, B. J. Lee: Thermodynamic evaluation of the Ti–Al–O ternary system, *International Journal of Materials Research*, 1997, Vol. 88, pp. 152-161.
- [98] A. A. A. P. D. Silva, G. C. Coelho, C. A. Nunes, J. M. Fiorani, N. David, and M. Vilasi: Nb–Al binary system: Reevaluation of the solubility limits of the (Nb), Nb_3Al , Nb_2Al and NbAl_3 phases at high temperatures, *Metall. Trans. A.*, 2019, Vol. 22, no. 5, pp. 1–8.
- [99] M. Palm, L. C. Zhang, F. Stein: Phases and phase equilibria in the Al-rich part of the Al–Ti system above 900 C, *Intermetallics*, 2002, Vol. 10, pp. 523-540.
- [100] A. Abdel-Hamid, C. H. Allibert, F. Durand: Equilibrium between TiAl , and Molten Al: Results from the Technique of Electromagnetic Phase Separation, *International Journal of Materials Research*, 1984, Vol. 75, pp. 455-458.
- [101] R. M. Waterstrat: Effect of interstitial elements on phase relationships in the titanium–aluminum system, NISTIR 88-3856, US Dept. of Commerce, 1988, pp. 1–53.
- [102] F. H. Froes, I. L. Caplan: *Titanium'92: Science and Technology*, Minerals Metals and Materials Society Warrendale PA, 1993, Vol. 3, pp. 1-12.
- [103] J. C. Schuster, M. Palm: Reassessment of the binary aluminum-titanium phase diagram, *Journal of phase equilibria and diffusion*, 2006, Vol. 27, pp. 255-277.
- [104] J. O. Andersson, T. Helander, L. Höglund, P. F. Shi, and B. Sundman: Thermo-Calc and DICTRA, Computational tools for materials science. *Calphad*, 2002, Vol. 26, pp. 273-312.
- [105] M. Cupid, M. J. Kriegel, O. Fabrichnaya, F. Ebrahimi, and H. J. Seifert: Thermodynamic assessment of the Cr–Ti and first assessment of the Al–Cr–Ti systems, *Intermetallics*, 2011, vol. 19, no. 8, pp. 1222–1235, doi: 10.1016/j.intermet.2011.03.031.

- [106] G. Ghosh: Thermodynamic and kinetic modelling of the Cr-Ti-V system, *J. Phase Equilibria*, 2002, Vol. 23, no. 4, pp. 310–328, doi: 10.1361/105497102770331569.
- [107] S. A. Minaeva, P. B. Budberg, and A. L. Gavze: Phase structure of Ti-Cr alloys, *Russian Metallurgy Metal*, 1971, Vol. 4, pp. 144-148
- [108] P. A. Farrar, and H. Margolin: A reinvestigation of the chromium-rich region of the titanium-chromium system, *Trans. AIME*, 1963, Vol. 227, pp. 1342-345.
- [109] R. J. Van Thyne, H. D. Kessler, and M. Hansen: The systems titanium-chromium and titanium-iron, *Metall. Trans. A*, 1952, Vol. 44, pp. 974-989.
- [110] V. S. Mikheyev, and T. S. Chernova: Solubility of chromium in Titanium and mechanical properties of the binary system titanium-chromium, *Titan I Ego Splavy AN SSSR Inst. Met*, 1962, Vol. 7, pp. 68-73.
- [111] M. Venkatraman, J. P. Neumann: The Cr– Nb (Chromium-Niobium) system, *Bulletin of Alloy Phase Diagrams*, 1986, Vol. 7, no.5, pp. 462-466.
- [112] J. G. Costa Neto, S. G. Fries, H. L. Lukas, S. Gama, and G. Effenberg: Thermodynamic optimisation of the Nb-Cr system, *Calphad*, 1993, Vol. 17, no. 3, pp. 219–228, doi: 10.1016/0364-5916(93)90001-R.
- [113] T. Takasugi, K. S. Kumar, C. T. Liu, and E. H. Lee: Microstructure and mechanical properties of two-phase Cr–Cr₂Nb, Cr–Cr₂Zr and Cr–Cr₂(Nb, Zr) alloys, *Materials Science and Engineering A*, 1999, Vol. 260, pp. 108-135.
- [114] J. M. Zelaya Bejarano, S. Ganma, C. A. Riheiro, and G. Effenberg: The iron-niobium phase diagram, *International Journal of Materials Research*, 1993, Vol. 84, pp. 160-164.
- [115] D. Wang, S. Yang, and M. Yang: Experimental investigation of phase equilibria in the Fe–Nb–Si ternary system, *Journal of alloys and compounds*, 2014, Vol. 605, pp. 183-192.
- [116] M. Takeyama, N. Gomi, S. Morita, and T. Matsuo: Phase equilibria and lattice parameters of Fe₂Nb Laves phase in Fe-Ni-Nb ternary system at elevated temperatures, *MRS Online Proceedings Library (OPL)*, 2005, Vol. 842, pp. 461-466.
- [117] B. Wierzba, W. J. Nowak, and D. Serafin: The Interface Reaction between Titanium and Iron-Nickel alloys, *High Temperature Materials and Processes*, 2018, Vol. 37, no. 7, pp. 683-691.
- [118] C. A. Qiu, and Z. P. Jin: An experimental study and thermodynamic evaluation of the Fe–Ti–W system at 1000°C, *Scr Metall*, 1993, Vol. 28, pp. 85–90.
- [119] M. Ko, and T. nishizawa: Effect of magnetic transition on the solubility of alloying elements in alpha iron, *Metall. Trans. A*, 1979, Vol. 43, pp. 118–126.

- [120] A. Hellawell, W. Hume-Rothery: The constitution of alloys of iron and manganese with transition elements of the first long period, *Phil Trans R Soc Lond A*, 1957, Vol. 249. pp. 417–459.
- [121] S. Fu, J. Dong, M. Zhang, and X. Xie: Thermodynamic simulation of the development of high stability 718 alloy. *Journal of Materials Engineering*, 2009, Vol. 11, pp. 8-13.
- [122] D. Dew-Hughes: The addition of Mn and Al to the hydrating compound FeTi: Range of homogeneity and lattice parameters, *Metall. Trans. A*, 1980, Vol. 11. pp. 1219–1225.
- [123] K. Santhy, and K. C. Hari Kumar: Thermodynamic reassessment of Nb-Ni-Ti system with order-disorder model, *J. Alloys Compd.*, 2015, Vol. 619, pp. 733–747.
- [124] H. L. Chen, Y. Du, H. H. Xu, Y. Liu, and J. C. Schuster: Experimental investigation of the Nb-Ni phase diagram, *Journal of materials science*, 2005, Vol. 40, pp. 6019–6022.
- [125] I. J. Duerden and W. Hume-Rothery: The equilibrium diagram of the system niobium-nickel, *Journal of the Less Common Metals*, 1966, Vol. 11, pp. 381-387.
- [126] G. Grube, O. Kubaschewski, and K. Zwiauer: Über die Gewinnung von festen Niob-Nickel-Legierungen durch Reduktion von Niobpentoxyd bei Gegenwart von Nickel, *Zeitschrift für Elektrochemie und angewandte physikalische Chemie*, 1939, Vol. 45, pp. 881-884.
- [127] B. Hassan, and J. Corney: Grain boundary precipitation in Inconel 718 and ATI 718 Plus, *Materials Science and Technology*, 2017, pp. 1879-1889.
- [128] S. Sridar, Y. Zhao, and W. Xiong: Phase transformations during homogenization of Inconel 718 alloy fabricated by suction casting and laser powder bed fusion: a CALPHAD case study evaluating different homogenization models, *Journal of Phase Equilibria and Diffusion*, 2021, Vol. 42, pp. 28-41, doi: 10.1007/s11669-021-00871-3.
- [129] W. J. Sames, K. A. Unocic, R. R. Dehoff, T. Lolla, and S. S. Babu: Thermal effects on microstructural heterogeneity of Inconel 718 materials fabricated by electron beam melting, *J. Mater. Res.*, 2014, Vol. 29, no. 17, pp. 1920–1930.
- [130] S. I. Kwon, S. H. Bae, J. H. Do, C. Y. Jo, and H. U. Hong: Characterization of the microstructures and the cryogenic mechanical properties of electron beam welded Inconel 718, *Metallurgical and Materials Transactions A*, 2016, Vol. 47, pp.777-787.
- [131] EOS Gmbh Electro Optical Systems. EOS Nickelalloy in 718 Datasheet; EOS Gmbh Electro Optical Systems: Munich, Germany, 2014.
- [132] A. Mostafa, I. Picazo Rubio, V. Brailovski, M. Jahazi, and M. Medraj: Structure, texture and phases in 3D printed IN718 alloy subjected to homogenization and HIP treatments, *Metals*, 2017, Vol. 7, pp.1-23.

- [133] Aria, Khalili: A.S.T.M. (A1014-03): Standard Specification for Precipitation-Hardening Bolting Material (UNS N07718) for High Temperature Service, 2003.
- [134] H. P. Wang, C. H. Zheng, P. F. Zou, S. J. Yang, L. Hu, and B. Wei: Density determination and simulation of Inconel 718 alloy at normal and metastable liquid states, *J. Mater. Sci. Technol.*, 2018, Vol. 34, no. 3, pp. 436–439.
- [135] V. P. Kumar and A. V. Jebaraj: Attainment of Favorable Microstructure for Residual Stress Reduction Through High-Temperature Heat Treatment on Additive Manufactured Inconel 718 Alloy, 2022. DOI: 10.21203/rs.3.rs-1151578/v1.
- [136] R. Rosten, M. Koski, E. Koppana: A guide to the calculation of theoretical densities of crystal structures for solid oxide fuel cells. 2006, pp. 38-41